Combining Ab Initio Computation with Experiments for Designing/Understanding High Energy Density Electrode Materials for Advanced Lithium Batteries

by

Ying Shirley Meng

B. Sc (Mat. Eng.) with First Class Honors
Nanyang Technological University of Singapore, 2000

Submitted to the Singapore-MIT Alliance Office
in Partial Fulfillment of the Requirements for the Degree of

DOCTOR OF PHILOSOPHY
IN ADVANCED MATERIALS FOR MICRO- & NANO- SYSTEMS
(AMM&NS)

AT
THE SINGAPORE-MIT ALLIANCE

2005

Signature of author: ______________________________
Ms. Ying Shirley Meng
AMM&NS Programme
September 30, 2004

Certified by: ______________________________
Prof. Li Yi
SMA Fellow, NUS
Thesis Advisor

Certified by: ______________________________
Prof. Gerbrand Ceder
SMA Fellow, MIT
Thesis Advisor

Accepted by: ______________________________
Prof. Choi Wee Kiong
Programme Co-Chair
AMM&NS Programme

Accepted by: ______________________________
Prof. Carl Thompson
Programme Co-Chair
AMM&NS Programme

Combining Ab Initio Computation with Experiments for Designing/Understanding High Energy Density Electrode Materials for Advanced Lithium Batteries

by

Ying Shirley Meng

Submitted to the Singapore-MIT Alliance Office in Partial Fulfillment of the Requirements for the Degree of Doctor of Philosophy in Advanced Materials for Micro- & Nano- Systems (AMM&NS)

ABSTRACT

We have performed an initial search on $LiNi_{1/3}TM1_{1/3}TM2_{1/3}O_2$ (TM1 = Co^{3+}, Al^{3+}, Fe^{3+} etc. and TM2 = Ti^{4+}, Zr^{4+}, Mn^{4+} etc.) with first principles computation. Fe substitution is found to be advantageous, since among the compounds investigated $LiNi_{1/3}Fe_{1/3}Mn_{1/3}O_2$ shows the lowest voltage at the last stage of charge. Excess Fe doping will result in non-layered phase according to mixed enthalpy calculation, thus the structural and electronic changes of $LiNi_{1/3}Fe_{1/6}Co_{1/6}Mn_{1/3}O_2$ with various lithium concentrations were investigated by first principles method. Motivated by the computation results, $LiNi_{1/3}Fe_zCo_{1/3-z}Mn_{1/3}O_2$ ($0 \leq z \leq 1/3$) cathode materials were synthesized by a sol-gel method. Excessive Fe substitution ($z > 2/9$) leads to evolution of non-layered impurity phase, which can be clearly observed by powder XRD and SEM experiments. XPS investigation for $LiNi_{1/3}Fe_zCo_{1/3-z}Mn_{1/3}O_2$ revealed that the oxidation state of Ni, Mn, Fe and Co are 2+, 4+, 3+ and 3+, respectively, which is consistent with the first principles prediction. First principles electronic structure computations indicated that Ni and Fe are simultaneously oxidized in this material and Co will only be oxidized at the very end of charge which is confirmed both by XPS and in-situ XAS. The inductive effect is found to be the main reason for Ni^{2+}/Ni^{4+} redox voltage shift in Li(Ni, TM1, TM2)O_2 layered compounds.

The second part of the thesis focuses on the three dimensional crystal structure of $LiNi_xLi_{1/3-2x/3}Mn_{2/3-x/3}O_2$ ($0 \leq x \leq 1/2$), which is an exciting new system of cathode materials for lithium ion batteries. Single crystal electron diffraction experiment indicates that Li, Ni and Mn ions are ordered in the transition metal layer and form two sublattices with significantly different occupation. It is demonstrated that for $LiNi_{1/2}Mn_{1/2}O_2$ ($x = 1/2$) such ordering would be extremely difficult to detect experimentally, if not impossible, with powder diffraction of X-ray and neutron. Detailed diffraction study reveals an *a1b2c1* stacking sequence of these ordered planes in $LiNi_{1/2}Mn_{1/2}O_2$ ($x = 1/2$) and $LiNi_{1/3}Li_{1/9}Mn_{5/9}O_2$ ($x = 1/3$), though stacking disorder is observed in $LiNi_{1/2}Mn_{1/2}O_2$. For Li_2MnO_3 ($x = 0$) the exact stacking sequence of the sample is found to depend on the synthesis conditions.

Key words: lithium battery; energy storage; ab initio; first principles; DFT; lithium nickel manganese oxides; charge ordering; stacking faults; polytypes; diffraction.

Thesis Advisors: Prof. Gerbrand Ceder
Prof. Li Yi

Acknowledgements

I would foremost like to thank my thesis advisors Prof. Gerbrand Ceder and Prof. Li Yi. Their expert guidance and constant encouragements are essential to make this thesis possible. I am truly grateful for their generosity in sharing their knowledge and insights with me.

I am lucky to have worked in both Prof. Ceder’s and Prof. Li Yi’s groups, where I had many useful and stimulating discussions. The post doctoral researchers and graduate students in Prof. Ceder’s group: Elena Arroyo, Dany Carlier, Dane Morgan, Anton Van der Ven, Eric Wu, John Reed, Chris Marianetti, Ashley Predith, Byungchan Han, Kisuk Kang, Chris Fischer, Tim Mueller Matteo Cococcioni, Thomas Maxisch and Byungwoo Kang have helped me and inspired me in many ways, making my two-year stay at MIT an enjoyable and memorable experience. I am also grateful to the post doctoral researchers and graduate students in Prof. Li Yi’s group: Tan Hao, Irene Lee, Kong Hui Zi, Wang Dong, Zhang Yong and Wang Cui Yang, it has been a pleasure to work with them.

I express special thanks to Prof. Hwang Bing Joe, a visiting professor who I met and worked with in MIT. He is a great mentor and at the same time, a great friend. It was also a pleasure to work with Wu Yin Wei, former student of Prof. Hwang, for our collaboration work.

I am grateful to Prof. Yang Shao-Horn whose generosity in sharing her knowledge and life experience at a critical stage of my research is greatly appreciated. I am especially thankful for the time she spent with me discussing about diffraction and crystal structures.

The Singapore – MIT Alliance and the Department of Materials Science and Engineering at MIT are gratefully acknowledged for financial support.

Many thanks to my parents, Meng Jizu and Yu Yiping, for their unselfish support and love through out my life. Their trust in me has made me a strong and confident person.

Most of all, I thank my husband, Richard Wee whose understanding, patience, humor and love are crucial to make this all possible.

Contents

Chapter 3 Pre-screening of Candidate Electrode Materials by First Principles Methods …………42

Chapter 4 Synthesis, Characterization & Electrochemical Testing of Fe/Co Substituted Lithium Nickel Manganese Oxides …………64

List of Figures

List of Tables

Part I

Combining Ab Initio Computation with Experiments for Designing New High Energy Density Electrode Materials: Li[$Ni_{1/3}$$TM1_{1/3}$$TM2_{1/3}$]$O_2$

CHAPTER 1

LITHIUM ION BATTERIES & THE ELECTRODE MATERIALS

Lithium ion batteries offer high energy density, flexible and light weight design and longer cycle life than other battery systems. [1] The share of worldwide sales for Li-ion portable batteries is 63%, much higher than those of Ni–Cd (23%) and Ni–MeH (14%) [2], which explains why this area receives most attention at both fundamental and applied levels. Lithium transition metal oxides are important positive electrode materials and are the focus of this thesis. In this chapter, we give a brief description of the electrochemistry in the lithium ion batteries and overview of the lithium intercalation compounds.

1.1 Lithium Ion Batteries

A battery is an energy storage and conversion device. It consists of several electrochemical cells that are connected in parallel and/or in series to provide the required capacity and voltage, respectively. Each cell has a negative (the anode in electrochemical cell) and a positive electrode (the cathode), as the sources of chemical reactions, separated by the non-aqueous electrolyte. The electrolyte contains dissociated salts, which provides an ion transport path between the two electrodes. The electrolyte takes no part in the reaction except for conveying the electroactive lithium ions during discharge from a high (chemical) energy state in the negative electrode to a low (chemical) energy state in the positive electrode while the electrons pass through the external circuit with a release of (electric) energy. If such process is reversible, in another word, the chemical energy can be re-stored by supplying electric power; the device which undertakes this process is called a rechargeable battery, see Figure 1-1. Lithium ion battery is one of the dominant rechargeable battery technologies including nickel metal hydride battery (Ni-MH) because of its higher energy density and design flexibility, as shown in Figure 1-2.

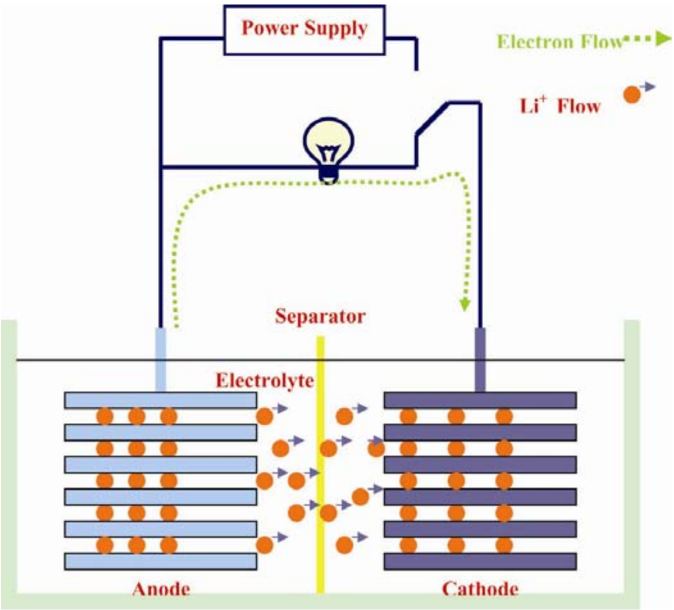

Figure 1-1 Principles of lithium ion battery - the cell is in discharge state.

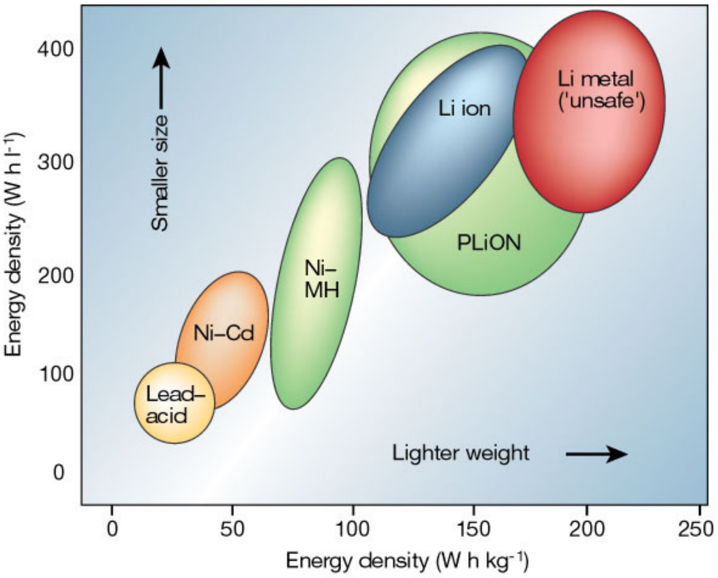

Figure 1-2 Comparison of the different battery technologies in terms of volumetric and gravimetric energy density [1].

The key parameters for electrode materials are:

i) Gravimetric specific capacity in Ah/g or energy in Wh/g

ii) Volumetric capacity in Ah/cm^3

iii) Rate capability (power density)

iv) Cycleability (stability)

v) Self-discharge (lifetime)

vi) Cost

vii) Toxicity (safety)

Considering any battery technology, measures of its performance (cell potential, capacity or energy density) are related to the intrinsic property of the materials that form the positive and negative electrodes. The cycle-life and lifetime are dependent on the nature of the electrode materials and electrode/electrolyte interfaces, whereas safety is a function of the stability of the electrode materials and interfaces.

1.2 Developments in Lithium Ion Battery Research

The first commercial lithium ion rechargeable battery was introduced by Sony Japan in 1989 [3]. Over the past three decades, Li rechargeable battery technology research has undergone three main stages in its research:

- In the 1970s, the discovery of intercalation compounds was crucial in the development of high-energy rechargeable lithium batteries [4]. In 1972, Exxon introduced a Li-metal/liquid electrolyte/TiS_2 battery [5]. However, uneven dendritic Li growth as the metal was re-plated during subsequent charge-discharge cycle caused explosion hazards. Substituting Li metal with alloys solved the dendrite problem [6], but alloy electrodes survived only a limited number of cycles due to large volume changes during the charge-discharge operation.

- In the 1980s, the discoveries of more low-dimensional intercalation compounds and the use of carbon materials as the anodic lithium insertion material led to the Li-ion battery technology or the so-called rocking chair technology. Sony commercialized the rocking-chair cell with a potential exceeding 3.6V and gravimetric energy density as high as 120-150 Wh/Kg^{-1} [3].

- The most recent development is the Li hybrid polymer electrolyte (Li-HPE) battery. ‘Hybrid” means that the electrolyte consists three components: a polymer matrix swollen with liquid solvent and a salt. Bellcore researchers developed the first reliable and practical rechargeable Li-ion HPE battery [7], named plastic Li ion (PliON), which has been commercially developed since 1999.

The demands for energy storage in the future are unpredictable with more advanced portable electronic devices and more environment-friendly transportation. The state-of-the-art lithium ion batteries use carbon materials as the anode and $LiCoO_2$ as the cathode, whose capacity will hardly be able to meet the ever-increasing demand for larger, more stable capacity. The current commercial lithium ion batteries also have serious safety problem due to instability of the overcharged Li_xCoO_2 in the electrolyte; several explosions have been reported in year 2004 alone.

1.3 Materials for the Positive Electrode

1.3.1 Intercalation Compounds

The rechargeability of the battery depends on the reversibility of the reactions on the electrodes. Intercalation compounds are considered as ideal materials since they can accommodate guest species such as lithium over large concentration ranges. The guest species can enter and leave the crystal structure of intercalation compounds without causing any significant change in the host lattice. An important category of such compounds are transition metal oxides, which consist of close-packed planes of oxygen ions with transition metal ions occupying octahedral and/or tetrahedral interstitial sites.

A typical layered structure of transitional metal oxides is shown in Figure 1-3. It consists of closed – packed oxygen planes, stacked in ABCABC sequence. The lithium and transition metal ions are octahedrally coordinated with oxygen ions and form alternate layers. A two-dimensional (sheet) channel for lithium ion transportation is available. This structure belongs to the R-3m space group and is often referred as the O3 form (α-$NaFeO_2$ iso-structure) [8]. $LiCoO_2$ adopts such crystal structure and is used as the current cathode material for commercial lithium ion battery. Other layered structures with different oxygen stacking sequences are observed, such as ABABAB in the deintercalated CoO_2 [9].

In addition, if the transition metal and lithium ions are distributed in such a way that ¾ of the transition metal ions occupy octahedral sites in alternating layers in theO3 oxygen frame while the remaining ¼ reside in the other alternating layers, such form is called the spinel crystal structure [10]. As shown in Figure 1-4, a subset of tetrahedral interstitial sites is available for lithium. Notice that this structure also has the ABCABC oxygen stacking sequence.

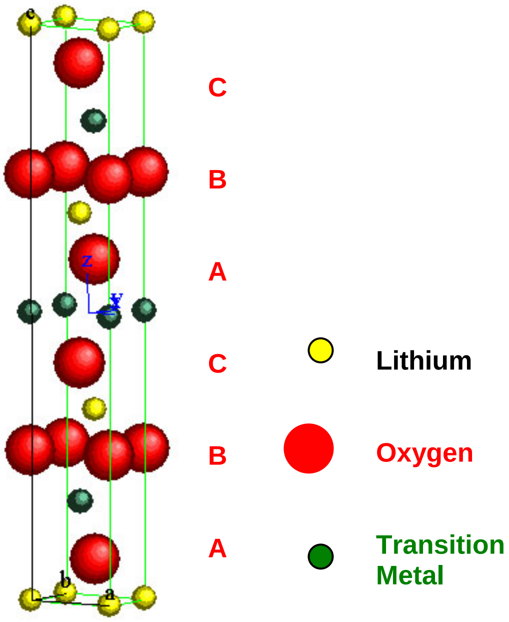

Figure 1-3 The O3 layered crystal structure, which is commonly observed in lithium transition metal oxides.

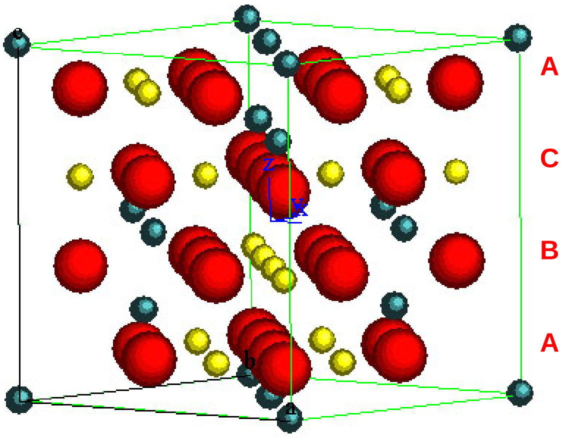

Figure 1-4 The spinel structure. Notice that a set of tetrahedral sites that are available for lithium ions.

1.3.2 $LiCoO_2$ vs. $LiNiO_2$

O3 layered $LiCoO_2$ has been studied thoroughly with experiments as well as first-principles computation [11-16]. It can be easily synthesized and enables a fast and reversible lithium intercalation over a large lithium concentration interval. In practice delithiation is limited to the value x = 0.5 for safety reason though it is feasible to reversibly cycle $LiCoO_2$ beyond 0.5Li.[17] In agreement with experiment, first principles calculations predict that O3 is stable at intermediate to high lithium concentration and that O1 is stable when the compound is fully delithiated. [18] Calculations also predict that H1-3 is stable at low lithium concentration. H1-3 is a hybrid between the O3 and O1 structures, as shown below in Figure1-5 [19].

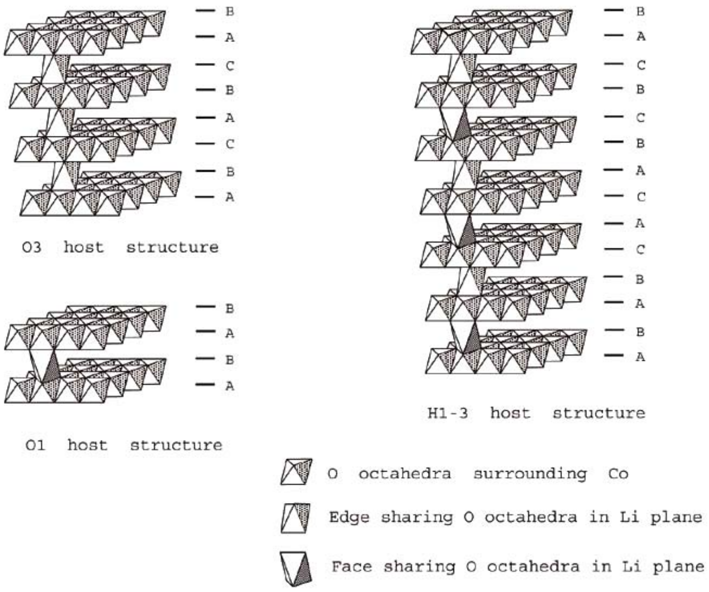

Figure 1-5 Schematic illustration of the three layered structures O3, O1 and H1-3. The vertices of each octahedral are oxygen ions.

Due to the high cost and toxicity associated with $LiCoO_2$, the use of layered $LiNiO_2$ was considered as it also has favorable specific capacity compared with $LiCoO_2$. However, expectations were dismissed for safety reasons as exothermic oxidation occurs between the organic electrolyte and the collapsing delithiated Li_xNiO_2 structure[20-23]. Both experimental and computational investigations show that a monoclinic distortion occurs upon delithiation. The coupling between the Li-vacancy ordering and the Jahn-Teller activity of Ni^{3+} ions is the origin of the monoclinic distortion [24]. In addition, high quality $LiNiO_2$ samples are very difficult to synthesize, owing to the fact that Ni^{3+} and Li^+ have similar ionic radii and are easily mixed in the layered structure.

Delithiated Li_xCoO_2 was found to be more thermally stable than its Li_xNiO_2 counterpart. Thus, substitution of Co for Ni in $LiNi_{1-x}Co_xO_2$ was adopted to provide a partial solution to the safety concerns[25, 26]. Furthermore, with electrochemically inert cationic substitute for Ni or Co with Al, Mg or Ti, practical capacities beyond 180mAh/g can be obtained [27].

1.3.3 $LiMnO_2$

Lithium manganese oxide in the O3 layered structure has been regarded as a promising positive electrode material for rechargeable lithium batteries [17] [28]. It exhibits a smoother voltage profile and has higher lithium content than other lithium manganese oxide structures such as the spinel ($LiMn_2O_4$). Unfortunately, the thermodynamically stable phase of $LiMnO_2$ does not have the α-$NaFeO_2$ structure, and all pure or lightly doped layered forms of layered-$LiMnO_2$ have been found to transform to a defective spinel-like structure upon cycling in a battery with significant change in voltage profile [29-31]. The stability of the compound has hindered its application in practice. The similar $LiCoO_2$ compound does not readily transform from layered to spinel even though such a transformation is thermodynamically favored in both Li_xMnO_2 and Li_xCoO_2.[32] Computational studies by Reed & Ceder demonstrate that these two materials differ in performance due to kinetic rather than thermodynamic factors [33].

In the first stage of layer-to-spinel transformation, a significant fraction of the Mn and Li ions rapidly occupy tetrahedral sites, forming a metastable intermediate. The second stage of layer-to-spinel transformation involves a more difficult coordinated rearrangement of Mn and Li ions to form spinel. The susceptibility of Mn migration into the Li layer is found to be controlled by its oxidation state. The Jahn-Teller active Mn^{3+} ions likely charge disproportionate to Mn^{2+} and Mn^{4+} upon delithiation and Mn^{2+} favors a tetrahedral coordination with oxygen which leads to the layer-to-spinel transformation. The mechanism of the transformation and strategies to inhibit such transformation is well explained based on the ligand field theory. [33, 34]

1.3.4 Multi-Cation Systems

Recently, layered di- and tri- transition metal oxides have become the trend in cathode materials research. Among these intercalation compounds, nickel manganese based oxide and their derivatives are considered to be one of the most promising candidates for future lithium ion batteries [35-40]. The general formula for this system is $Li[Ni_xLi_{1/3-2x/3}Mn_{2/3-x/3}]O_2$ ($0 \le x \le 1/2$), among which $LiNi_{1/2}Mn_{1/2}O_2$ has gained significant amount of attention. It is confirmed both by experiments and first-principles calculations that in the as-prepared $LiNi_{1/2}Mn_{1/2}O_2$, only Ni^{2+} and Mn^{4+} ions are present.[39, 41, 42] Therefore nickel can exchange two electrons and be oxidized to Ni^{4+} which manganese remains at a 4+ oxidation state during the charge-discharge cycle without any loss of theoretical capacity, and without the instabilities associated with more reduced states of Mn. Detailed experimental studies show that though this phase has a O3 layered structure; some (about 9%) Ni^{2+} was found in lithium sites, by XRD Rietveld refinement [35, 36]. ^{6}Li MAS NMR confirmed the presence of Li^+ in the transition metal layer [43, 44].

Theoretically, this material has a high capacity of 280 Ah/Kg assuming all Ni^{2+} are oxidized to Ni^{4+}; experimentally the material exhibits different capacity and cycling performance with different preparation methods and synthesis conditions. Y. Makimura et al. obtained a reversible capacity of 200 Ah/Kg in the potential window 2.5-4.5V and a good cycling efficiency up to 30 cycles [40]. Z.Lu et al. reported a stable capacity of 140 Ah/Kg between 3 to 4.4V and 200Ah/Kg between 2.5V to 4.8V.[36] A comparison of the electrochemical performance among $LiCoO_2$, $LiMn_2O_4$ and $LiCo_{1/2}Ni_{1/2}O_2$ with $LiNi_{1/2}Mn_{1/2}O_2$ is illustrated in Figure 1-6 [45].

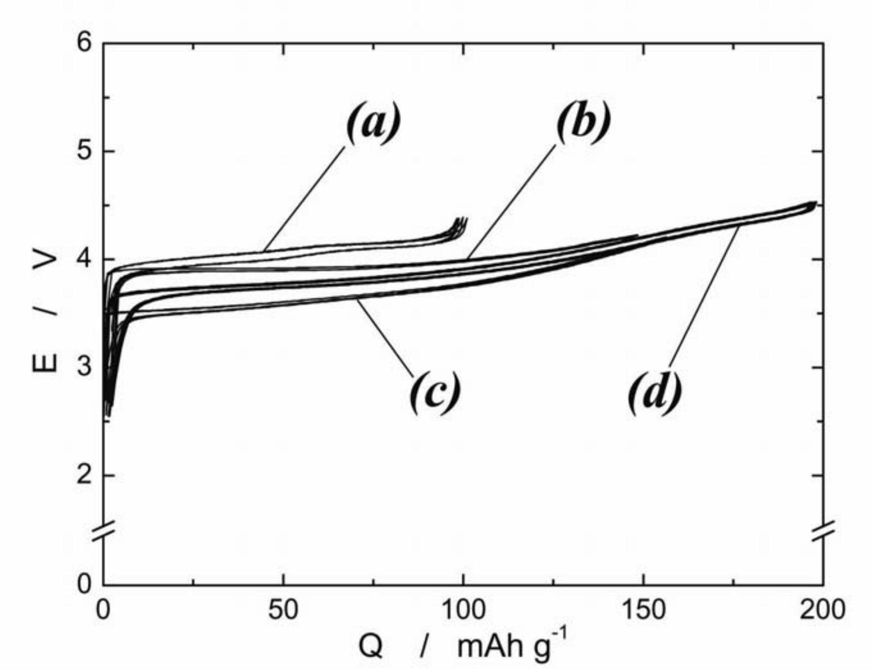

Figure 1-6 Charge and discharge curves [45] of a lithium cell with a) $Li[Li_{0.1}Mn_{1.9}]O_4$, b) $LiCoO_2$, c) $LiCo_{1/2}Ni_{1/2}O_2$ and d) $LiNi_{1/2}Mn_{1/2}O_2$ as cathode, operated in voltage range 2.5-4.5V at 0.17mA/cm^2 at room temperature.

$LiNi_{1/3}Co_{1/3}Mn_{1/3}O_2$ was also found to have very good electrochemical properties [46-49]. It is an attractive candidate for cathode material due to its ease of synthesis and excellent capacity retention. Ohzuku et al. reported that this compound has 200 mAh/g in the voltage range of 3.5-5V with negligible capacity loss up to 30 cycles [46]. Hwang et al. obtained reversible capacity of 188 mAh/g in the potential window of 3 to 4.5V [49]. Shaju et al. inferred from cyclic voltammetry results that the redox processes at 3.8V and 4.6V correspond to the Ni^{2+}/Ni^{4+} and Co^{3+}/Co^{4+} couples, respectively, though the capacity contributed by the latter redox pair is very small in this potential window [47]. First principles calculation confirmed that Co^{3+} is only oxidized to Co^{4+} at rather high voltage in this material [49, 50].

1.4 Motivation & Objectives

$LiNi_{1/2}Mn_{1/2}O_2$ and $LiNi_{1/3}Co_{1/3}Mn_{1/3}O_2$ illustrates the recent trend towards multi-component transition metal oxides, which creates a large number of possible compositional choices. The materials development including synthesis, processing, characterization and optimization, can be more efficient and cost effective if we have the ability to do accurate property predication and optimization during the materials design stage and prior to synthesis.

While first principles methods are not accurate enough to exactly predict voltages, it can act as a powerful pre-screening tool. It can predict the trend in voltages for different redox couples satisfactorily. Moreover, computational modeling can help to gain in-depth understanding of the experimental data. In this research, our goal is to show how first principles methods can be combined with various experimental tools to shorten the development cycle of a new material. The specific objectives are:

- Identify the best potential candidates cathode materials in the multi- cationic system with O3 layered structure (TM = Ni, Co, Mn, Fe, Mo, Ti, Zr, etc.) based on their lithium intercalation potentials and electronic structures.
- Synthesize and characterize the candidate materials, and optimize their electrochemical properties.
- Understand the crystal structure and electronic structure of the candidate materials at various lithium concentration

It is hoped that such direct integration of first principles methods with experimental research will aid the discovery of new electrode materials and shorten the development cycle of such materials.

References

1. J.-M. Tarascon and M. Armand, *Issues and challenges facing rechargeable lithium batteries.* Nature, 2001. **414**: p. 359.
2. H. Takeshita, *Proc. Conf. Power*. 2000. San Diego.
3. *Handbook of Battery Materials*, ed. J.O. Besenhard. 1999, Weinheim, Germany: Wiley-VCH.
4. B.C.H. Steele, *Fast Ion Transport in Solids*, ed. W. Van Gool. 1973, Amsterdam: North-Holland. p.103-109.
5. M.S. Whittingham, *Electrical Energy Storage and Intercalation Chemistry.* Science, 1976. **192**: p. 1126-1127.
6. B.M.L. Rao, Francis, R.W. and Christopher, H.A., Journal of the Electrochemical Society, 1977. **124**: p. 1490-1492.
7. J.M. Tarascon, et al., *Performance of Bellcore's plastic rechargeable Li-ion batteries.* Journal of Power Sources, 1996. **86-88**: p. 49-54.
8. C. Delmas, C. Fouassier, and P. Hagenmuller, *Structural classification and properties of the layered oxides.* Physica, 1980. **99B**: p. 81.
9. G.G. Amatucci, J.M. Tarascon, and L.C. Klein, *CoO_2, the end member of the $LixCoO_2$ solid solution.* J. Electrochem. Soc., 1996. **143**(3): p. 1114-1123.
10. W.D. Kingery, Bowen, H.K. and Uhlmann, D.R., *Introduction to Ceramics.* 1960, New York: John Wiley and Sons.
11. K. Mizushima, et al., *Li_xCoO_2 $(0<x<=1)$: a new cathode material for batteries of high energy density.* Materials Research Bulletin, 1980. **15**: p. 783-789.
12. H.J. Orman and P.J. Wiseman, *Cobalt (III) lithium oxide, $LiCoO_2$: structure refinement by powder neutron diffraction.* Acta Cryst., 1984. **C**(40): p. 12-14.
13. A. Van der Ven, et al., *First-principles investigation of phase stability in Li_xCoO_2.* Physical Review B, 1998. **58**(6): p. 2975-2987.
14. G. Ceder and A. Vanderven, *Phase diagrams of lithium transition metal oxides: investigations from first principles.* Electrochimica Acta, 1999. **45**(1-2): p. 131-150.
15. J.N. Reimers and J.R. Dahn, *Electrochemical and In Situ X-Ray Diffraction Studies of Lithium Intercalation in Li_xCoO_2.* J. Electrochem. Soc., 1992. **139**(8): p. 2091-2097.
16. T. Ohzuku and A. Ueda, *Solid-state redox reactions of $LiCoO_2$ (R-3m) for 4 volt secondary lithium cells.* J. Electrochem. Soc., 1994. **141**(11): p. 2972-2977.
17. A.R. Armstrong, et al., *The layered intercalation compounds $Li(Mn_{1-y}Co_y)O_2$: Positive electrode materials for lithium-ion batteries.* Journal of Solid State Chemistry, 1999. **145**(2): p. 549-556.
18. A.Van der Ven, M.K. Aydinol, and G. Ceder, *First-principles evidence for stage ordering in Li_xCoO_2.* J. Electrochem. Soc., 1998. **145**(6): p. 2149-2155.
19. A.Van der Ven, *First Principles Investigation of the Thermodynamic and Kinetic Properties of Lithium Transition Metal Oxides*, in *Department of Materials Science and Engineering*. 2000, Massachusetts Institute of Technology: Cambridge. p. 164.
20. J.R. Dahn, et al., *Rechargeable $LiNiO_2$/Carbon cells.* J. Electrochem. Soc., 1991. **138**(8): p. 2207-2211.

21. T. Ohzuku, A. Ueda, and M. Nagayama, *Electrochemistry and structural chemistry of $LiNiO_2(R3m)$ for 4 volt secondary lithium cells.* J. Electrochem. Soc., 1993. **140**(7): p. 1862-1870.
22. A. Rougier, P. Gravereau, and C. Delmas, *Optimization of the composition of the $Li_{1-z}Ni_{1+z}O_2$ electrode materials: structural, magnetic, and electrochemical studies.* Journal of the Electrochemical Society, 1996. **143**(4): p. 1168-1174.
23. M.E. Arroyo de Dompablo, A. Van der Ven, and G. Ceder, *First-principles calculations of lithium ordering and phase stability on Li_xNiO_2.* Physical Review B, 2002. **66**(6): p. 064112.
24. M.E. Arroyo y de Dompablo, A. Van der Ven, and G. Ceder, *On the origin of the monoclinic distortion in Li_xNiO_2.* Chemistry of Materials, 2003. **15**(1): p. 63-67.
25. C. Delmas and I. Saadoune, *Electrochemical and physical properties of the $Li_xNi_{1-y}Co_yO_2$ phases.* Solid State Ionics, 1992. **53-56**: p. 370.
26. C. Delmas, et al., *An overview of the $Li(Ni,M)O_2$ systems : syntheses, structures and properties.* Electrochimica Acta, 1999. **45**: p. 243-253.
27. G. Yuan, M.V. Yakovleva, and W. Ebner, *Novel $LiNi_{1-x}Ti_{x/2}Mg_{x/2}O_2$ compounds as cathode materials for safer lithium ion batteries.* Electrochemical and Solid State Letters, 1998. **1**(117-119).
28. B. Ammundsen, et al., *Formation and structural properties of layered $LiMnO_2$ cathode materials.* Journal of the Electrochemical Society, 2000. **147**(11): p. 4078-4082.
29. G. Vitins and K. West, *Lithium Intercalation into Layered $LiMnO_2$.* Journal of the Electrochemical Society, 1997. **144**(8): p. 2587-2592.
30. A. Blyr, et al., *Self-discharge of $LiMn_2O_4/C$ Li-ion cells in their discharged state - Understanding by means of three-electrode measurements.* Journal of the Electrochemical Society, 1998. **145**(1): p. 194-209.
31. Y. Shao-Horn, et al., *Structural characterization of layered $LiMnO_2$ electrodes by electron diffraction and lattice imaging.* Journal of the Electrochemical Society, 1999. **146**(7): p. 2404-2412.
32. A. Van der Ven and G. Ceder, *Electrochemical properties of spinel Li_xCoO_2: A first-principles investigation.* Physical Review B - Condensed Matter, 1999. **59**(2): p. 742-749.
33. J. Reed, G. Ceder, and A. Van Der Ven, *Layered-to-spinel phase transition in Li_xMnO_2.* Electrochemical and Solid-State Letters, 2001. **4**(6): p. A78.
34. J. Reed, *Ab Initio Study of Cathode Materials for Lithium Batteries*, in *Department of Materials Science and Engineering*. 2003, Massachusetts Institute of Technology: Cambridge, MA. p. 311.
35. Z.H. Lu, et al., *Synthesis, structure, and electrochemical behavior of $Li\ Ni_xLi_{1/3-2x/3}Mn_{2/3-x/3}O_2$.* Journal of the Electrochemical Society, 2002. **149**(6): p. A778-A791.
36. Z.H. Lu and J.R. Dahn, *Understanding the anomalous capacity of $Li/Li\ Ni_xLi_{(1/3-2x/3)}Mn_{(2/3-x/3)}O_2$ cells using in situ X-ray diffraction and electrochemical studies.* Journal of the Electrochemical Society, 2002. **149**(7): p. A815-A822.
37. Z.H. Lu, Z.H. Chen, and J.R. Dahn, *Lack of cation clustering in $Li\ Ni_xLi_{1/3-2x/3}Mn_{2/3-x/3}O_2$ $(0 < x <= 1/2)$ and $LiCr_xLi_{(1-x)/3}Mn_{(2-2x)/3}O_2$ $(0 < x < 1)$.* Chemistry of Materials, 2003. **15**(16): p. 3214-3220.

38. Y. Makimura, and T. Ohzuku, *Lithium insertion material of* $LiNi_{1/2}Mn_{1/2}O_2$ *for advanced lithium-ion batteries.* Journal of Power Sources, 2003. **119**: p. 156-160.
39. J. Reed and G. Ceder, *Charge, potential, and phase stability of layered* $Li(Ni_{0.5}Mn_{0.5})O_2$. Electrochemical and Solid State Letters, 2002. **5**(7): p. A145-A148.
40. T. Ohzuku and Y. Makimura, *Layered lithium insertion material of* $LiNi_{1/2}Mn_{1/2}O_2$*: A possible alternative to* $LiCoO_2$ *for advanced lithium-ion batteries.* Chemistry Letters, 2001(8): p. 744-745.
41. H. Kobayashi, et al., *Structural determination of* $Li_{1-y}Ni_{0.5}Mn_{0.5}O_2$ *(y=0.5) using a combination of Rietveld analysis and the maximum entropy method.* Journal of Materials Chemistry, 2004. **14**(1): p. 40-42.
42. W.S. Yoon, et al., *In situ X-ray absorption spectroscopic study on* $LiNi_{0.5}Mn_{0.5}O_2$ *cathode material during electrochemical cycling.* Chemistry of Materials, 2003. **15**(16): p. 3161-3169.
43. C.P. Grey, and Y.J. Lee, *Lithium MAS NMR studies of cathode materials for lithium-ion batteries.* Solid State Sciences, 2003. **5**(6): p. 883-894.
44. W.S. Yoon, et al., *Local structure and cation ordering in O3 lithium nickel manganese oxides with stoichiometry* $LiNi_xMn_{(2-x)/3}Li_{(1-2x)/3}O_2$ *- NMR studies and first principles calculations.* Electrochemical and Solid State Letters, 2004. **7**(7): p. A167-A171.
45. Y. Makimura, N. Nakayama, and T. Ohzuku. *Structural Chemistry and Electrochemistry of* $LiNi_{1/2}Mn_{1/2}O_2$ *for Advanced Lithium Batteries*. in *The Electrochemical Society Meeting*. 2003. Paris France.
46. T. Ohzuku and Y. Makimura, *Layered lithium insertion material of* $LiCo_{1/3}Ni_{1/3}Mn_{1/3}O_2$ *for lithium-ion batteries.* Chemistry Letters, 2001(7): p. 642-643.
47. K.M. Shaju, G.V.S. Rao, and B.V.R. Chowdari, *Performance of layered* $Li(Ni_{1/3}Co_{1/3}Mn_{1/3})O_2$ *as cathode for Li-ion batteries.* Electrochimica Acta, 2002. **48**(2): p. 145-151.
48. I. Belharouak, et al., $Li(Ni_{1/3}Co_{1/3}Mn_{1/3})O_2$ *as a suitable cathode for high power applications.* Journal of Power Sources, 2003. **123**(2): p. 247-252.
49. B.J. Hwang, et al., *A combined computational/experimental study on* $LiNi_{1/3}Co_{1/3}Mn_{1/3}O_2$. Chemistry of Materials, 2003. **15**(19): p. 3676-3682.
50. Koyama, Y., et al., *Crystal and electronic structures of superstructural* $Li_{1-x}Co_{1/3}Ni_{1/3}Mn_{1/3}O_2$ $(0 \leq x \leq 1)$. Journal of Power Sources, 2003. **119**: p. 644-648.

CHAPTER 2

FIRST PRINCIPLES COMPUTATION

First principles methods are distinguished from empirical methods since they require only nuclear charges and number of electrons as inputs, without any adjustable experimental parameters. Through the application of quantum mechanics, the structure and properties of a substance can be calculated. Over the past few years, first principles methods have been proven as excellent complementary tools to laboratory experiments in the research of cathode materials for lithium ion battery [1-3]. In some case, the first principles methods even led the experiments to the discovery of new phases in these systems [4]. We believe that direct integration of the first principles computation with various experiments will significantly shorten the development cycle of new electrode material. In this chapter, we will discuss briefly the method applied in this work and what approximations are assumed in calculations of the physical quantities.

2.1 Quantum Mechanics and First Principles Energies

First principles methods can control and manipulate a modeled system at atomic scale; therefore characteristics of such a system can be more precisely calculated provided that this modeled system reflects the real system. Lithium transition metal oxides are complex solids, for such many bodied systems, a number of approximations must be made in order to obtain a solution for the many-body wave function ψ.

The first approximation is the Born-Oppenheimer approximation where the electrons are assumed to move so much faster than the nuclei that the nuclei can be treated as stationary. This approximation allows a separate wave function ψ that contains information about electrons only to be determined, thus the Schrödinger equation can be expressed as

$$H\psi = E\psi \qquad \text{Eq. 2 -1}$$

Where H is the Hamiltonian operator for the solid, E is the total energy of the solid and ψ is the wave function describing N electrons. The electronic wave functions that satisfy the Schrödinger equation must be anti-symmetric to obey the Pauli Exclusion Principle. The coordinates of nuclei act only as parameters in the Schrödinger equation, and the interaction between the electrons and the nuclei of the solid is represented as the Ewald energy arising from the columbic interactions. The Hamiltonian operator can be written in atomic units as

$$H = T + V_{ee} + \sum_j v(\vec{r}_j) + \sum_n \sum_{m<n} \frac{Z_m Z_n}{\left|\vec{R}_m - \vec{R}_n\right|} \qquad \text{Eq. 2 -2}$$

T describes the electronic kinetic energy, V_{ee} is the coulomb interactions between the different electrons and $v(\vec{r})$ is the coulomb potential due to the nuclei of the solid.

For many bodied system, solving the above many body Schrödinger equation is intractable. Variational approximation says that for any square integrable function φ, an upper bound for the ground state energy E_0 of the system governed by the Hamiltonian H is provided by [5]

$$E[\varphi] = \frac{\langle \varphi | H | \varphi \rangle}{\langle \varphi | \varphi \rangle} \geq E_0 \qquad \text{Eq. 2 -3}$$

φ is solved for $\partial E(\varphi) = 0$ but a trial function has to be determined to start with the variational minimization of energy.

One type of trial function is a Slater determinant of single electron orbitals, such a method is called the Hartree-Fock method [6]. However in this thesis, we focus on the first principles method based on the Density Functional Theory.

2.2 Density Functional Theory

DFT has some advantages over the Hartree-Fock method in terms of accuracy and simplicity. As proven by Hohenberg and Kohn [7], the ground-state properties of a crystal are uniquely determined by the electron density $\rho(\overrightarrow{r})$

$$\rho(\overrightarrow{r}) = \langle \psi | \sum_j \delta(\vec{r} - \vec{r}_j) | \psi \rangle \qquad \text{Eq. 2 -4}$$

The fundamental theorems of DFT state that the ground state energy $E[\rho(\vec{r})]$ of a solid is a function of the electron density [7]

$$E[\rho(\vec{r})] = F[\rho(\vec{r})] + \int \rho(\vec{r}) v(\vec{r}) d\vec{r} \qquad \text{Eq. 2 -5}$$

where $F[\rho(\vec{r})] = \langle \psi | T + V_{ee} | \psi \rangle$ is a universal function. ψ is the electronic wave function that minimizes $\langle \psi | T + V_{ee} | \psi \rangle$ with the constraint that ψ produces the electron density $\rho(\overrightarrow{r})$. $F[\rho(\vec{r})]$ is independent of the nuclear arrangement and charge, according to DFT if it is known then the ground state energy can be uniquely determined. [6, 7]

Kohn and Sham introduced a separation of $F[\rho(\vec{r})]$ by writing it as [8]

$$F[\rho] = T[\rho] + J[\rho] + E_{xc}[\rho] \qquad \text{Eq. 2 -6}$$

where $T[\rho]$ is the kinetic energy of a system of non-interacting electrons. $J[\rho]$ is the classical Coulomb energy, often referred as the Hartree term, and $E_{xc}[\rho]$ is called the exchange-correlation energy. $E_{xc}[\rho]$ includes the difference between the kinetic energy of a system of independent electrons and the kinetic energy of the actual interacting system with the same density.

2.3 LDA and GGA

The most common (and simplest) approximation to E_{xc} is the local density approximation (LDA) proposed by Kohn and Sham [8]. In LDA, the exchange correlation energy per electron at $\vec{r}$ is set equal to the exchange correlation energy per electron of a homogeneous electron gas with the same density. Therefore, the local density approximation is a good approximation for system with a slowly varying electron density. For solids in which the electronic states are highly localized in space, we can expect LDA to break down since it cannot capture the strong correlations between the localized electrons.

The generalized gradient approximation (GGA) is developed by Purdue and Yue [6] in order to address the major source of error in LDA. GGA attempts to capture some of the deviation of the exchange-correlation energy from the uniform electron gas result [9]. It has been well-accepted that GGA is more suitable in systems where the electronic states are highly localized in space, such as the lithium transition metal oxides.

Many numerical techniques exist for solving the Kohn-Sham equations. For oxides, one of the most reliable methods is called the pseudopotential method [10-12], which is applied in this work. In the pseudopotential method, the effects of the core electrons around the ions that do not participate in bonding are replaced by pseudopotential. The pseudopotential approximation is valid as long as the core electrons do not participate in the bonding of the solid. Their wave functions and energy levels are negligible when the atom is placed in different environments. For most of the solids, this approximation is valid.

2.4 VASP

The first principles method used in this work is called “Vienna Ab Initio Software Package” or VASP [13, 14]. VASP solves the Kohn-Sham equations iteratively for valence orbitals using ultra-soft pseudopotentials determined from first principles. The exchange-correlation energy functional is spin-polarized GGA. This is due to the fact that for lithium manganese oxides spin polarized GGA correctly calculated ground states that were not obtained by the LDA method [15].

References:

1. G. Ceder, et al., *Identification of cathode materials for lithium batteries guided by first-principles calculations.* Nature, 1998. **392**: p. 694-666.
2. G. Ceder, *Predicting properties from scratch.* Science, 1998. **280**: p. 1099-1104.
3. G. Ceder, et al., *Computational modeling and simulation for rechargeable batteries.* Mrs Bulletin, 2002. **27**(8): p. 619-623.
4. G. Ceder and A. Van der ven, *Phase diagrams of lithium transition metal oxides: investigations from first principles.* Electrochimica Acta, 1999. **45**(1-2): p. 131-150.
5. B.H. Bransden and C.J. Joachin, *Introduction to Quantum Mechanics*. 1989: Longman Group UK Limited.
6. R.G. Parr and W. Yang, *Density-Functional Theory of Atoms and Molecules*. 1989, Oxford England: Clarendon Press.
7. P. Hohenberg and W. Kohn, *Inhomogeneous electron gas.* Physical Review, 1964. **136**(3B): p. 864.
8. W. Kohn and L.J. Sham, *Self-consistent equation including exchange and correlation effects.* Physical Review, 1965. **140**(4A): p. 1133.
9. K. Ohno, K. Esfarjani, and Y. Kawazoe, *Computational Materials Science: from ab initio to Monte Carlo Methods*. 1999, Berlin: Springer.
10. A.F. Kohan and G. Ceder, *Calculation of total energies in multicomponent oxides.* Computational Materials Science, 1997. **8**(1-2): p. 142-152.
11. M.C. Payne, et al., *Iterative Minimization Techniques for Abinitio Total-Energy Calculations - Molecular-Dynamics and Conjugate Gradients.* Reviews of Modern Physics, 1992. **64**(4): p. 1045-1097.
12. A.F. Kohan, *Total-Energy Models for Phase-Stability Studies in Multicomponent Oxides*, in *Department of Materials Science and Engineering*. 1997, Massachusetts Institute of Technology: Cambridge.
13. G. Kresse and J. Furthmuller, Comp. Mat. Sci., 1996. **6**: p. 15.
14. G. Kresse and J. Furthmuller, Physical Review B, 1996. **54**: p. 11169.
15. S.K. Mishra and G. Ceder, *Structural stability of lithium manganese oxides.* Physical Review B - Condensed Matter, 1999. **59**(9): p. 6120-6130.

CHAPTER 3

PRESCREENING OF CANDIDATE ELECTRODE MATERIALS BY FIRST PRINCIPLES METHODS

An initial search on $LiNi_{1/3}TM1_{1/3}TM2_{1/3}O_2$ where TM1 is a 3+ transition metal (Co^{3+}, Al^{3+}, Fe^{3+} etc) and TM2 is a 4+ transition metal (Ti^{4+}, Zr^{4+}, Mn^{4+} etc.) was carried out. It has been amply demonstrated that reasonable lithium intercalation potentials and geometrical information can be obtained with first principles methods [1, 2]. The relative stability of phase can also be predicted with total energy calculation. In this chapter, we will discuss the computational details of the work, demonstrating how the first principles method can act as a prescreening tool to identify potential cathode materials.

3.1 Computation Details

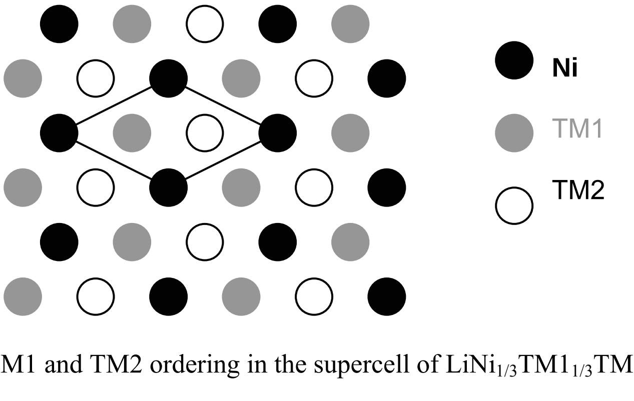

Figure 3-1 Ni, TM1 and TM2 ordering in the supercell of $LiNi_{1/3}TM1_{1/3}TM2_{1/3}O_2$

To describe the $Li_xNi_{1/3}TM1_{1/3}TM2_{1/3}O_2$ system, supercells with three formula units were used. As most of the computation methods do, this computation approach requires the use of periodic boundaries; Ni, TM1 and TM2 are long-range ordered on a triangular lattice of transition metal sites as shown in Figure 3-1. Partial states of de-lithiation were investigated at $x = 2/3$ and $1/3$. The number of possible arrangements for Li and vacancy sites in the supercell were 1, 3, 3 and 1 for $x=1$, $2/3$, $1/3$ and 0, respectively. All possible arrangements have been calculated.

All energies, intercalation potentials, geometries and electronic structure of materials in this work were obtained using first-principles quantum mechanics in the Generalized Gradient Approximation (GGA) to Density Functional Theory (DFT), as implemented in the Vienna Ab Initio Simulation Package (VASP). Ultra-soft pseudo-potentials are applied to represent the nuclei and core electrons and all structures are fully relaxed with respect to internal and external cell parameters. The wave functions are expanded in plane waves with energy below 405eV. Brillouin zone integration of the band structure is performed with a $6\times3\times4$ mesh. All calculations are performed with spin polarization, previously demonstrated to be crucial in manganese oxides [3]. Both ferromagnetic and anti-ferromagnetic spin polarization was taken into consideration, no qualitative difference was found in the voltage and relative formation energies calculation. Since experimentally, the materials are mostly found paramagnetic, we will not discuss the effect of magnetic configuration here.

3.2 Formation Energies

According to general alloy theory [4], a measure of the effective Ni-TM1-TM2 interactions can be obtained by comparing the energy of $LiNi_{1/3}TM1_{1/3}TM2_{1/3}O_2$ to the average energy of $LiNiO_2$, $LiTM1O_2$ and $LiTM2O_2$.

$$\Delta E_{mix}^{x=1} = E_{LiNi_{1/3}TM1_{1/3}TM2_{1/3}O_2} - \frac{1}{3}(E_{LiNiO_2} + E_{LiTM1O_2} + E_{LiTM2O_2}) \qquad \text{Eq. 3-1}$$

If ΔE_{mix} is negative, Ni, TM1 and TM2 have an attractive interaction on average and the system will be either randomly mixed or ordered, depending on the synthesis temperature. If ΔE_{mix} is positive, it is energetically more favorable to phase separate into Ni, TM1 and TM2 rich regions, though random mixing can be achieved if the synthesis temperature is high enough. By calculating the relevant energies values in the above formula, it was found that all ΔE_{mix} (meV per Li) for the compounds: $LiNi_{1/3}TM1_{1/3}Mn_{1/3}O_2$ (TM1 = Co, Al, Fe) and $LiNi_{1/3}Co_{1/3}TM2_{1/3}O_2$ (TM2 = Mn, Ti, Zr) are negative. It implies that the synthesis of these materials is thermodynamically favorable.

For fully delithiated $Li_xNi_{1/3}TM1_{1/3}TM2_{1/3}O_2$, ΔE_{mix} computed by

$$\Delta E_{mix}^{x=0} = E_{Ni_{1/3}TM1_{1/3}TM2_{1/3}O_2} - \frac{1}{3}(E_{NiO_2} + E_{TM1O_2} + E_{TM2O_2}) \qquad \text{Eq. 3 – 2}$$

is usually positive. For example, ΔE_{mix} of $Li_xNi_{1/3}Fe_{1/3}Mn_{1/3}O_2$ (x = 0), is calculated to be +34meV per formula unit. To remove the last one-third of lithium, one not only has to supply the binding energy of the lithium ion and electron, but also the strong energy raise in the system due to the unfavorable $Ni^{VI} - Fe^{VI} - Mn^{VI}$ interaction.

The relative formation energy E_{RF} for a given lithium-vacancy arrangement with lithium concentration in $Li_xNi_{1/3}TM1_{1/3}TM2_{1/3}O_2$, is defined as

$$\Delta E_{RF} = E_{Li_xNi_{1/3}Fe_{1/3}Mn_{1/3}O_2} - xE_{LiN_{1/3}Fe_{1/3}Mn_{1/3}O_2} - (1-x)E_{Ni_{1/3}Fe_{1/3}Mn_{1/3}O_2} \qquad \text{Eq. 3 – 3}$$

Relative formation energy more conveniently displays relative stability between different phases. The relative formation energies for $Li_xNi_{1/3}Fe_{1/3}Mn_{1/3}O_2$ are negative, as shown in Figure 3-2. It can be seen that at x = 1/2, the Li-vacancy arrangement lies on the convex hull, which indicates $Li_{1/2}Ni_{1/3}Fe_{1/3}Mn_{1/3}O_2$ will not phase separate into a two-phase mixture of $LiNi_{1/3}Fe_{1/3}Mn_{1/3}O_2$ and $Ni_{1/3}Fe_{1/3}Mn_{1/3}O_2$.

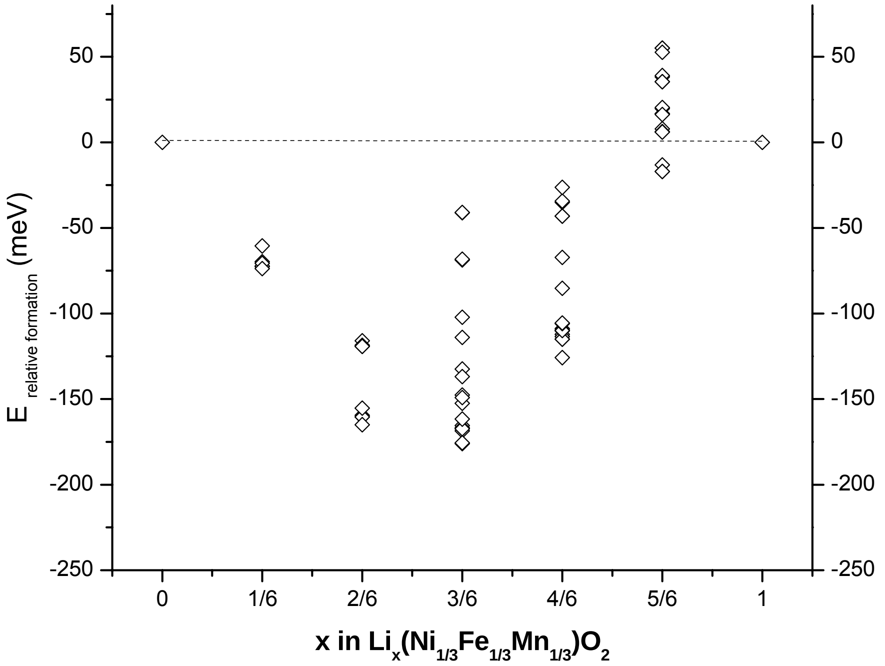

Figure 3-2 Relative formation energy (E_{RF}) of $Li_xNi_{1/3}Fe_{1/3}Mn_{1/3}O_2$ calculated with antiferromagnetic coupling in a supercell of six formula units.

3.3 Voltages

Measuring the cell voltage at equilibrium versus charge passed between the electrodes is equivalent to measuring the chemical potential as a function of x in the lithium intercalation compound. This simple fact derived from the Nernst equation [5] can be written as

$$V(x) = -\frac{(\mu_{Li}^{cathode} - \mu_{Li}^{anode})}{ze} \qquad \text{Eq. 3 – 4}$$

where μ_{Li}^{anode} is constant if metallic lithium is used as anode;

According to the thermodynamics of intercalation compounds, the Gibbs free energy G changes with the concentration x of intercalated Li. The chemical potential is simply the slope of G_f with respect to x,

$$\mu_{Li}^{cathode} = (\frac{\partial G_f}{\partial x})_{T,P,N_{host}} \qquad \text{Eq. 3 – 5}$$

In this work, G_f is approximated by E (total energy) because electronic, vibrational and configurationally excitations are not considered.

Figure 3-3 shows the potential of some of the possible compounds as average voltages over intervals of 1/3 Li composition. The stepwise nature of the curves is therefore artificial and due to the averaging of the potential over the specific composition interval. The effect of disorder, present in a real system, would likely smooth the voltage curve from what is achieved computationally.

Previously in section 1.3.4, we have mentioned that a multi-cation compound $LiNi_{1/3}Co_{1/3}Mn_{1/3}O_2$ is a promising cathode material. Nevertheless first principles calculation and experimental studies [6, 7] reveal that Co^{3+} is only oxidized to Co^{4+} at rather high voltage (about 5V), where normal electrolyte tends to break down. in this material. If we can find an intercalation compound, by substituting Mn^{4+} with other 4+ transition metal ions; or by replacing Co^{3+}/Co^{4+} redox couple by another redox couple which will be active in the operation voltage window 3.0-4.5V, we can achieve higher specific capacity (mAh/g) in the fixed voltage range.

As it can be clearly seen in Figure 3-3, if the calculated voltage of $LiNi_{1/3}Co_{1/3}Mn_{1/3}O_2$ is regarded as the reference point, substitution of Mn by either Ti or Zr clearly increases the average potential. It needs to be point out that the GGA calculations tend to under-predict the voltages in layered transition metal oxides, which as been amply demonstrated [8]. The potential difference between the calculated and experimental voltages is suggested to be about 0.7-0.8V.[9] The self-interaction in GGA tends to delocalize electrons too much, and as such the first principles methods are unable to capture precisely the Coulomb correlation effects in correlated electron systems like transition metal oxides. The problem has recently been highlighted and fixed by Zhou et al. [10, 11] with the implantation of GGA+U method.

In agreement with previous work on Al-doping [2], substitution of Co by Al increases the potential. As it can not be easily oxidized beyond 3+, Al doping is expected to reduce the capacity at the end of charge. Of all the compositional modifications investigated, Fe substitution of Co seems to be advantageous since it lowers the voltage profile at the last stage of the charge, compared to $LiNi_{1/3}Co_{1/3}Mn_{1/3}O_2$, whose capacity in the voltage range 3.0 – 4.5V is limited by higher voltage of Co^{3+}/Co^{4+} redox couple. Hence, the specific capacity of $LiNi_{1/3}Fe_{1/3}Mn_{1/3}O_2$ could be higher in the potential window of 3.0-4.5V.

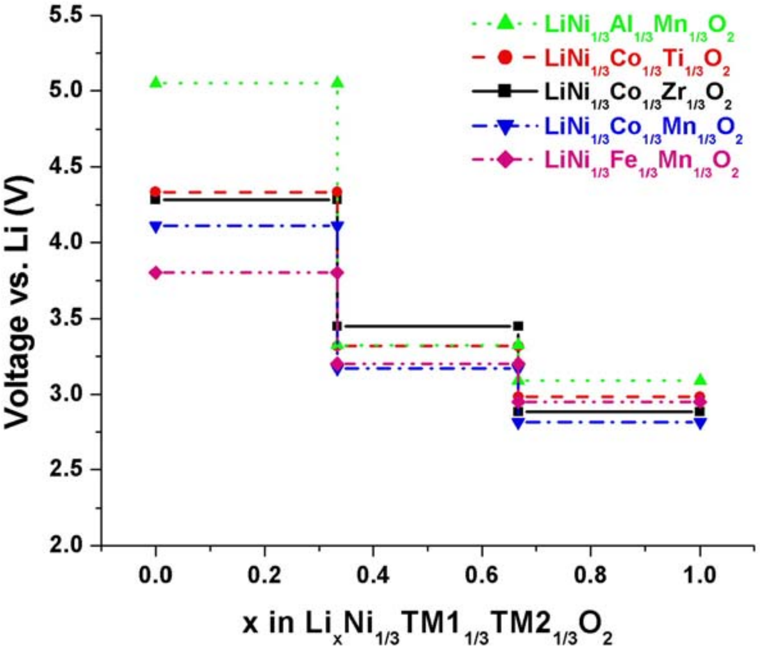

Figure 3-3 Calculated voltage curves for $LiNi_{1/3}TM1_{1/3}TM2_{1/3}O_2$ where TM1 = Al^{3+}, Co^{3+} or Fe^{3+} and TM2 = Mn^{4+}, Ti^{4+} or Zr^{4+}

Here we have demonstrated that with the first principles compotation as a prescreening tool, we identified the Fe substituted nickel manganese oxide could deliver higher specific capacity in the practical voltage range compared with other compounds in $LiNi_{1/3}TM1_{1/3}Mn_{1/3}$ system, therefore could be a potential candidate for cathode material in lithium ion battery. The detailed analysis of the effect of cation substitution on Li intercalation voltages will be presented in chapter 5.

3.4 Material of the Choice

Concerning iron substitution, numerous works have been carried out in lithium nickel-iron oxides [12-14]. In those work the presence of iron ions does not suppress the disordering in the structure and degrades the cell capacity compared to $LiNiO_2$. According to a review by Delmas [15], the small difference in size between lithium ions and the substituting atom leads to its preferential occupancy on the lithium site in a layered structure. The size of Fe^{3+} (0.65 Å) ion is comparable to those of Ni^{2+}(0.69 Å) and Li^{+}(0.70 Å), though in all previous works, Ni ions shall be in the oxidation state of Ni^{3+} for perfect stoichiometric compound, though small amount of Ni^{2+} is always found in the pristine material. It is well known that due to the similar ion size of Fe^{3+} and Li^{+}, the Fe can partially occupy the Li-layer [12-14]. In addition, unlike $LiCoO_2$ and $LiNiO_2$, the $LiFeO_2$ ground-state structure is not layered, but a structure with symmetry $I4_1/amd$ [15]. According to our preliminary mixing enthalpy calculations using the equation below, the relative formation energy of $LiNi_{1/3}Fe_{1/3}Mn_{1/3}O_2$ with respect to $LiNi_{1/2}Mn_{1/2}O_2$ and $LiFeO_2$ is approximately zero, indicating that only a weak entropic driving force for mixing might exist in a compound where Co is fully substituted by Fe.

$$\Delta E_{mix} = E_{LiNi_{1/3}Fe_zCo_{1/3-z}Mn_{1/3}O_2} - [\tfrac{2}{3} E_{LiNi_{1/2}Mn_{1/2}O_2} + zE_{LiFeO_2} + (\tfrac{1}{3} - z)E_{LiCoO_2}] \qquad \text{Eq. 3 - 6}$$

Therefore, in first principles computation we chose to substitute Co only partially by Fe and targeted the nominal composition $LiNi_{1/3}Fe_{1/6}Co_{1/6}Mn_{1/3}O_2$ in order to have reasonable supercell size.

To describe the $Li_xNi_{1/3}Fe_{1/6}Co_{1/6}Mn_{1/3}O_2$ system, supercells with six formula units were used. As it is typical in solid state computations periodic boundaries are used, so that one effectively models a system with Ni, Fe Co and Mn long-range ordered (Figure 4). Partial states of delithiation were investigated at x = 5/6, 2/3, 1/2, 1/3 and 1/6. The number of possible arrangements for Li and vacancy sites in the supercell were 1, 6, 15, 20, 15, 6 and 1 for x = 1, 5/6, 2/3, 1/2, 1/3, 1/6 and 0, respectively. All possible arrangements have been calculated.

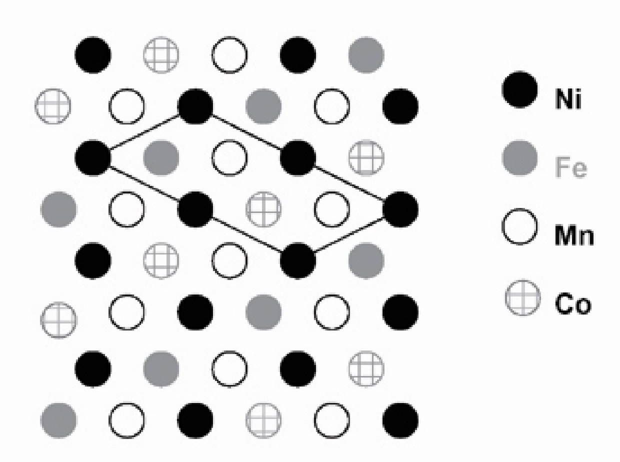

Figure 3-4. Ni, Fe, Co Mn ordering in the supercell of$Li(Ni_{1/3}Fe_{1/6}Co_{1/6}Mn_{1/3})O_2$.

3.4.1 Intercalation Voltage

Average voltage profiles for $Li_xNi_{1/3}Fe_{1/6}Co_{1/6}Mn_{1/3}O_2$ ($0 \le x \le 1$) were computed from the lowest energy lithium-vacancy arrangements in the six-formula supercell as function of lithium compositions. The calculated potentials are typically lower than experimental values, as is usually the case in standard first principles energy methods [8, 9]. The calculated intercalation voltage of $Li_xNi_{1/3}Fe_{1/6}Co_{1/6}Mn_{1/3}O_2$ is compared to that of $Li_xNi_{1/3}Co_{1/3}Mn_{1/3}O_2$ in Figure 3-5. In the range $1/3 \le x \le 1$, a calculated average voltage of 3.0-3.1V is obtained for $Li_xNi_{1/3}Fe_{1/6}Co_{1/6}Mn_{1/3}O_2$. The potential increases significantly to 3.8-3.9V in the range $0 \le x \le 1/3$. Compared to $Li_xNi_{1/3}Co_{1/3}Mn_{1/3}O_2$ [7], (shown by the solid line in Figure 3-5) the substitution of Fe with Co increases the average voltage slightly for $1/2 \le x \le 1$. Most importantly, in the Fe substituted compound, the calculated voltage at the end of charge ($0 \le x \le 1/3$) is much lower than that of $Li_xNi_{1/3}Co_{1/3}Mn_{1/3}O_2$. These results indicate that Fe substitution of Co in $LiNi_{1/3}Fe_zCo_{1/3-z}Mn_{1/3}O_2$ may flatten the voltage curve and increase the experimentally attainable capacity by lowering the potential near the end of charge.

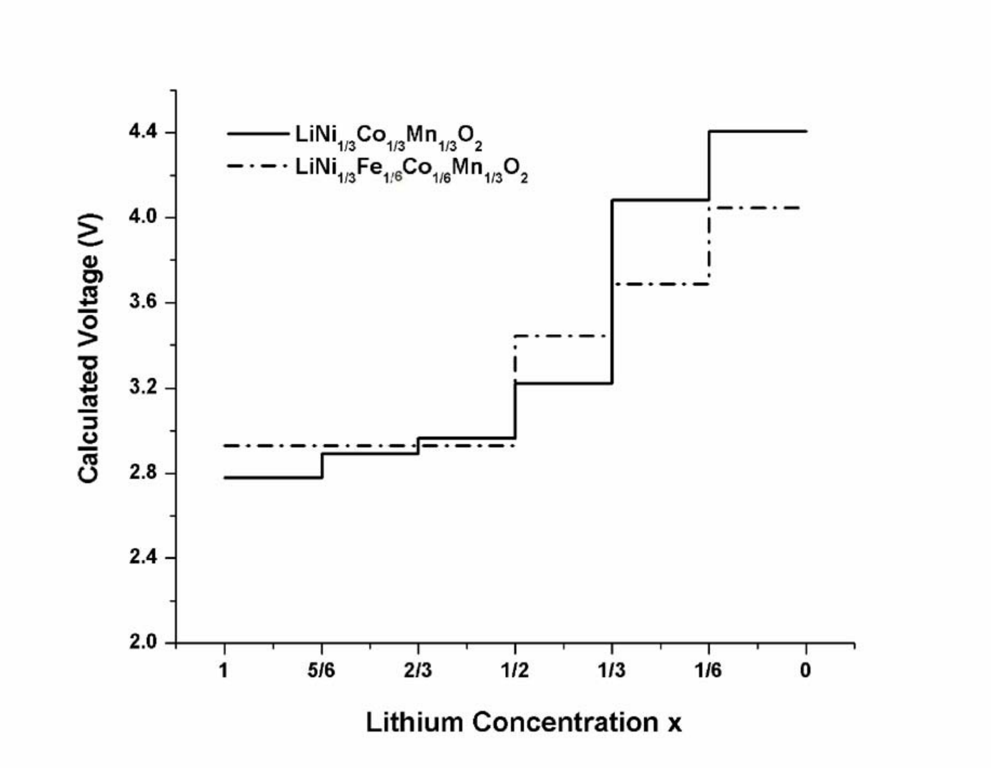

Figure 3-5. Comparison of calculated average voltage curves of$Li_xNi_{1/3}Co_{1/3}Mn_{1/3}O_2$ and $Li_xNi_{1/3}Fe_{1/6}Co_{1/6}Mn_{1/3}O_2$.

3.4.2 Electronic Change during Charge-Discharge

To understand the electronic changes in $LiNi_{1/3}Fe_{1/6}Co_{1/6}Mn_{1/3}O_2$ when lithium is removed, the spin polarized density of states (DOS) at different lithium concentrations is shown in Figure 3-6. Since the transition metal ions occupy the octahedral sites in the sublattices of oxygen ions, 3*d* bands of transition metal ions split into t_{2g} and e_g bands. The calculated DOS, projected onto the orbitals of each transition metal are shown in Figure 3-6.

For all lithium compositions, the Mn-t_{2g} and Mn-e_g bands are respectively, half filled and empty in $Li_xNi_{1/3}Fe_{1/6}Co_{1/6}Mn_{1/3}O_2$ ($0 \le x \le 1$), which is consistent with a Mn^{4+} valence state. For fully lithiated $LiNi_{1/3}Fe_{1/6}Co_{1/6}Mn_{1/3}O_2$ ($x = 1$ in Figure 3-6a), Ni-t_{2g} states are fully occupied and only one spin direction for the Ni-e_g states is occupied. For Fe-t_{2g} and Fe-e_g only the majority spin states are occupied indicating high-spin Fe^{3+}. The Co-t_{2g} states are fully occupied and Co-e_g states are empty, indicative of Co^{3+}. The Fermi level, E_F is located between the top of occupied Co-t_{2g} bands and unoccupied Fe-t_{2g} states. There is an energy gap of about 0.3 eV between the unoccupied and occupied states. Although it is well know that the calculated energy gaps in GGA are typically smaller than the experimental values, the comparison with the calculated energy gap for $LiNi_{1/3}Co_{1/3}Mn_{1/3}O_2$ (0.7V) [7] indicates that the electronic conductivity of $LiNi_{1/3}Fe_{1/6}Co_{1/6}Mn_{1/3}O_2$ may be as good, if not better, as $LiNi_{1/3}Co_{1/3}Mn_{1/3}O_2$.

As we applied a supercell with six-formula units in this study, both Ni^{2+}/Ni^{3+} and Ni^{2+}/Ni^{4+} are possible redox reactions. Figure 3-6a) & b) show that for a partially delithiated state ($2/3 \le x \le 1$), only the Ni^{2+}/Ni^{3+} redox reaction is observed, which is consistent with the previous studies on $LiNi_{1/2}Mn_{1/2}O_2$ and $LiNi_{1/3}Co_{1/3}Mn_{1/3}O_2$. [7, 8, 16] At $x = 2/3$ (Figure 3-6b)), there is an overlap between filled Ni-e_g and Fe-e_g states, indicating very similar redox potentials for Ni and Fe ions. Electrons are simultaneously removed from the Ni-e_g and Fe-e_g bands upon further delithiation as shown in Figure 3-6c). It clearly indicates that the Ni^{3+}/Ni^{4+} and Fe^{3+}/Fe^{4+} redox reactions take place simultaneously. Such simultaneous redox reactions of Fe and Ni have been reported in the $Li(Ni,Fe)O_2$ system by ^{57}Fe Mossbauer and EXAFS investigations. [17, 18] Furthermore, upon delithiation ($1/3 \le x \le 2/3$), the Fe-e_g states become empty and all four valence electrons partially fill Fe-t_{2g} states indicating low-spin for Fe^{4+}. At $x = 0$, an electron is also pulled from the Co-t_{2g} band (Figure 3-6d)), which demonstrates that the redox couple $Co^{3+}/Co^{4+}$is activated at the end of charge.

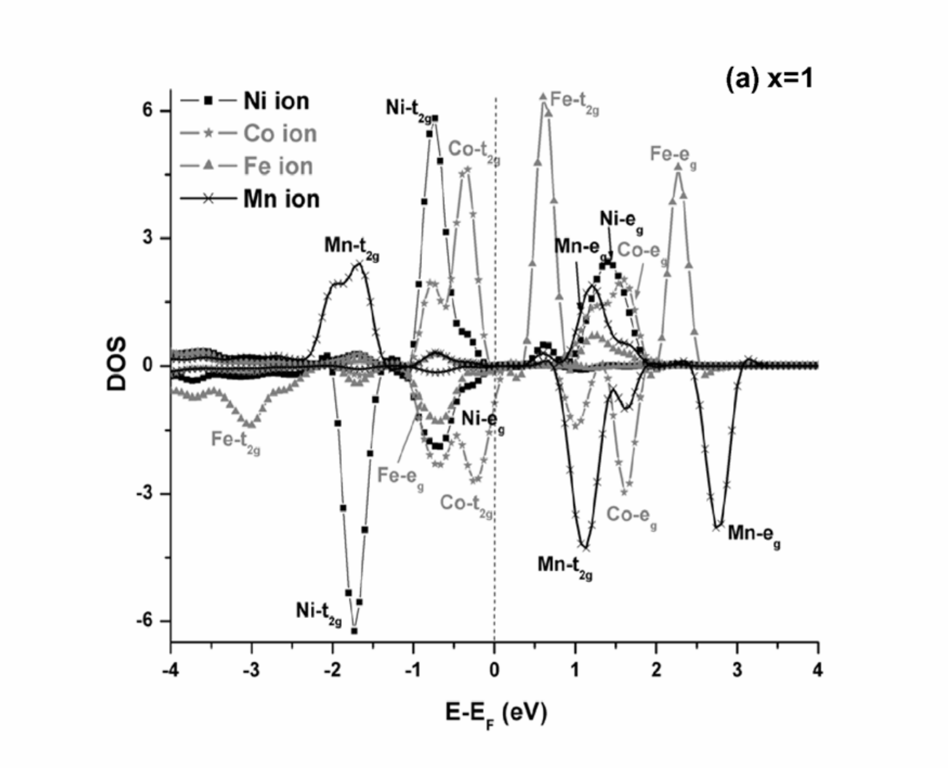
(a) x=1
Ni ion
Co ion
Fe ion
Mn ion
DOS
E-E$_F$ (eV)
6
3
0
-3
-6
-4
-3
-2
-1
0
1
2
3
4
Ni-t$_{2g}$
Co-t$_{2g}$
Fe-t$_{2g}$
Fe-e$_g$
Mn-t$_{2g}$
Ni-e$_g$
Mn-e$_g$
Co-e$_g$
Fe-t$_{2g}$
Ni-e$_g$
Fe-e$_g$
Co-t$_{2g}$
Co-e$_g$
Mn-t$_{2g}$
Mn-e$_g$
Ni-t$_{2g}$

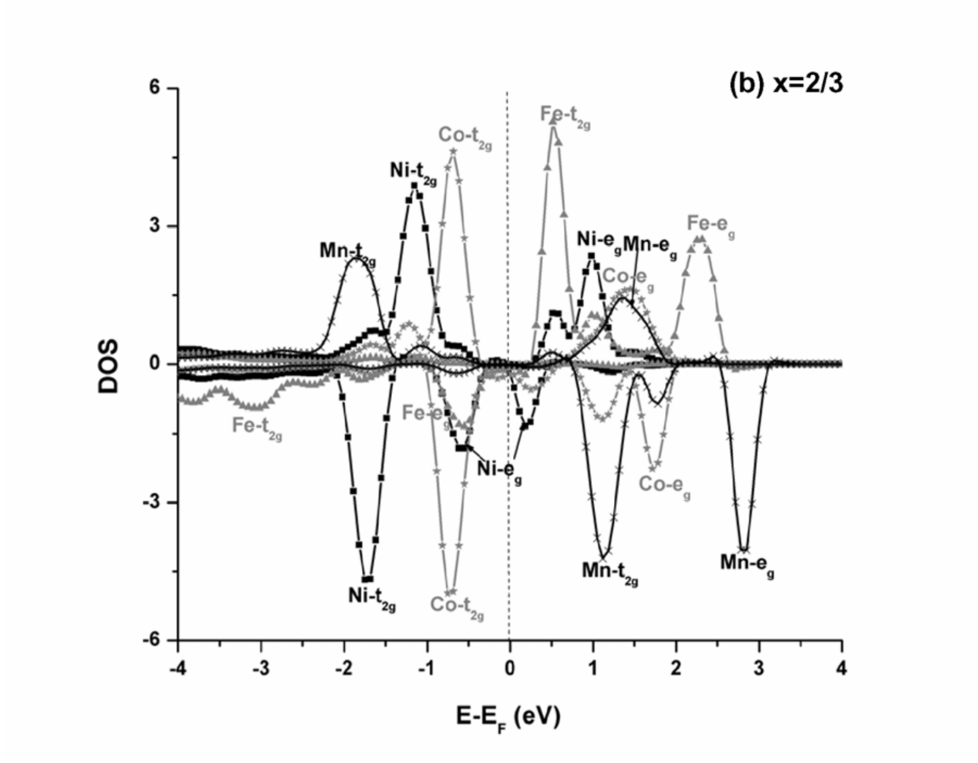
(b) x=2/3
DOS
E-E$_F$ (eV)
6
3
0
-3
-6
-4
-3
-2
-1
0
1
2
3
4
Fe-t$_{2g}$
Co-t$_{2g}$
Ni-t$_{2g}$
Mn-t$_{2g}$
Ni-e$_g$
Mn-e$_g$
Fe-e$_g$
Co-e$_g$
Fe-t$_{2g}$
Fe-e$_g$
Ni-e$_g$
Co-e$_g$
Mn-t$_{2g}$
Mn-e$_g$
Ni-t$_{2g}$
Co-t$_{2g}$

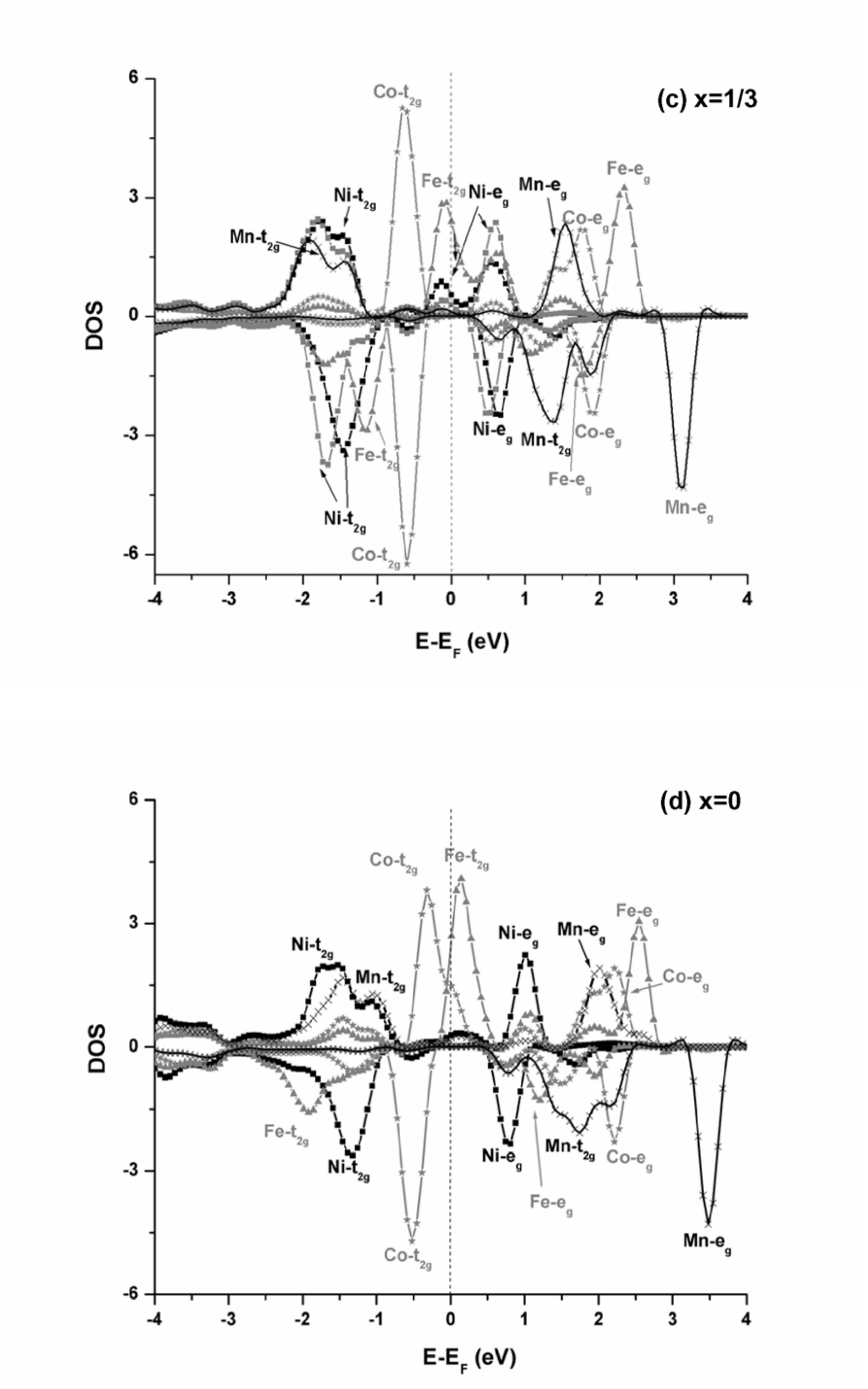

Figure 3-6 Calculated density of states of $Li_xNi_{1/3}Fe_{1/6}Co_{1/6}Mn_{1/3}O_2$ at a) x= 1, b) x = 2/3, c) x= 1/3, and d) x = 0.

3.4.3 Lattice Parameters and Bond Lengths

Table 3-I show the calculated lattice parameters and bond distances of $Li_xNi_{1/3}Co_{1/3}Fe_{1/6}Mn_{1/3}O_2$ at various lithium concentrations. The structural parameters of the most stable states were selected. There is no significant difference in the structural parameters among different Li-vacancy configurations at the same composition.

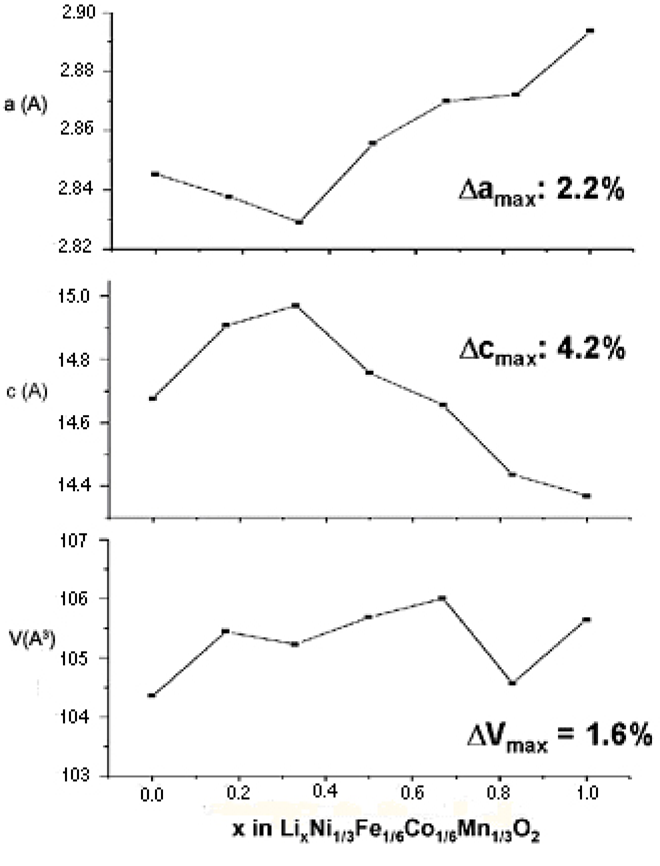

Figure 3-7 Calculated lattice parameter *a* & *c* and volume at various lithium concentrations.

The calculated lattice parameters *a* & *c* of $Li_xNi_{1/3}Co_{1/6}Fe_{1/6}Mn_{1/3}O_2$ at various lithium concentrations are depicted in Figure 3-7. The calculated *a* lattice parameter decreases in the range of $1/3 \le x \le 1$ by approximately 2.2% and increases slightly in the range of $0 \leq x \leq 1/3$. The lattice parameter ***c*** increases by about 4.2% in the range of $1/3 \leq x \leq 1$ and decreases for $0 \leq x \leq 1/3$. The maximum change in cell volume is only 1.6%, which implies that effect of stress and strain in the material during the lithiation – delithiation cycle will be very small; in comparison the volume change of $LiCoO_2$ is about 3 to 4 percent [19].

The bond distances between the transition metal ions and oxygen ions at different lithium contents are also shown in Table 3-I. The average bond distances between the transition metal ions and oxygen ions at different lithium contents are plotted in Figure 3-8. The bond distances of Ni-O and Mn-O in fully-lithiated $Li_xNi_{1/3}Fe_{1/6}Co_{1/6}Mn_{1/3}O_2$ material (x = 1) are [2×2.04 2.05 2×2.06 2.07] Å, [2.06 2.07 2.08 3×2.09] Å and [1.93 4×1.94 1.95] Å, [3×1.93 1.94 2×1.95] Å, respectively. The bond distance of Ni-O is much longer than that of Mn-O, indicating Ni has oxidation state of 2+ in this material. Fe-O has similar bond distances as Ni-O [2.04 4×2.05 2.06] Å, which can be explained by the similar size of Fe^{3+} and Ni^{2+} [Shannon radius] [20]. Co-O has the typical bond distance of Co^{3+} in the layered compound [21].

As lithium is removed, in the range of $2/3 \leq x \leq 1$, Ni^{2+} is oxidized and the bond distances of Ni-O become shorter. The large spread of bond lengths for Ni-O in his range is due to Jahn-Teller distortion of $Ni^{III}O_6$ octahedron. Note that this also affects the Fe-O and Mn-O bond lengths. Such distortion disappears upon further lithium removal: in the range of $1/3 \leq x \leq 2/3$, the Fe-O (Figure 3-8c)) and Ni-O (Figure 3-8a) & b)) bond distances reduce simultaneously, which is in good agreement with the DOS observations in Figure 3-6. In addition, in this range ($1/3 \leq x \leq 2/3$) the decrease in Fe-O bonds distance changes the crystal field splitting between the e_g and t_{2g} bands [22], which leads to low-spin of Fe^{4+}, as mentioned previously.

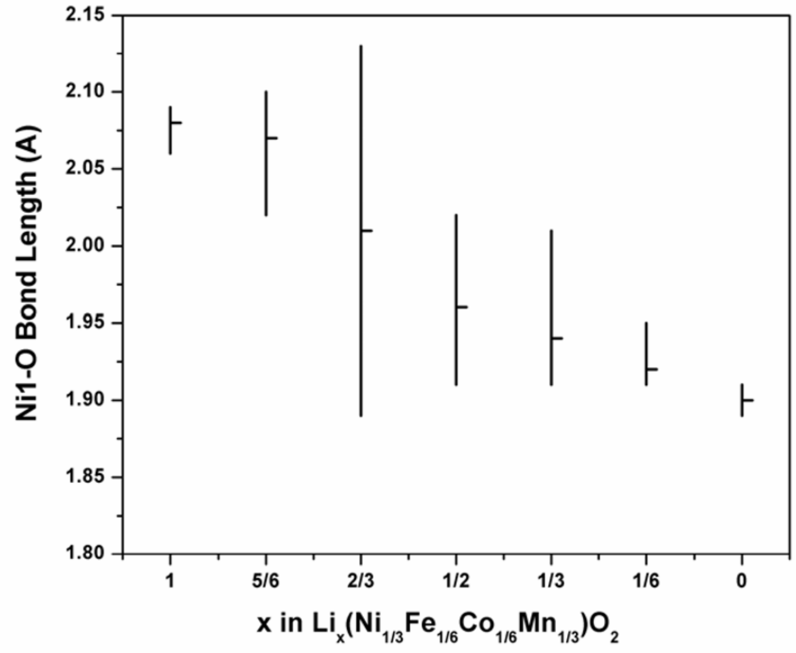

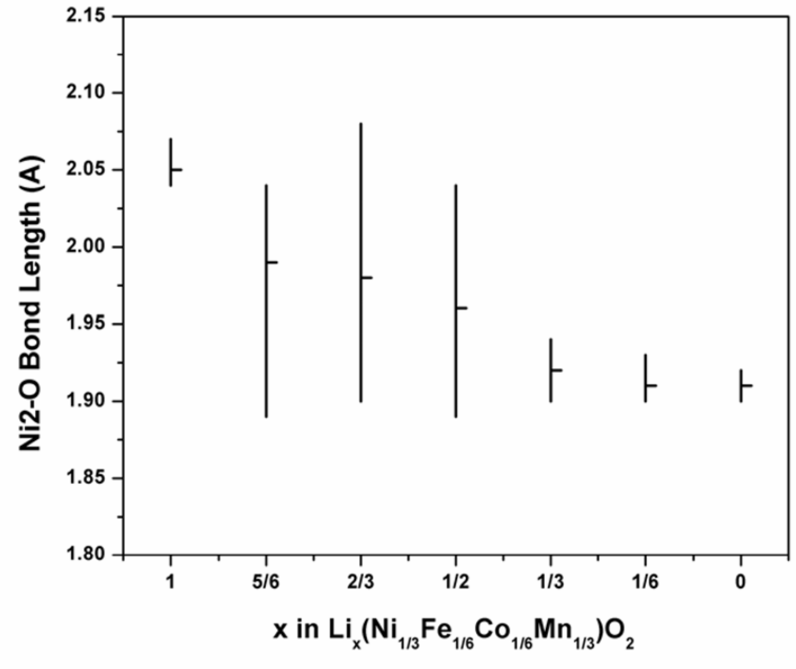

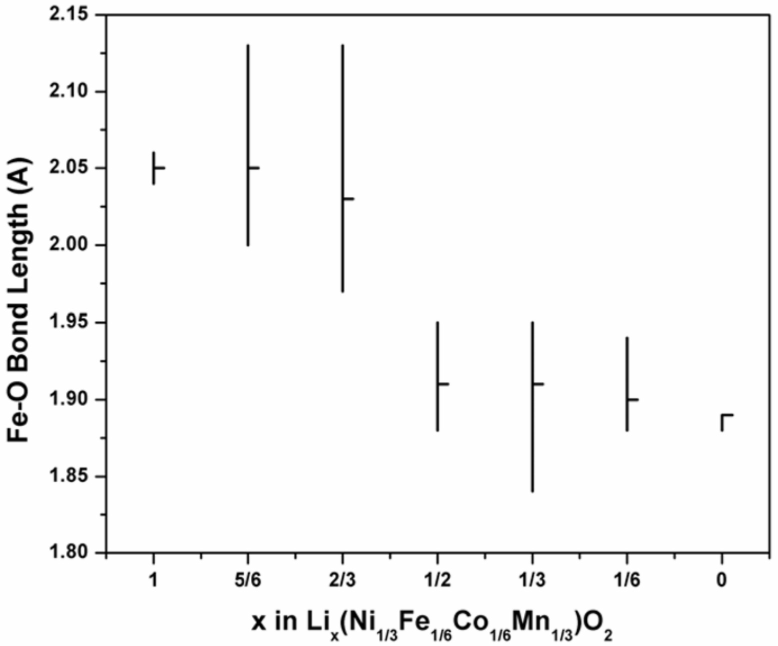
Fe-O Bond Length (A)
2.15
2.10
2.05
2.00
1.95
1.90
1.85
1.80
1
5/6
2/3
1/2
1/3
1/6
0
x in $Li_x(Ni_{1/3}Fe_{1/6}Co_{1/6}Mn_{1/3})O_2$

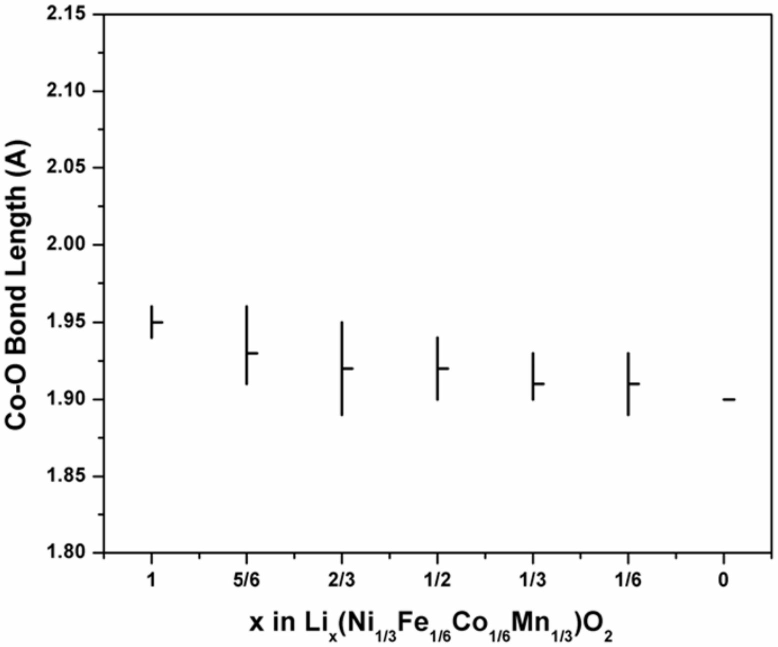
Co-O Bond Length (A)
2.15
2.10
2.05
2.00
1.95
1.90
1.85
1.80
1
5/6
2/3
1/2
1/3
1/6
0
x in $Li_x(Ni_{1/3}Fe_{1/6}Co_{1/6}Mn_{1/3})O_2$

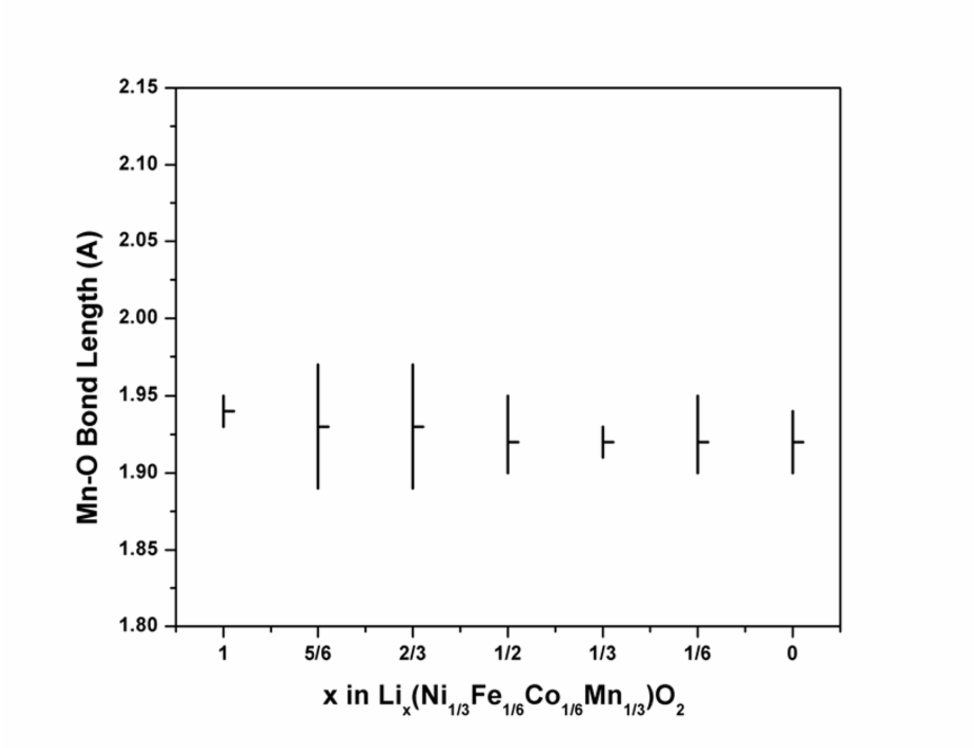

Figure 3-8. Calculated transition metal - oxygen bond lengths (TM-O distances) of $Li_xNi_{1/3}Fe_{1/6}Co_{1/6}Mn_{1/3}O_2$ ($0 \le x \le 1$)

Table 3-1 Calculated lattice parameters and transition metal –oxygen bond distances of $Li_xNi_{1/3}Co_{1/6}Fe_{1/6}Mn_{1/3}O_2$

$Li_xNi_{1/3}Co_{1/6}Fe_{1/6}Mn_{1/3}O_2$	**1**	**5/6**	**2/3**	**1/2**	**1/3**	**1/6**	**0**
a (Å)	2.9138	2.8922	2.8901	2.8758	2.8490	2.8578	2.8653
c (Å)	14.3690	14.4359	14.6552	14.7569	14.9709	14.9086	14.6775
Ni-O (Å)	2×2.04 2.05 2×2.06 2.07	2.02 2×2.06 2.09 2×2.10	1.90 1.91 1.96 1.97 2.07 2.08	1.91 1.93 1.95 1.96 2.01 2.02	2×1.91 1.92 1.93 1.97 2.01	5×1.91 1.95	2×1.89 4×1.91
	2.06 2.07 2.08 3×2.09	1.89 1.91 2.02 2.03 2×2.04	1.89 1.91 1.99 2.03 2.08 2.13	1.89 1.91 2×1.94 2.03 2.04	2×1.90 1.91 1.93 2×1.94	2×1.90 1.91 2×1.92 1.93	4×1.90 2×1.92
Co-O (Å)	2×1.94 3×1.95 1.96	1.91 2×1.92 1.94 1.95 1.96	1.89 1.90 3×1.93 1.95	2×1.90 1.91 1.92 1.93 1.94	3×1.90 1.91 1.92 1.93	2×1.89 1.90 2×1.91 1.93	6×1.90
Fe-O (Å)	2.04 4×2.05 2.06	2×2.00 2.03 2.04 2.09 2.13	1.97 1.98 2.03 2.04 2.05 2.14	1.88 1.89 2×1.91 1.92 1.95	1.84 1.89 1.91 1.93 2×1.95	1.88 3×1.89 1.90 1.94	1.88 5×1.89
Mn-O (Å)	1.93 4×1.94 1.95	1.89 1.90 1.92 1.95 1.96 1.97	1.89 1.91 1.93 2×1.95 1.97	1.91 1.92 3×1.93 1.95	1.91 2×1.92 3×1.93	2×1.90 2×1.92 1.94 1.95	2×1.90 2×1.91 1.93 1.94
	3×1.95 1.94 2×1.95	2×1.89 2×1.94 2×1.96	1.86 1.91 1.92 1.95 2×1.96	2×1.90 2×1.92 1.93 1.95	1.90 2×1.92 1.93 2×1.94	1.89 1.91 2×1.92 1.93 1.94	2×1.90 2×1.92 2×1.93

3.5 Conclusions

Prescreening with Density Functional Theory to sort through potential cathode materials based on their Li intercalation potentials and electronic structures was carried on $LiNi_{1/3}TM1_{1/3}TM2_{1/3}O_2$ systems, where TM1 is a 3+ transition metal (Co^{3+}, Al^{3+}, Fe^{3+} etc.) and TM2 is a 4+ transition metal (Ti^{4+}, Zr^{4+}, Mn^{4+} etc.). Fe substitution is found to be advantageous because among the compounds investigated it shows the lowest voltage at the last stage of the charge. The structural and electronic changes of $LiNi_{1/3}Fe_{1/6}Co_{1/6}Mn_{1/3}O_2$ with various lithium concentrations were investigated by first principles methods. Fe/Co substituted lithium nickel manganese oxides can be considered as potential cathode materials and their synthesis and characterization will be presented in the next chapter.

References:

1. C. Wolverton and A. Zunger, *Prediction of Li intercalation and battery voltages in layered vs. Cubic* Li_xCoO_2. J. Electrochem. Soc., 1998. **145**(7): p. 2424-2431.
2. G. Ceder , et al., *Identification of cathode materials for lithium batteries guided by first-principles calculations.* Nature, 1998. **392**: p. 694-666.
3. S.K. Mishra and G. Ceder, *Structural stability of lithium manganese oxides.* Physical Review B - Condensed Matter, 1999. **59**(9): p. 6120-6130.
4. D. deFontaine, in *Solid State Physics*, E.H.T. D., Editor. 1994, Academic Press: New York.
5. A.J. Bard and L.R. Faulkner, *Electrochemical Methods: Fundamentals and Applications*. 2001, New York: John Wiley & Sons, Inc.
6. K.M. Shaju, G.V.S. Rao, and B.V.R. Chowdari, *Performance of layered* $Li(Ni_{1/3}Co_{1/3}Mn_{1/3})O_2$ *as cathode for Li-ion batteries.* Electrochimica Acta, 2002. **48**(2): p. 145-151.
7. Hwang, B.J., et al., *A combined computational/experimental study on* $LiNi_{1/3}Co_{1/3}Mn_{1/3}O_2$. Chemistry of Materials, 2003. **15**(19): p. 3676-3682.
8. J. Reed and G. Ceder, *Charge, potential, and phase stability of layered* $Li(Ni_{0.5}Mn_{0.5})O_2$. Electrochemical and Solid State Letters, 2002. **5**(7): p. A145-A148.
9. M.K. Aydinol, et al., *Ab initio study of lithium intercalation in metal oxides and metal dichalcogenides.* Physical Review B, 1997. **56**(3): p. 1354-1365.
10. F. Zhou, et al., *Phase separation in* Li_xFePO_4 *induced by correlation effects.* Physical Review B, 2004. **69**(20).
11. F. Zhou, et al., *The electronic structure and band gap of* $LiFePO_4$ *and* $LiMnPO_4$. Solid State Communications, 2004. **132**: p. 181-186.
12. J.N. Reimers, et al., *Structure and electrochemistry of* $Li_xFe_yNi_{1-y}O_2$. Solid State Ionics, 1993. **61**: p. 335-344.
13. R. Kanno, et al., *Synthesis and electrochemical properties of lithium iron oxides with layer-related structures.* Journal of Power Sources, 1997. **68**(1): p. 145-152.
14. G. Prado, et al., *Electrochemical behaviour of iron substituted lithium nickelate.* J. Electrochem. Soc., 2000. **147**(8): p. 2880.
15. C. Delmas, et al., *An overview of the* $Li(Ni,M)O_2$ *systems : syntheses, structures and properties.* Electrochimica Acta, 1999. **45**: p. 243-253.
16. Arachi, Y., et al., *Structural change of* $Li_{1-x}Ni_{0.5}Mn_{0.5}O_2$ *cathode materials for lithium-ion batteries by synchrotron radiation.* Chemistry Letters, 2003. **32**(1): p. 60-61.
17. A. Demourgues, *(Fe,Co,Ni) K-edge EXAFS study of* $Lix(Ni_{1-y}M_y)O_2$ *(M = Fe, Co) phases : effect of the lithium content and the cation substitution on the Ni(III) Jahn-Teller distorsion*. in *Lithium Batterie Discussion*. 2001. Arcachon.
18. G. Prado, L. Fournès, and C. Delmas, *On the* $Li_xNi_{0.70}Fe_{0.15}Co_{0.15}O_2$ *cathode material.* Journal of Solid State Chemistry, 2001. **159**: p. 103.
19. T. Ohzuku and A. Ueda, *Solid-state redox reactions of* $LiCoO_2$ *(R-3m) for 4 volt secondary lithium cells.* J. Electrochem. Soc., 1994. **141**(11): p. 2972-2977.
20. R.D. Shannon and C.T. Prewitt, *Revised Effective Ionic Radii in Halides and Chalcogenides,* Acta Crystallographica, 1969. **B25**: p. 925.

21. Y. Koyama, et al., *Crystal and electronic structures of superstructural* $Li_{1-x}Co_{1/3}Ni_{1/3}Mn_{1/3}O_2$ *(*$0 \leq x \leq 1$*)*. Journal of Power Sources, 2003. **119**: p. 644-648.
22. B.N. Figgis and M.A. Hitchman, *Ligand Field Theory and Its Applications*. 2000, New York: Wiley-VCH.

CHAPTER 4

SYNTHESIS, CHARACTERIZATION & ELECTROCHEMICAL TESTING OF FE/CO SUBSTITUTED LITHIUM NICKEL MANGANESE OXIDES

As demonstrated in the previous chapter, Fe substitution in the $LiNi_{1/3}\mathbf{TM1}_{1/3}Mn_{1/3}O_2$ system (**TM1** = Co^{3+}, Fe^{3+}, Al^{3+} etc) is found to be advantageous because it has a relatively low voltage according to the first principles study, which means possibly higher accessible capacity in the practical voltage range. Motivated by the first principles computation based on Density Functional Theory, experimental studies of the system $LiNi_{1/3}Fe_zCo_{1/3-z}Mn_{1/3}O_2$ were carried out. In this chapter, we will show how these potential cathode materials were synthesized, characterized and optimized with the guidance of first principles method. Experimental results on their Li intercalation voltages, crystal structures and electronic structures will be compared with the computationally predicted values. We hope to demonstrate that the direct integration of first principles computation with various experimental techniques helps to shorten the development cycle of the cathode material in lithium ion batteries.

4.1 Guided Synthesis

It is well-known that due to the similar ion size of Fe^{3+} and Li^+, the Fe can partially occupy Li sites in the Li layer [1, 2]. In addition, unlike $LiCoO_2$ and $LiNiO_2$, the

$LiFeO_2$ ground state structure is a rocksalt structure with space group $I4_1/amd$ [3]. According to the preliminary mixing enthalpy calculations using the equation below, the relative formation energy of $LiNi_{1/3}Fe_{1/3}Mn_{1/3}O_2$ with respect to $LiNi_{1/2}Mn_{1/2}O_2$ and $LiFeO_2$ is approximately zero, indicating that only a weak entropic driving force for mixing might exist in a compound where Co is fully substituted by Fe.

$$\Delta E_{mix} = E_{LiNi_{1/3}Fe_zCo_{1/3-z}Mn_{1/3}O_2} - [\tfrac{2}{3} E_{LiNi_{1/2}Mn_{1/2}O_2} + zE_{LiFeO_2} + (\tfrac{1}{3} - z)E_{LiCoO_2}] \qquad \text{Eq. 4 – 1}$$

Therefore, we chose to substitute Co only partially by Fe and targeted the nominal composition range $LiNi_{1/3}Fe_zCo_{1/3-z}Mn_{1/3}O_2$ ($0 \leq z \leq 1/3$) in order to obtain the composition limit by which a pure single-phase layered material.

$LiNi_{1/3}Fe_zCo_{1/3-z}Mn_{1/3}O_2$ ($0 \leq z \leq 1/3$) cathode materials were synthesized by the sol-gel method. Four particular compositions were chosen $LiNi_{1/3}Fe_{1/9}Co_{2/9}Mn_{1/3}O_2$ ($z = 1/9$), $LiNi_{1/3}Fe_{1/6}Co_{1/6}Mn_{1/3}O_2$ ($z = 1/6$) and $LiNi_{1/3}Fe_{2/9}Co_{1/9}Mn_{1/3}O_2$ ($z = 2/9$) and $LiNi_{1/3}Fe_{1/3}Mn_{1/3}O_2$ ($z = 1/3$). The sol-gel method has been largely used for producing materials with high purity and high homogeneity while employing low synthesis temperatures. It has been widely applied in synthesis of the multi cation cathode materials. In the process, atomic level mixing among the precursors can be achieved, thus sol-gel method is chosen for this work in order to obtain pure single phase layered compound.

$LiNi_{1/3}Fe_zCo_{1/3-z}Mn_{1/3}O_2$ ($0 \leq z \leq 1/3$) powders were synthesized by the sol-gel method using citric acid as a chelating agent. A stoichiometric amount of lithium acetate ($Li(CH_3COO)\bullet 2H_2O$), nickel acetate ($Ni(CH_3COO)_2\bullet 4H_2O$), cobalt nitrate ($Co(NO_3)_2\bullet 6H_2O$), iron nitrate ($Fe(NO_3)_3\bullet 9H_2O$) and manganese acetate

($Mn(CH_3COO)_2 \bullet 4H_2O$) were dissolved in distilled water and well mixed with an aqueous solution of citric acid. The solution was stirred at 60-70°C for 5-6 hours to obtain a clear viscous gel. The gel was dried in a vacuum oven at 120°C for 24 hours. All the $LiNi_{1/3}Fe_zCo_{1/3-z}Mn_{1/3}O_2$ compounds were precalcined in two stages: at 350°C for 5 hours and 450°C for 4 hours and ground before they were calcined at high temperatures (650-950°C) at a heating rate of about 2°C/min. The powders were slowly cooled to room temperature in oxygen. The overall flow of the synthesis process is illustrated in Figure 4-1.

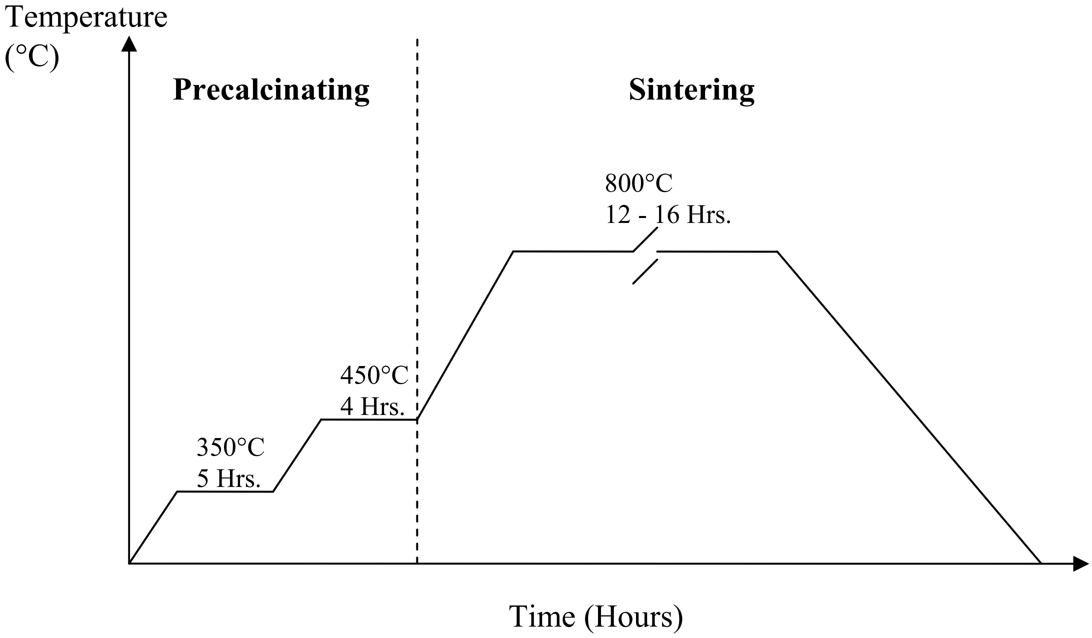

Figure 4-1 Process flow of heat treatment

4.2 Characterization of As-Synthesized Materials

4.2.1 Powder X-ray Diffraction

Powder X-ray diffraction data were collected on a Rigaku diffractometer with Cu Kα1 radiation (λ = 1.5406 Å), operating at 300kV and 60mA. To minimize the preferred orientation effect, typical in layered lithium intercalation compound, Vaseline is mixed with sample powders to randomize the particles.

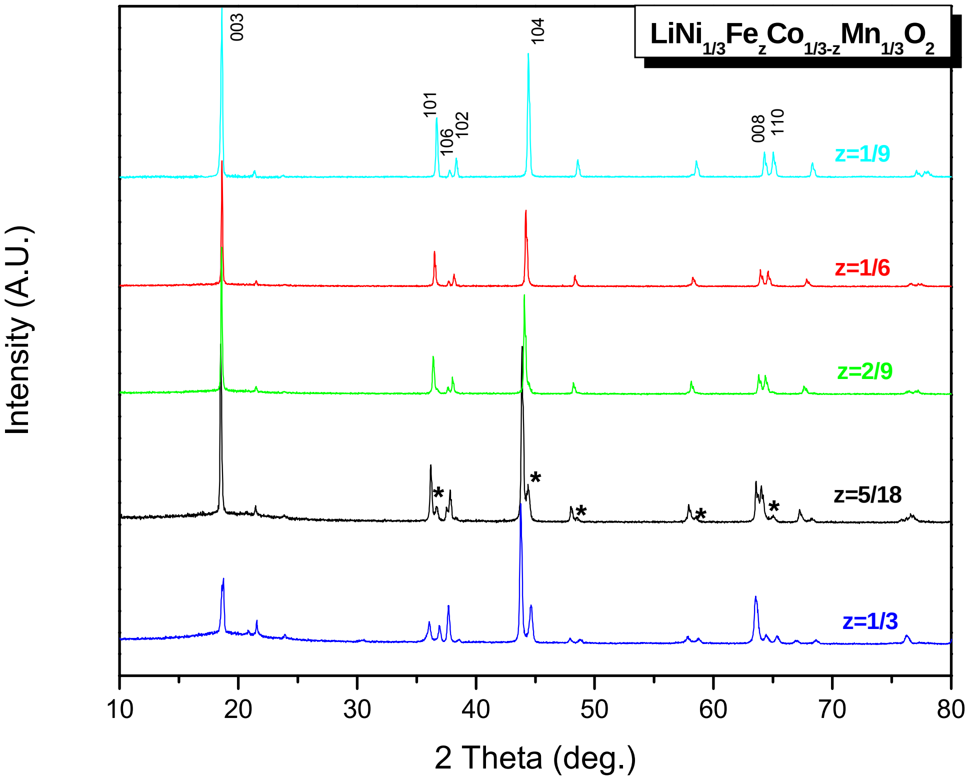

Figure 4-2 XRD spectra for $LiNi_{1/3}Fe_zCo_{1/3-z}Mn_{1/3}O_2$ at z = 1/9, z = 1/6, z = 2/9, z = 5/18, z = 1/3, all synthesized at 850°C.

XRD spectra of $LiNi_{1/3}Fe_zCo_{1/3-z}Mn_{1/3}O_2$ for z = 0, z = 1/6, z = 2/9, z = 5/18, z = 1/3, all synthesized at 850°C are shown in Figure 4-2. X-ray diffraction study shows that when $z \leq 2/9$, a typical layered structure with R-3m space group is obtained; when z = 5/18 and z = 1/3, another non-layered impurity phase is present contributing to the peaks with *.

Figure 4-3 shows the XRD spectra of $LiNi_{1/3}Fe_{1/6}Co_{1/6}Mn_{1/3}O_2$ synthesized at 750°C, 800°C and 850°C. Due to instrument limitation, which requires sample powders to be pressed in the vertical sample holder, even with Vaseline blending; we cannot evaluate the layered property of the compounds by comparing the peak ratio of I_{003}/I_{104} due to the preferential orientation associated with the pressing. Instead, the clear peak splitting of (108) and (110) can be used to confirm that good layered structures have been obtained. (Rietveld refinement of the powder XRD data was done in another instrument, which will be discussed in detail later) (104) peak for the three compounds is closely examined, as shown in Figure 4-3b), when the synthesis temperature goes up to 850°C, another phase is evolving, evident by an obvious hump right beside the main peak. For samples synthesized below 700°C, poorly crystallized powders were obtained.

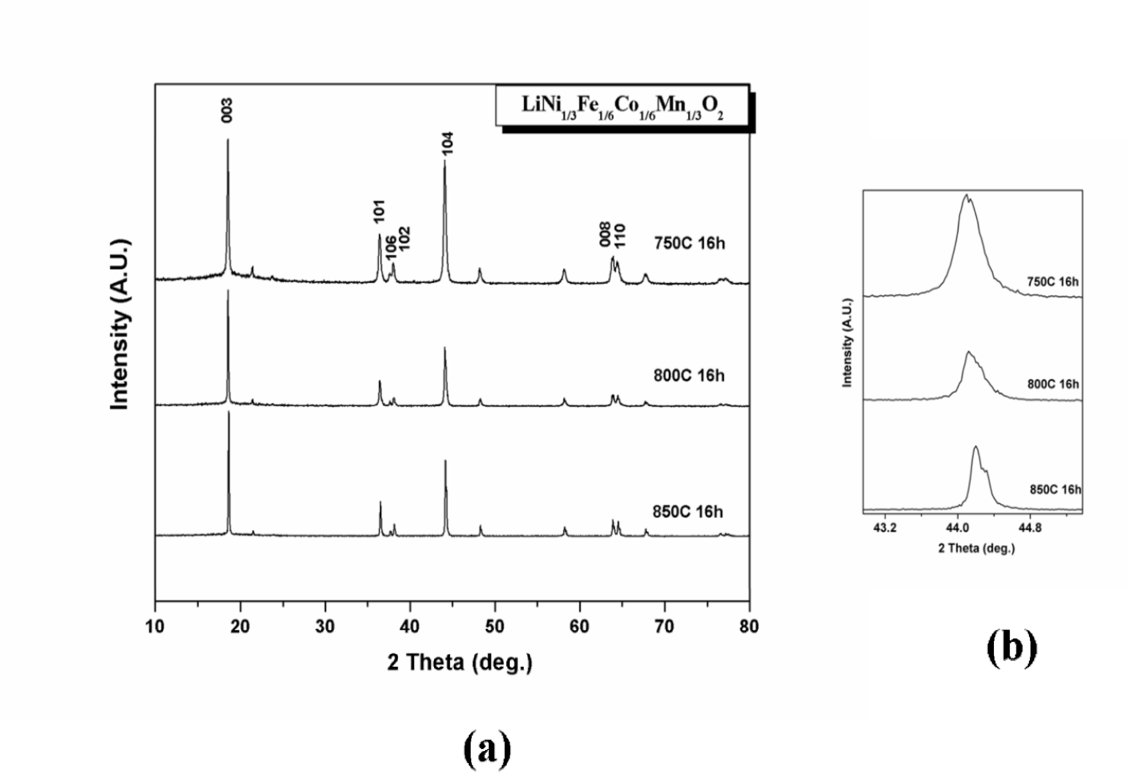

Figure 4-3 XRD spectra of $LiNi_{1/3}Co_{1/6}Fe_{1/6}Mn_{1/3}O_2$ synthesized at 750°C, 800°C and 850°C

The optimum synthesis temperature and time for $LiNi_{1/3}Co_{1/3}Mn_{1/3}O2$ is about 900°C and 12 hours, respectively [4] . Such synthesis condition is commonly applied in lithium nickel manganese oxides, such as $LiNi_{1/2}Mn_{1/2}O_2$. However, in order to obtain pure layered structure in Fe substituted compounds, the synthesis temperature has to be lowered. This fact will be further discussed in terms of the electrochemical properties of the compound synthesized at different temperatures.

4.2.2 Scanning Electron Microscopy

Grain morphology and particle size of $LiNi_{1/3}Fe_zCo_{1/3-z}Mn_{1/3}O_2$ compounds were examined by scanning electron microscopy using a JEOL FEG - 6320. The effects of Fe substitution of Co, as well as the sintering temperatures on the grain morphology and size have been carefully studied.

Scanning electron micrographs of $LiNi_{1/3}Fe_zCo_{1/3-z}Mn_{1/3}O_2$ $z = 1/6$, $z = 2/9$, $z = 1/3$ all synthesized at 850°C for 16 hours were collected and shown in Figure 4-4. Uniform grain size and faceted grain morphology are observed for $LiNi_{1/3}Fe_{1/6}Co_{1/6}Mn_{1/3}O_2$ and $LiNi_{1/3}Fe_{2/9}Co_{1/9}Mn_{1/3}O_2$ compounds, where a single layered structure is present, according to the XRD spectra in Figure 4-2. In the Co-free sample $LiNi_{1/3}Fe_{1/3}Co_{1/3}O_2$ ($z = 1/3$) Figure 4-4c), many small non-faceted particles are surrounding the large faceted crystals. The presence of two distinct powder morphologies is a strong indication of two different phases present in the material.

A comparison of SEM micrographs obtained for $LiNi_{1/3}Fe_{1/6}Co_{1/6}Mn_{1/3}O_2$ synthesized at 750°C, 800°C and 850°C is shown in Figure 4-5. The grain size increases from 40-50 nm to 400-500nm as the synthesis temperature raises from 750°C to and 850°C. All samples have a uniform grain size and faceted grain morphology.

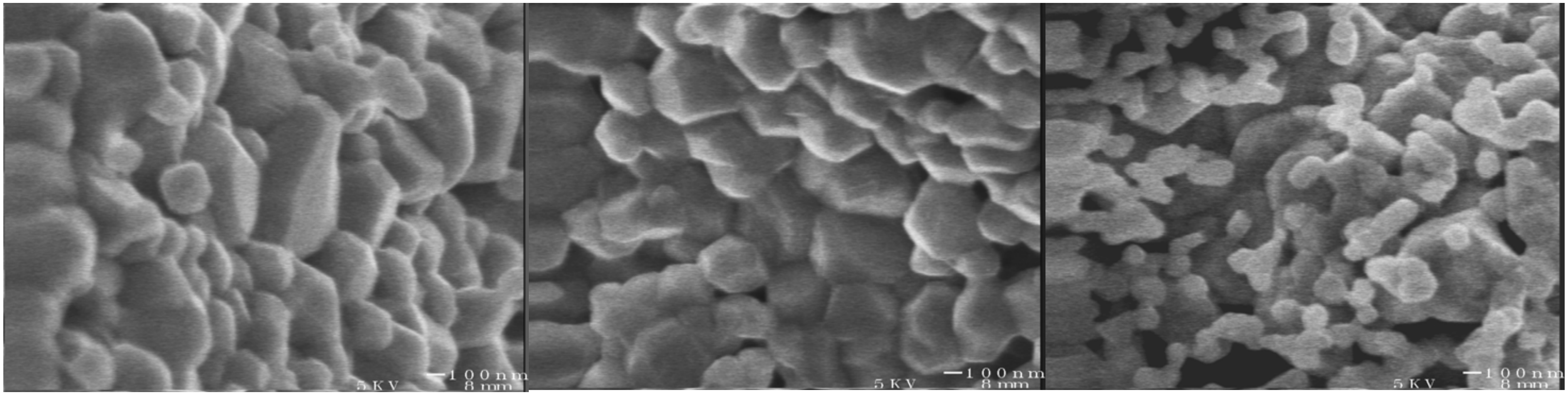

(a) (b) (c)

Figure 4-4 SEM images of as-prepared $LiNi_{1/3}Fe_zCo_{1/3-z}Mn_{1/3}O_2$ at (a) z=1/6, (b) z=2/9, (c) z=1/3, all synthesized at 850°C.

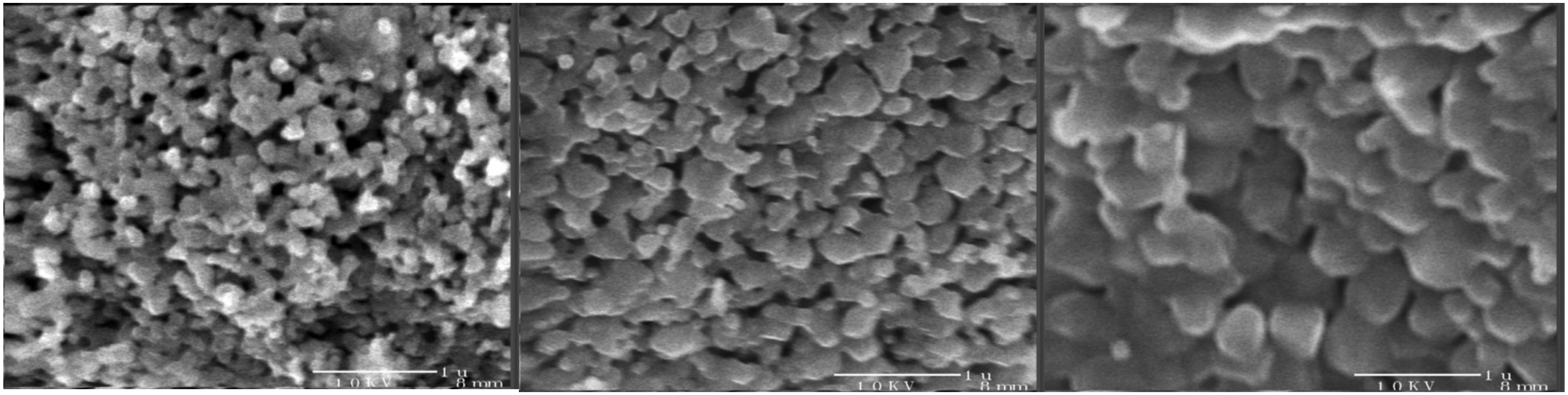

(a) (b) (c)

Figure 4-5. SEM images of as-prepared $LiNi_{1/3}Co_{1/6}Fe_{1/6}Mn_{1/3}O_2$ materials synthesized at (a) 750ºC (b) 800ºC and (c) 850ºC

4.2.3 Rietveld Refinement of Powder XRD Data

Rietveld refinement is a method for analyzing XRD patterns by means of a curve-fitting procedure. The least-squares procedure includes the refinement of conventional parameters, such as scale factor, atomic coordinates and temperature factors, and additional parameters such as the lattice parameters, zero-point error for the detector etc. The Rietveld method is a powerful tool, but it is limited by the drawback that affects powder methods in general: the loss of information that arises from the compression of the three-dimensional diffraction pattern into a single dimension. It is important to realize the fact that the Rietveld method is a technique for refining structures and does not, by itself, constitute a method for structure determination. It requires a good starting structure model for successful convergence. In $LiNi_{1/3}Fe_zCo_{1/3-z}Mn_{1/3}O_2$ compounds, R-3m – typical structure for O3 type layered transition metal oxide is applied in all refinement procedures. It is assumed there is no cation ordering in the transition metal layer.

Table 4-I. Refined lattice parameters of as-prepared materials

	a_{exp}	c_{exp}	a_{cal}	c_{cal}
$LiNi_{1/3}Fe_{1/9}Co_{2/9}Mn_{1/3}O_2$	2.8788	14.3002		
$LiNi_{1/3}Fe_{1/6}Co_{1/6}Mn_{1/3}O_2$	2.8859	14.3222	2.9138	14.3690
$LiNi_{1/3}Fe_{2/9}Co_{1/9}Mn_{1/3}O_2$	2.8933	14.3470		-

The powder XRD data for the Rietveld refinement were collected by a SIEMENS D5000 diffractometer with Cu Kα1 radiation ($\lambda = 1.5406$ Å), operating at 40kV and 40mA. The diffractometer has a sample holder with horizontal orientation. Special care was taken in sample preparation to minimize the preferred orientation effect.

Data for 2theta range of 5-120° was collected with step time 40 seconds and step size 0.02, the 64-hour data collection procedure ensured the high quality (resolution) data for the Rietveld refinement.

The Rietveld refinement data for samples where x = 1/9 and x=1/6 is summarized in Table 4-II.

Table 4-II. Rietveld refinement parameters for $LiNi_{1/3}Fe_{1/9}Co_{2/9}Mn_{1/3}O_2$ and $LiNi_{1/3}Fe_{1/6}Co_{1/6}Mn_{1/3}O_2$

	Li/M n.r.	**$a_{hex.}$ (Å)**	**$c_{hex.}$ (Å)**	**$z_{ox.}$**	**k**	**R_B (%)**	**Rwp (%)**
$LiNi_{1/3}Fe_{1/9}Co_{2/9}Mn_{1/3}O_2$	1.02	2.8788	14.3002	0.2579	0.051	3.9	13.3
$LiNi_{1/3}Fe_{1/6}Co_{1/6}Mn_{1/3}O_2$	1.02	2.8859	14.3222	0.2580	0.064	4.2	12.1

4.2.4 X-ray Photoelectron spectroscopy

Information of nickel, cobalt, iron and manganese oxidation states in three as-synthesized samples (z = 0, z = 1/6 and z = 2/9) were obtained from X-ray photoelectron spectroscopy (XPS) on the pristine powders. Binding energies were charge-corrected using the C_{1s} peak (285 eV).

XPS is based on the photoelectric effect where the concept of the photon was used to describe the ejection of electrons from a surface when photons impinge upon it. For XPS, Al Kα (1486.6eV) or Mg Kα (1253.6eV) is often the photon energies of choice. In this work, an Al source was used. The XPS technique is highly surface specific due to the short range of the photoelectrons that are excited from the solid. The penetration depth in solid samples is about 10-100 Å. The energy of the photoelectrons leaving the sample are determined using a *Concentric Hemispherical Analyzer* (CHA) and this gives a spectrum with a series of photoelectron peaks. The binding energies of the peaks are characteristics of each element. The peak areas can be used (with appropriate sensitivity factors) to determine the composition of the materials surface. The shape of each peak and the binding energy can be slightly altered by the chemical state of the emitting atom. Hence XPS can provide chemical bonding information as well. XPS is not sensitive to hydrogen or helium, but can detect all other elements. XPS must be carried out in ultra-high vacuum (UHV) conditions.

X-ray Photoelectron Spectroscopy XPS (Al source) results for $LiNi_{1/3}Fe_zCo_{1/3-z}Mn_{1/3}O_2$ cathode materials revealed that the oxidation state of Ni, Mn, Fe and Co in the as-synthesized samples are 2+, 4+, 3+ and 3+, respectively, which is consistent with the first-principle computation results. The binding energies of those cations in the as-prepared compounds are tabulated in Table 4-III.

Shift in binding energy with respect to elemental Fe (the binding energies of Fe $2p_{3/2}$ is about 706 ~708eV [5], 707eV is taken as the reference point for comparison) is decided by the valence state of the Fe; while the chemical environment of the Fe, in this case, the Fe-O polyhedron, determines the peak shape. The binding energies of cations in $LiNi_{1/3}Fe_zCo_{1-z}Mn_{1/3}O_2$ for z = 1/6, 2/9 and 1/3 are similar, although there is detectable peak-shape difference in Fe-edge spectra in $LiNi_{1/3}Fe_{1/3}Mn_{1/3}O_2$ (z = 1/3) compared with the other two (z = 1/6 & 2/9), as shown in Figure 4-6. Notice in

Figure 4-6c), there is a small hump in between the $Fe2p_{3/2}$ and $Fe2p_{1/2}$ peaks in $LiNi_{1/3}Fe_{1/3}Mn_{1/3}O_2$. And this hump starts to evolve in $LiNi_{1/3}Fe_{2/9}Co_{1/9}Mn_{1/3}O_2$, though it is not obvious. It is an indication of different Fe local environments in those compounds.

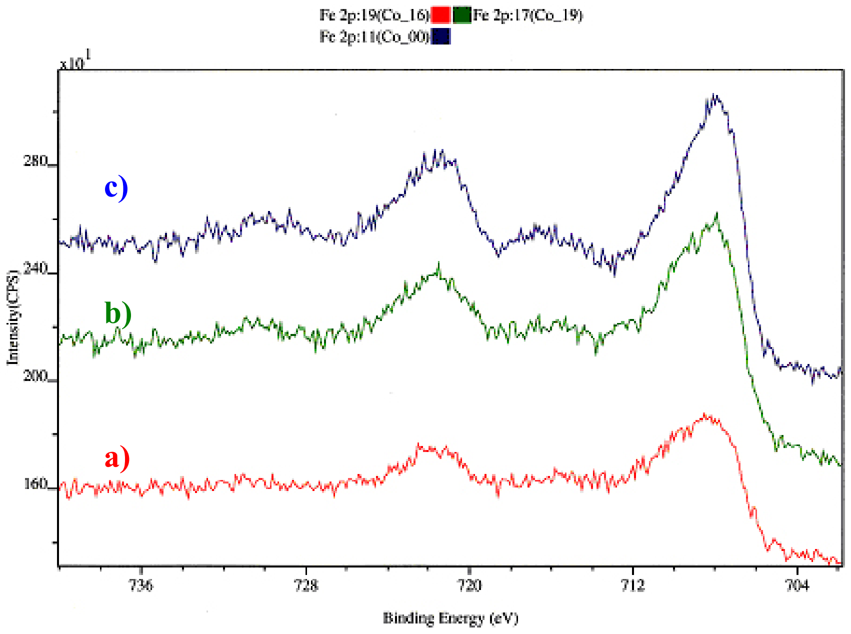

Figure 4-6 XPS spectra of Fe-edge (uncorrected) in $LiNi_{1/3}Fe_zCo_{1/3-z}Mn_{1/3}O_2$ a) z = 1/6, b) z = 2/9 and c) z = 1/3, all synthesized at 850ºC

Table 4-III XPS binding energy for as-prepared materials

	Ni $2p_{3/2}$/eV	Fe $2p_{3/2}$/eV	Co $2p_{3/2}$/eV	Mn $2p_{3/2}$/eV
$LiNi_{1/3}Fe_{1/6}Co_{1/6}Mn_{1/3}O_2$	854.7 (1.7)	710.9 (3.9)	780.4(1.6)	842.3 (3.3)
$LiNi_{1/3}Fe_{2/9}Co_{1/9}Mn_{1/3}O_2$	854.9 (1.9)	711.0 (4.0)	780.4(1.6)	842.4 (3.4)
$LiNi_{1/3}Fe_{1/3}Mn_{1/3}O_2$	854.8 (1.9)	710.8 (3.8)	-	842.3 (3.3)

The binding energies for elemental Fe are 719-720eV for $2p_{1/2}$ and 706-708eV for $2p_{3/2}$ [5]

4.2.5 ^{57}Fe Mössbauer Spectroscopy

Mössbauer spectroscopy can give precise information about the chemical, structural, magnetic and time-dependent properties of a material. Nuclei in atoms undergo a variety of energy level transitions, often associated with the emission or absorption of a gamma ray. These energy levels are influenced by their surrounding environment, both electronic and magnetic, which can change or split these energy levels. Isomer Shift, Quadrupole Splitting and Magnetic Splitting are the primary characteristics of Mössbauer spectra.

Isomer shift arises due to the non-zero volume of the nucleus and the electron charge density due to s-electrons within it. This leads to a monopole (Coulomb) interaction, altering the nuclear energy levels. The isomer shift is for determining valence states, ligand bonding states and electron shielding.

Quadrupole splitting describes the electrical interactions. In the presence of an asymmetrical electric field (present due to an asymmetric charge distribution or ligand arrangement), the nuclear energy levels will be split. In the case of an isotope with an excited state I=3/2 (I = 1/2 is the ground state), such as ^{57}Fe, the excited state is split into $m_I = \pm 1/2$ and $m_I = \pm 3/2$, giving a doublet spectrum.

Magnetic splitting arises by the internal field experienced by the nucleus. In the presence of a magnetic field the nuclear spin moment experiences a dipolar interaction with the magnetic field, that is, Zeeman splitting. For ^{57}Fe, six possible transitions between the excited state and ground state can occur.

The two samples: $LiNi_{1/3}Fe_{1/9}Co_{2/9}Mn_{1/3}O_2$ and $LiNi_{1/3}Fe_{1/9}Co_{2/9}Mn_{1/3}O_2$ (800°C) have been studied using a HALDER type spectrometer with a constant acceleration and a ^{57}Co source (in a Rhodium matrix). The powders were grounded and the samples contained about 10 mg of Fe per cm^2. The spectra were recorded at 293 K and 4.2 K by using a cryostat with liquid helium. The refinement of these spectra has been performed following the Hesse and Rubartsch method [6].

Figure 4-7 is the Fe Mossbauer spectra obtained at room temperature. A calculation taking into account a distribution of doublets was shown to give the good reliability factors and minimisation of the difference $A_{obs.}$-$A_{calc.}$, and the refinement parameters are shown in Table 4-IV.

The position of the line is associated to the isomer shift δ, α-Fe being the standard at room temperature. The isomer shift reflects the electronic density present at the nucleus. For Fe, it increases with the ionicity of the Fe-O bonds. δ values were obtained by a first refinement of the spectra using a distribution of Lorentzian lines.

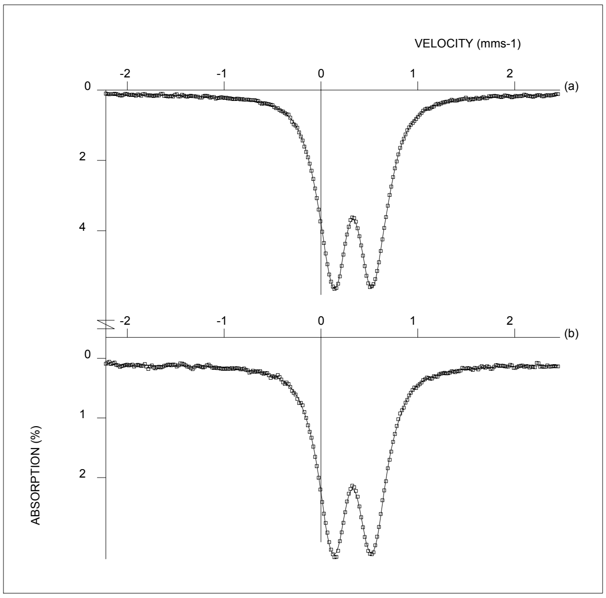

Figure 4-7 Experimental and calculated Mössbauer spectra obtained at 293 K for $LiNi_{1/3}Fe_zCo_{1/3-z}Mn_{1/3}O_2$ with (a) z = 1/6 and (b) z = 1/9. (The dots are experimental values and the lines are calculated values)

Table 4-IV Mössbauer parameters obtained at 293 K

z = 1/6	**DIS**	**δ (mm.s^{-1})**	**Δ (mm.s^{-1})***	**Γ (mm.s^{-1})**	**%***	**site**
	1	0.39	0.45	0.25	49.8	Fe^{3+}
	2	0.29	0.44	0.25	50.2	Fe^{3+}
z = 1/9	**DIS**	**δ (mm.s^{-1})**	**Δ (mm.s^{-1})***	**Γ (mm.s^{-1})**	**%***	**site**
	1	0.39	0.44	0.25	47.4	Fe^{3+}
	2	0.29	0.43	0.25	52.6	Fe^{3+}

(*) refined parameters
Γ: line width at half height, fixed at 0.25 mm/s, value expected for ^{57}Fe at room temperature.

Two distinct octahedral sites were identified for trivalent iron at room temperature. The proportion between these two sites is approximately 50/50 in both cases. These two distributions can be distinguished by the value of their isomer shifts (DIS1: δ = 0.39 mm.s^{-1} and DIS2: δ = 0.29 mm.s^{-1}). These two sites are probably associated to two different cationic distributions around the iron ions.

The distribution **DIS1** corresponds to a site less covalent than the one associated to the distribution **DIS2**, *i.e.* the average Fe-O distances in site 1 are longer than the ones in site 2. Due to the presence of different cations (Ni^{II}, Co^{III}, Fe^{III} and Mn^{IV}) in the materials with different ionic radii and valence states, we would expect difference in Fe local environments. Another possibility is local $LiFeO_2$-formation in the compounds. The $LiFeO_2$ ground-state structure is not layered, but a structure with symmetry $I4_1/amd$ as shown in Figure 4-8. Different from the layered O3 structure, the $LiFeO_2$ structure forms a tetragonal supercell of the rocksalt structure. Notice that DIS2 could not be associated to Fe present in a tetrahedral site since the literature value for the isomer shift for Fe in tetrahedral site is close to 0.21mm/s.

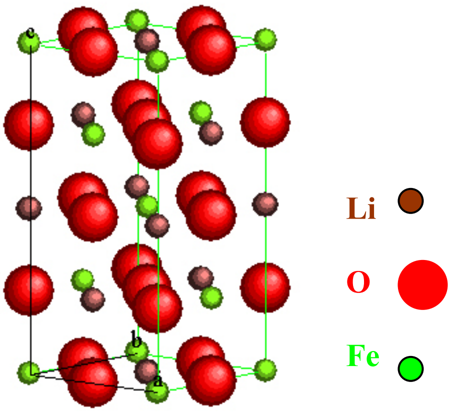

Figure 4-8 Crystal structure of ground state $LiFeO_2$, with space group $I4_1/amd$

In order to further understand the compounds by examining their magnetic behavior, Mössbauer data was also collected at 4.2 K, shown in Figure 4-9 and Table 4-V. The resolution of these spectra is not good despite a long counting time. The main reason is the presence of two types of contributions: one (DIS3) is characterised by a superparamagnetism behaviour that is observed in materials characterised by domains very small in size, with no interactions between them; the others (DIS1 and

DIS2) are magnetically ordered at 4.2K. This result shows again that these materials are not homogeneous, consistent with the results found by room temperature

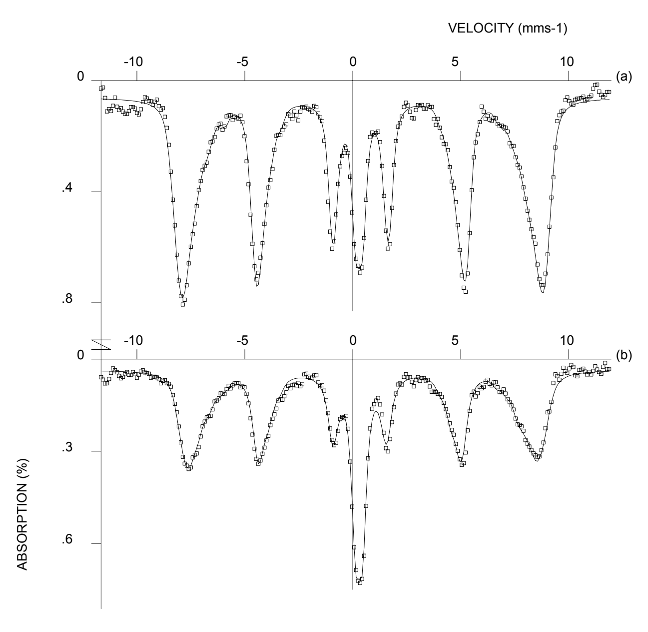

Figure 4-9 Experimental and calculated Mössbauer spectra obtained at 4.2 K for $LiNi_{1/3}Fe_xCo_{1/3-x}Mn_{1/3}O_2$ with (a) x = 1/6 and (b) x = 1/9.

The existence of these two types of contributions indicates that the ordering temperature is perhaps close to 4.2K. The study at 4.2K is in good agreement with the results obtained at T = 293 K with the existence of two octahedral sites for the trivalent iron ions. Their Mössbauer parameters remain close but with rather different values for isomer shift δ shows probably that a tendency to segregation exists in these materials with two cationic environments for the Fe ions.

Table 4-V Mössbauer parameters obtained at 4.2 K

x = 1/6	DIS	δ (mm.s^{-1})	Γ (mm.s^{-1})	ε (mm.s^{-1})	Δ (mm.s^{-1})*	H (T)	%*	site
	1	0.51	0.35	0.05	-	50.2	42	Fe^{3+}
	2	0.34	0.35	0.001	-	50.0	47	Fe^{3+}
	3	0.34	0.35	-	0.31	-	11	Fe^{3+}
x = 1/9	DIS	δ (mm.s^{-1})	Γ (mm.s^{-1})	ε (mm.s^{-1})	Δ (mm.s^{-1})*	H (T)	%*	site
	1	0.51	0.50	0.15	-	48.8	34	Fe^{3+}
	2	0.34	0.50	-0.01		48.4	43	Fe^{3+}
	3	0.34	0.40	-	0.31	-	23	Fe^{3+}

(*) refined parameters

H : hyperfine field, internal magnetic field

ε : quantifies the perturbations brought by the electrostatic interactions to the magnetic interactions.

4.3. Electrochemical Properties

$LiNi_{1/3}Fe_zCo_{1/3-z}Mn_{1/3}O_2$ electrodes were fabricated by mixing 85:1.5:3.5:10 (w/w) ratio of active material, SS carbon black, KS-6 carbon and polyvinylidene fluoride (PVDF), respectively, in N-methyl-pyrrolidinone (NMP). The resulting slurry was cast onto an aluminum current collector and dried under vacuum oven overnight. The electrode foils were cut into disks of 8mm diameter and cold pressed. Electrochemical measurements were made using coin-type cells comprising a Li metal counter electrode with a 1M solution of LiPF6 in EC/DMC (1:1 v/v, Merck LP30) as the electrolyte. The cells were assembled in an argon filled glove box where the moisture level is less than 1ppm. The cells were charge-discharged cycled using a Maccor battery tester at C/10 (or C/20) over a potential range between 3.0V to 4.5V/4.8V.

Electrodes of $LiNi_{1/3}Fe_{1/6}Co_{1/6}Mn_{1/3}O_2$ synthesized at 750 ºC, 800 ºC and 850 ºC were cycled at a rate of C/10 (based on 281mAh/g total capacity) between 3.0V and 4.5V. The first charge and discharge curves for each sample are shown in Figure 4-

10. Qualitatively, the potential curves are very similar, exhibiting a relatively flat potential on charging in the range of 3.7 to 3.9 V, and then a relatively steeply sloping curve on discharge. The compound synthesized at 750 ºC shows smaller polarization which could be related to its smaller grain size. There is a significant amount of irreversible capacity after the first charge for all three samples. As the synthesis temperature increases from 750 ºC, 800 ºC to 850 ºC, the first charge capacity decreases from 220mAh/g, 200mAh/g to 187mAh/g; the first discharge capacity changes from 150mAh/g, 139mAh/g to 134mAh/g.

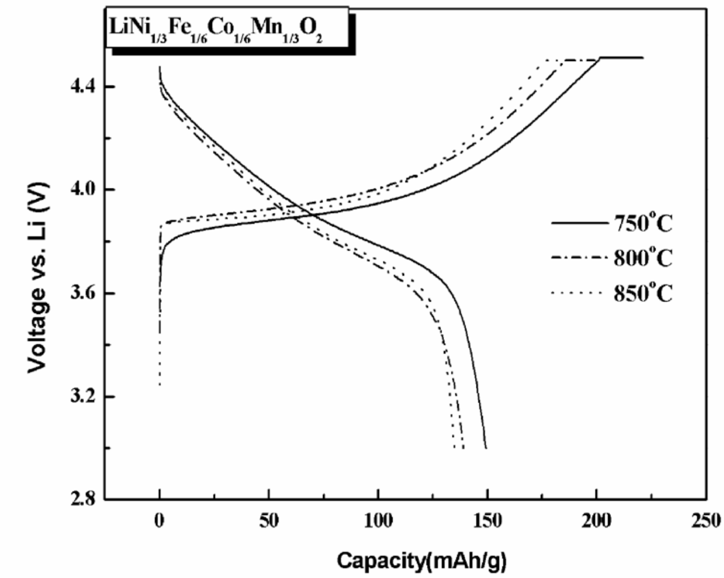

Figure 4-10 Variation of the cell potential on first charging then discharging the cells at C/10 for $LiNi_{1/3}Fe_{1/6}Co_{1/6}Mn_{1/3}O_2$ prepared at 750ºC, 800ºC and 850ºC

The delithiation potential of the material synthesized at 750°C is plotted together with the calculated potential curve in Figure 3-5. The potential difference between the calculated and experimental data is suggested to be 0.7~0.8V. [7] The correction of 0.9V in this case was added to the calculated potential to display a result that can be compared directly with the experimental values, as shown in Figure 4-11. The experimental charge-discharge curve matches the calculated one well in the range of $1/3 \leq x \leq 1$. The practical specific capacity of this material will likely be more than 250mAh/g if the cell is charged to approximately 4.8V, according to the computational prediction.

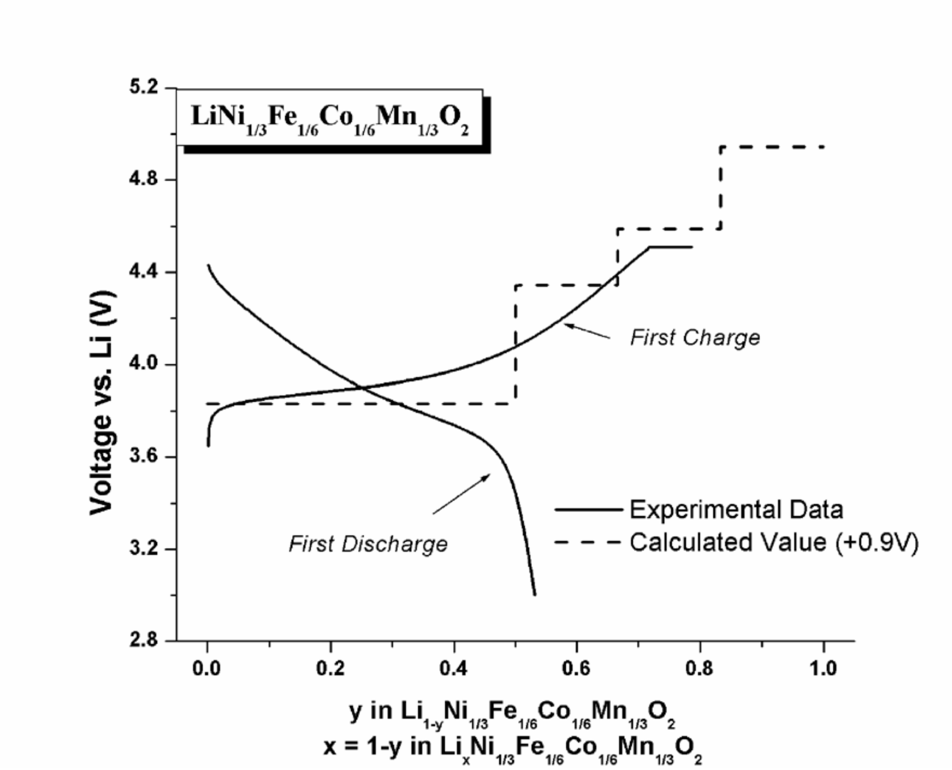

Figure 4-11 Comparison of experimental potential curve (sample synthesized at 750°C) with the predicted potential curve by first principles calculation.

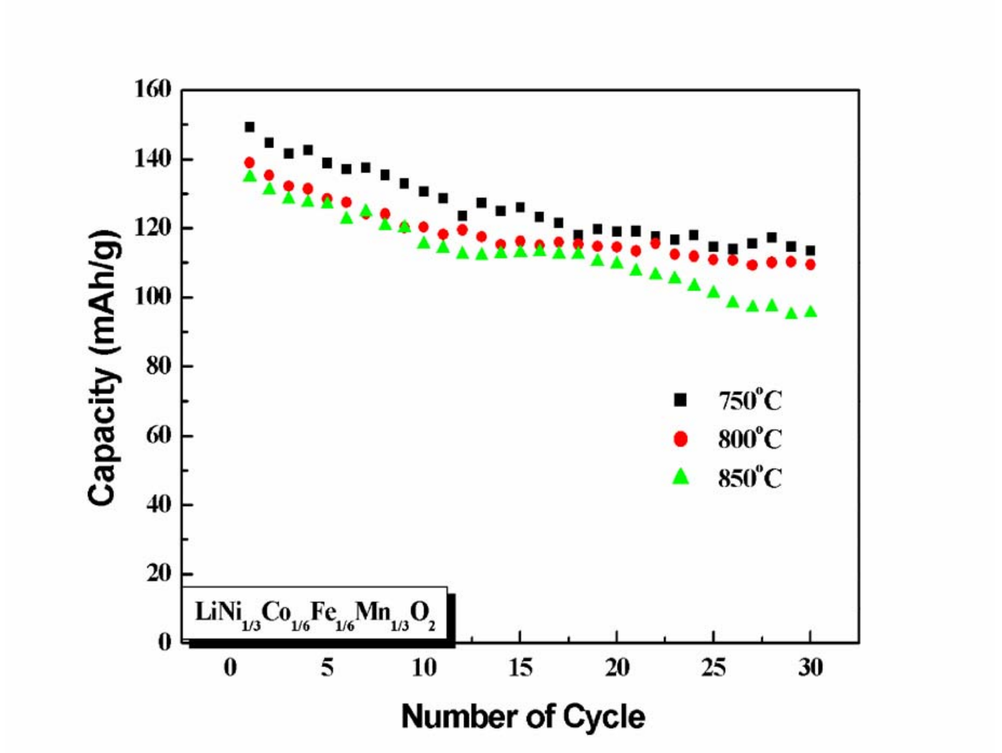

Figure 4-12 Charge and discharge capacity *vs.* cycle number curves of the$LiNi_{1/3}Fe_{1/6}Co_{1/6}Mn_{1/3}O_2$ materials synthesized at 750, 800, and 850°C for 16 h.

The capacity retention up to 30 cycles is reasonably good for all samples, as demonstrated in Figure 4-12. The possible reasons for the large first-cycle irreversible capacity will be discussed later. A preliminary study shows that the first cycle reversible capacity can be increased by 20% with surface treatment of the synthesized powders. This implies the surface degradation of the as-synthesized material might have a signification impact on the reversible capacity, similar to that has been demonstrated in $LiCoO_2$ system.[8]

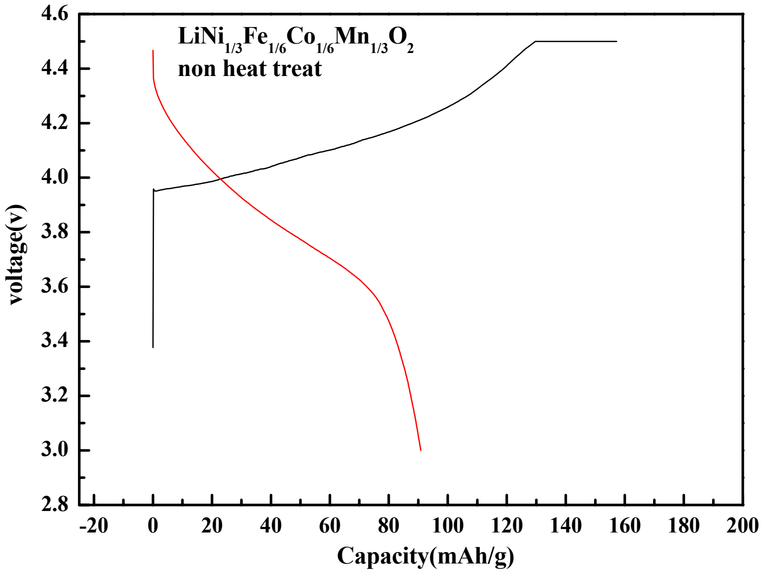

(a)

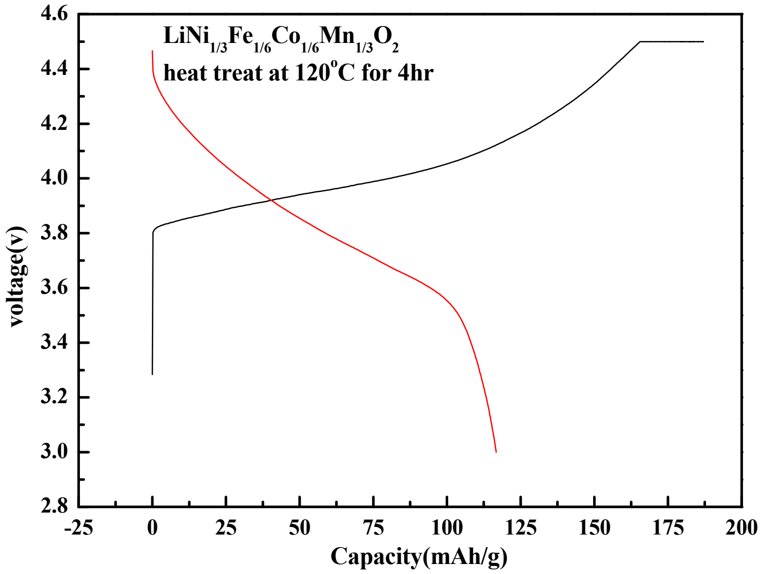

(b)

Figure 4-13. Comparison of first cycle potential curve of $LiNi_{1/3}Fe_{1/6}Co_{1/6}Mn_{1/3}O_2$ with (a) and without (b) heat treatment of the electrode in the glove box

Electrochemical cycling of $LiNi_{1/3}Fe_zCo_{1/3-z}Mn_{1/3}O_2$ compounds for and z = 1/6 and z = 2/9 synthesized at 800°C were carried out at C/10 between 3 - 4.8V. Figure 4-14 shows the comparison of first charge-discharge potential curves for the two compounds. Though more Fe doping (z = 2/9) gives lower potential, thus higher charge capacity, the percentage of irreversible capacity is much higher than that of z

= 1/6. In addition, the sample with more Fe doping cycled poorly. This is suspected that Fe migration to the tetrahedral sites could be the reason for reduced discharge capacity, which will be further discussed in the next section.

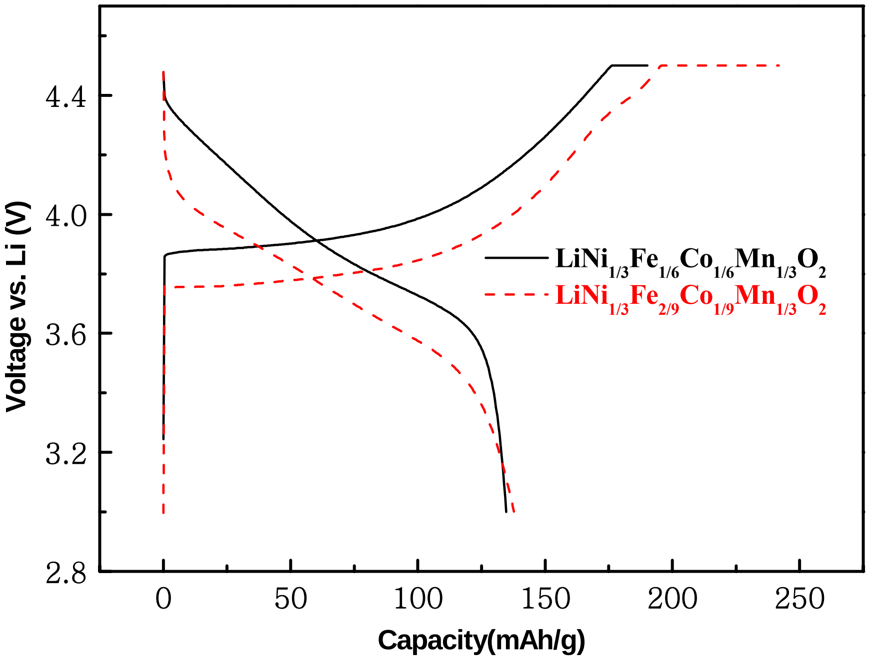

Figure 4-14 First charge discharge curve comparison of $LiNi_{1/3}Fe_{1/6}Co_{1/6}Mn_{1/3}O_2$ and $LiNi_{1/3}Fe_{2/9}Co_{1/9}Mn_{1/3}O_2$

In summary, among the samples synthesized, $LiNi_{1/3}Fe_{1/6}Co_{1/6}Mn_{1/3}O_2$ sintered at 750°C has shown the good electrochemical properties in terms of reversible capacity and capacity retention. Excessive Fe substitution ($z > 2/9$) leads to significant decrease both in initial capacity and capacity retention. The characterization of partially charged materials focuses on $LiNi_{1/3}Fe_{1/6}Co_{1/6}Mn_{1/3}O_2$, which is compared with the first principles computation performed on the compound with the same composition.

4.4 Characterization of Partially Charged Materials

4.4.1 XPS and Change in Electronic Structures

X-ray photoelectron spectroscopy (XPS) was applied to corroborate the electronic behavior predicted computationally. Ex-situ X-ray photoelectron spectroscopic study was carried out to study the valence shifts of Ni, Co, Fe and Mn in $LiNi_{1/3}Fe_{1/6}Co_{1/6}Mn_{1/3}O_2$ and in partially charged $Li_xNi_{1/3}Co_{1/6}Fe_{1/6}Mn_{1/3}O_2$ ($x \approx 1/2$). The electrodes were charged to 4.4V. The binding energies of those cations in the as-prepared and partially charged compounds are tabulated in Table VI. Indicated by the binding energy shift of the *2p* electrons for the transition metal cations from their elemental values [5], XPS confirms that the valence states of Ni, Fe, Co, and Mn in the as-synthesized $LiNi_{1/3}Fe_{1/6}Co_{1/6}Mn_{1/3}O_2$ are 2+, 3+, 3+ and 4+ respectively, as mentioned before. Furthermore, as lithium is removed from the compound, both $Ni^{2+}/Ni^{3+}/Ni^{4+}$ and Fe^{3+}/Fe^{4+} redox couples are activated, revealed by an obvious shift in the binding energies of Ni *2p* and Fe *2p* edges. No obvious shifts in Co and Mn edges were observed. The results are in good agreement with the calculated change of valence states during delithiation.

It is expected based on the XPS study that for the delithiated cathode materials $Li_xNi_{1/3}Fe_zCo_{1/3-z}Mn_{1/3}O_2$ cycled in the potential window of 3.0 to 4.5V, Ni and Fe redox couples are activated, while Co and Mn remain unchanged in their oxidation states and chemical environment.

Table 4-VI XPS binding energy for as-prepared and partially-charged materials

	Ni	Fe	Co	Mn
	$2p_{3/2}$/eV	$2p_{3/2}$/eV	$2p_{3/2}$/eV	$2p_{3/2}$/eV
$\mathbf{LiNi_{1/3}Fe_{1/6}Co_{1/6}Mn_{1/3}O_2}$	854.7	710.9	780.4	842.3
	(1.7)	(3.9)	(1.4)	(3.3)
$\mathbf{Li_xNi_{1/3}Fe_{1/6}Co_{1/6}Mn_{1/3}O_2}$	855.5	711.8	780.4	842.1
$x \approx 1/2$	(2.5)	(4.8)	(1.4)	(3.1)

* Number in the parentheses - shift in binding energy

4.4.2 Ex-situ XRD and Lattice Parameter

Ex-situ X-ray diffraction was carried out to characterize partially charged $LiNi_{1/3}Fe_{1/6}Co_{1/6}Mn_{1/3}O_2$. The first cell was charged to 4.5V and in open circuit relaxation for 12 hours (OCV = 4.1V) and dissembled in an argon-filled glove box. The second cell was charged to 4.5V and discharged to 3.0V, followed by open circuit relaxation for 12 hours (OCV = 3.8 V). The XRD spectra were depicted in Figure 4-15 a) and b) for the two samples respectively. No major second phase was observed in both samples.

As shown in Table 4-VII, the calculated lattice parameters predicted correctly the trend of change in a and c lattice parameters with various lithium concentrations. The first principles calculated a lattice parameter decreases in the range of $1/3 \leq x \leq 1$ by approximately 2.2%. The calculated lattice parameter c increases by about 4.2% in the range of $1/3 \leq x \leq 1$. However, in experiment the increase is much more subtle. It is commonly believed that the oxygen-oxygen columbic repulsion force and the electrostatic attraction of Li^+ and O^{2-} contribute to the change in *c* upon lithium removal. As x decreases (delithiation), there are less Li^+ ions attracting O^{2-} across the layers, resulting in increase of *c*. At the end of delithiation, when there is possibly charge transfer occur on oxygen, making oxygen ion less negative and O-O repulsion becomes weaker, which leads to decrease in *c*-axis. To explain why experimentally the change in *c* axis is less obvious than calculated change, one possibility is that due to the presence of transition metal ion in the lithium layer, the highly positively charged transition metal ions moderate the change in electrostatics caused by Li removal. A recent study by Van der Ven and Ceder on $LiNi_{1/2}Mn_{1/2}O_2$ demonstrated such possibility in more details[9].

Table 4-VII, Comparison of experimental and calculated lattice parameters at various lithium concentrations

	Voltage (V)	a_{exp} (Å)	c_{exp} (Å)	a_{cal} (Å)	c_{cal} (Å)
x=1	3.0V	2.8859	14.3222	2.9138	14.3690
x=0.36	4.1V	2.8448	14.3466	2.8490 (x=1/3)	14.9709
x=0.77	3.8V	2.8691	14.3298	2.8922 (x=5/6)	14.4359

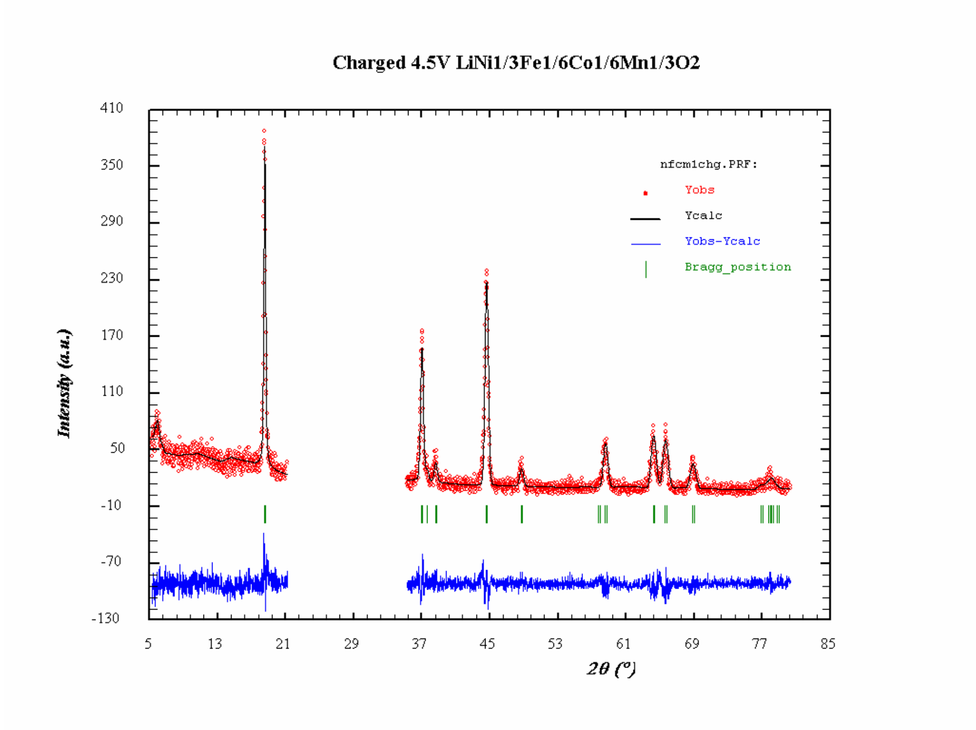

(a)

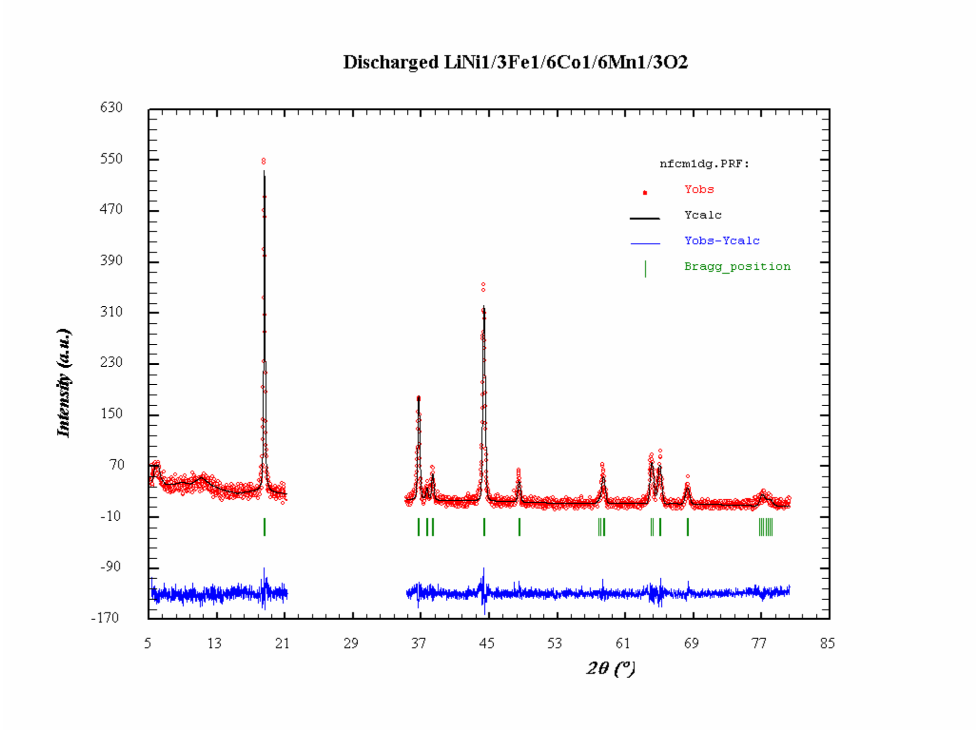

(b)

Figure 4-15 Powder XRD spectra of charged $LiNi_{1/3}Fe_{1/6}Co_{1/6}Mn_{1/3}O_2$ (a) x = 0.36 and (b) x = 0.77

4.4.3 XAS and TM-O Bond Lengths

X-ray absorption spectroscopy (XAS) experiments were carried out in transmission mode at beam line BL-17C at the National Synchrotron Radiation Research Center (NSRRC) in Hsinchu, Taiwan. The storage ring was operated with electron energy of 1.5 GeV and a current between 100 and 200mA. A Si(111) double-crystal monochromator was employed for energy selection. High-order harmonic contamination was rejected by mirrors. The intensities of the incident and transmitted beams were measured by gas ionization chambers. Energy scans of the sample were performed at Ni, Co, Fe and Mn K-edges.

X-ray Absorption Spectroscopy is the modulation of the x-ray absorption coefficient $\mu(E)$ at energies near and above an x-ray absorption edge. It utilizes high intensity, collimated x-ray sources at synchrotron radiation facilities. ($0.03\ \text{Å} \leq \lambda \leq 12\ \text{Å}$ or energy $1\text{keV} \leq E \leq 500\text{keV}$)

The amplitude of the back-scattered photo-electron at the absorbing atom will oscillate with energy, causing oscillation in $\mu(E)$. Such oscillations are an interference effect due to the presence of the neighboring atoms. As the photo-electron

1. leaves the absorbing atom
2. scatters from the neighbor atoms
3. returns to the absorbing atom

a simple model (Figure 4-16) can be built with spherical wave for the photo-electron:

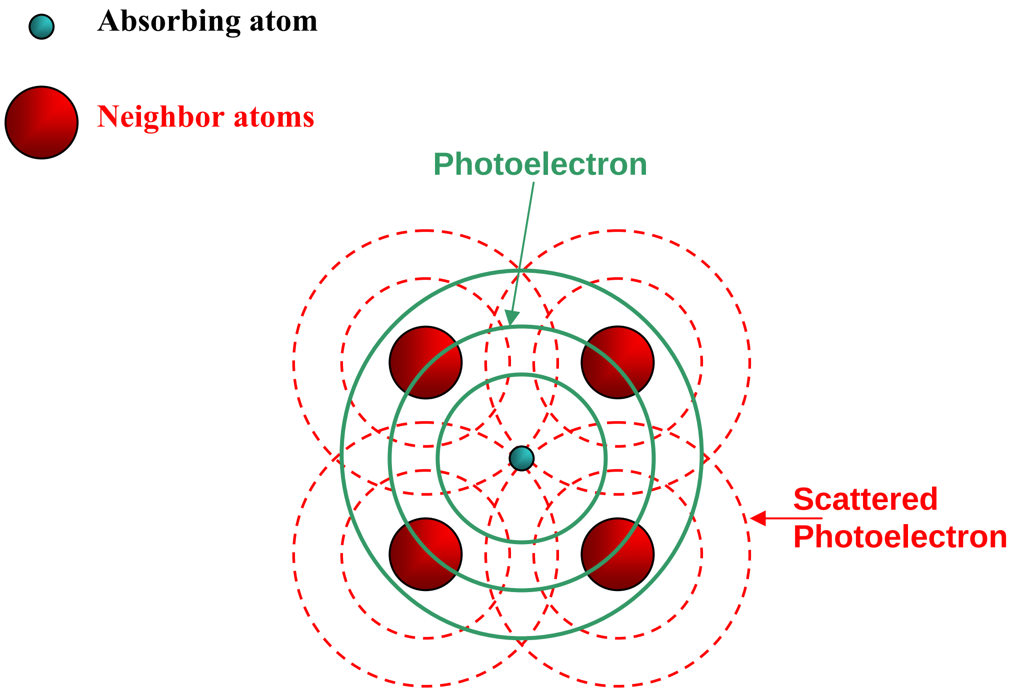

Figure 4-16 Schematic representation of back-scattered photo-electron at the absorbing atom

It is divided into two regimes:

X-ray Absorption Near-Edge Spectroscopy (**XANES)**, this technique is able to determine

- Electronic structures
- Symmetry
- Chemical / Oxidation state

Extended X-ray Absorption Fine-Structure (**EXAFS**), which contains information about an element’s local coordination and chemical state.

- Coordination number
- Radius
- Debye-Waller factor

The photo electron mean free path is typically 5 – 10 Å (< 25 Å) for much of the EXAFS range. EXAFS is a local atomic probe.

4.4.3.1 XANES

X-ray absorption near-edge structure (XANES) provides information about the valence state of the absorbing atom. The XANES results obtained for the $Li_xNi_{1/3}Fe_{1/6}Co_{1/6}Mn_{1/3}O_2$ material are shown in this work. Parts (a), (b), (c) and (d) of Figure 4-17 show the Ni, Co, Fe and Mn K-edges XANES spectra of this material, respectively. As observed easily in Figure 4-17a) and b), the Ni edges of $Li_xNi_{1/3}Fe_{1/6}Co_{1/6}Mn_{1/3}O_2$ at x = 1.0, 0.985, 0.771, 0.494 and 0.243 shifts to higher energy upon charging. This indicates that the valence state of Ni in $Ni_{1/3}Fe_{1/6}Co_{1/6}Mn_{1/3}O_2$ changes from 2+ to 3+ or 4+. A similar phenomenon is also observed in the Fe K-edge XANES spectra. No significant energy shift can be observed in the Co and Mn XANES spectra as shown in Figure 4-17 (c) and (d), which is consistent with all previous experimental and computation data. Mn ions do not appear to actively participate in the charge compensation process, and Co ions are not activated completely during the charging process at cutoff voltage 4.5V.

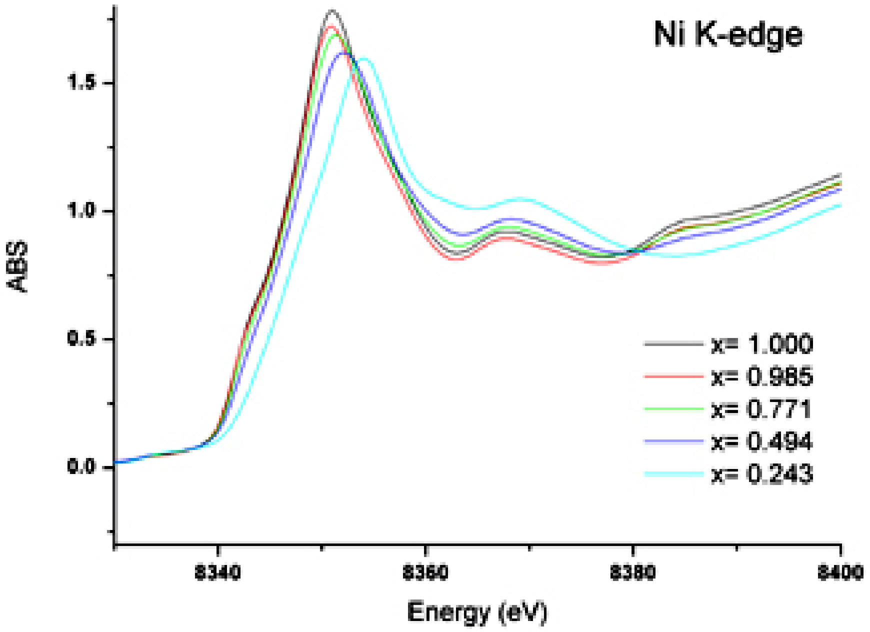
Ni K-edge
ABS
1.5
1.0
0.5
0.0
8340
8360
8380
8400
Energy (eV)
x= 1.000
x= 0.985
x= 0.771
x= 0.494
x= 0.243

(a)

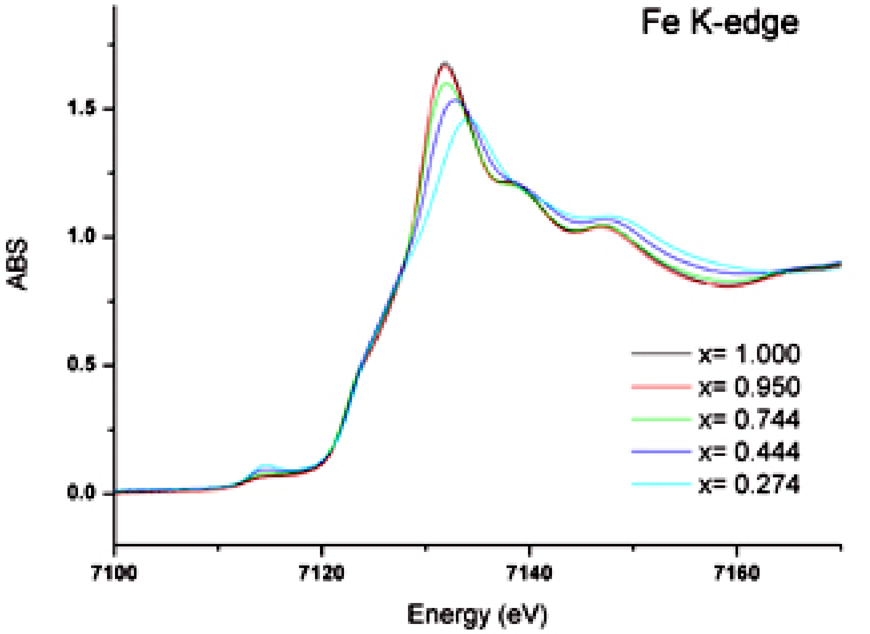
Fe K-edge
ABS
1.5
1.0
0.5
0.0
7100
7120
7140
7160
Energy (eV)
x= 1.000
x= 0.950
x= 0.744
x= 0.444
x= 0.274

(b)

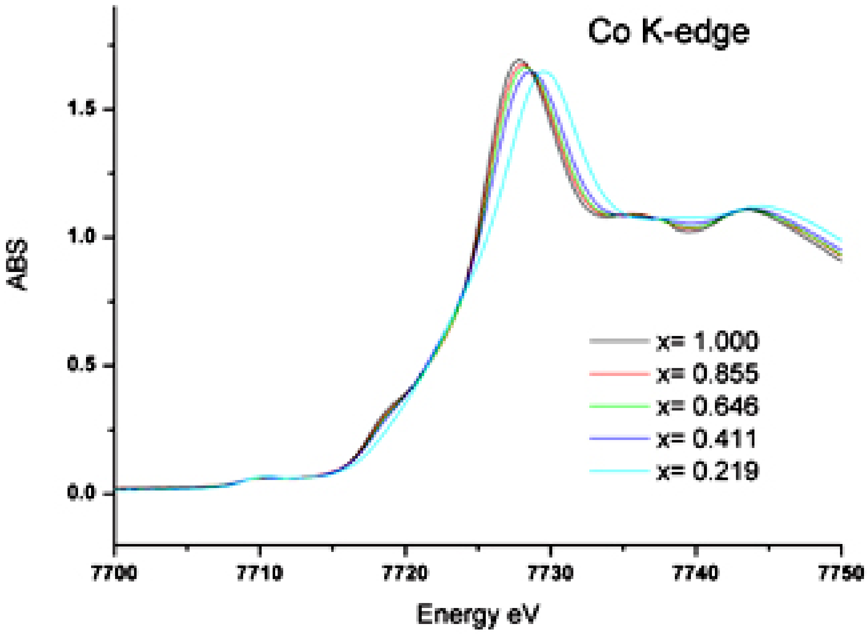

(c)

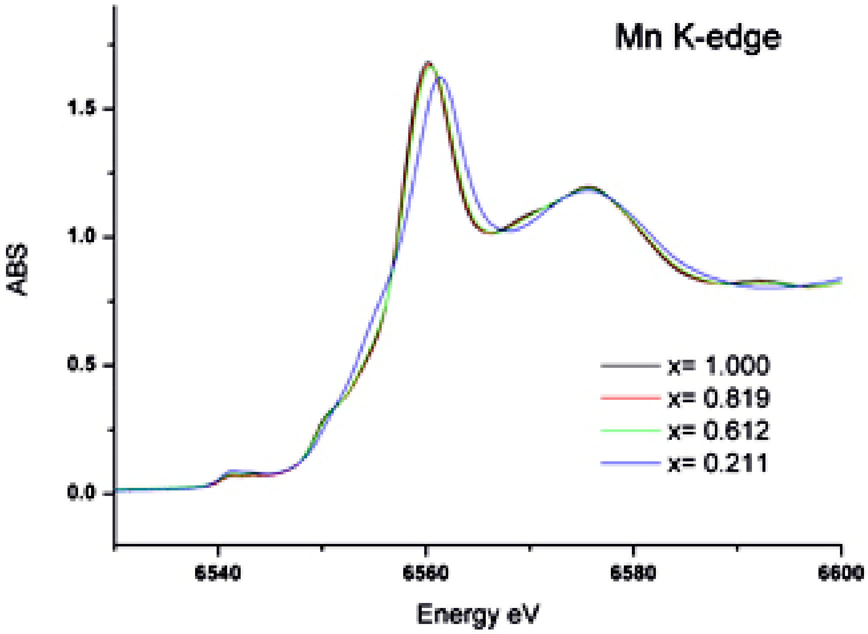

(d)

Figure 4-17 XANES spectra of a) Ni edge b) Fe edge c) Co edge and d) Mn edge of $LiNi_{1/3}Fe_{1/6}Co_{1/6}Mn_{1/3}O_2$

4.4.3.2 EXAFS

Figure 4-18 a)-d) shows the Fourier transform magnitudes of the Ni, Fe, Co and Mn K-edge EXAFS spectra during charge. The first coordination shell consists of oxygen, while the peak feature of the second coordination shell is dominated by transition metal cations. The most significant change during the charge is observed in the first coordination shell around Ni atoms. The dramatic changes of the first coordination peaks positions indicate that the charge compensation does mainly occur at the Ni sites and results in a large decrease in the average Ni-O bond length. There is also a considerable amount of shift of the first coordination peaks for Fe atoms, indicating that the charge compensation also happens at the Fe sites. Another obvious change is that the relative intensity ratio of the first coordination peak to the second coordination peak reverses for Fe atoms upon lithium removal. As this indicates a local environment change around the Fe sites, speculation of Fe migration to the Li sites in the Li layer rises. When Fe migrates to the Li layer, Fe will be surrounded by Li atom, which has a much weaker scattering power than the transition metal atoms; thus the peak intensity of the second coordination shell is reduced. This is highly possible since Fe^{3+} has 3d5 electronic structure, therefore no ligand field stabilization energy exists. In addition, a preliminary study on the susceptibility of Fe migration by first principles computations show that the migration barrier is small enough, comparable to that of Mn^{3+}. In consistency with the XANES spectra, no significant changes are observed in the first and second coordination shells around Co and Mn atoms, as illustrated in Figure 4-18 c) and d). The trend in TM-O bond length changes during charging agrees very well with the first principles computed ones, as shown in Figure 8 in the previous chapter.

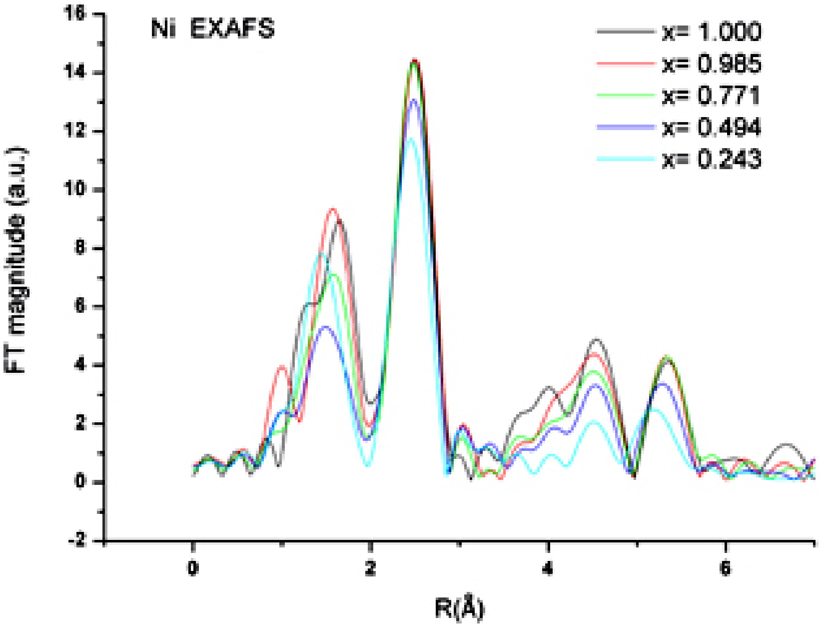
Ni EXAFS
x= 1.000
x= 0.985
x= 0.771
x= 0.494
x= 0.243
FT magnitude (a.u.)
R(Å)
16
14
12
10
8
6
4
2
0
-2
0
2
4
6

(a)

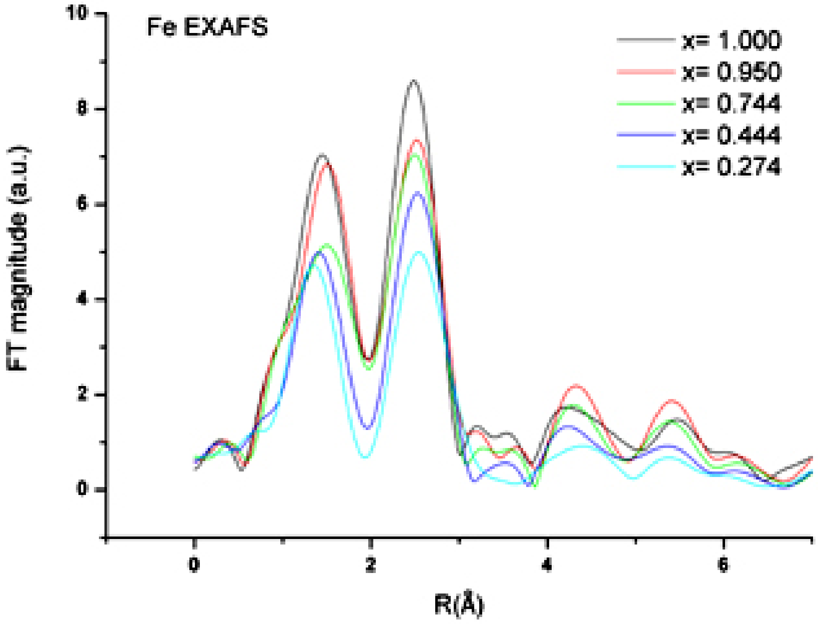
Fe EXAFS
x= 1.000
x= 0.950
x= 0.744
x= 0.444
x= 0.274
FT magnitude (a.u.)
R(Å)
10
8
6
4
2
0
0
2
4
6

(b)

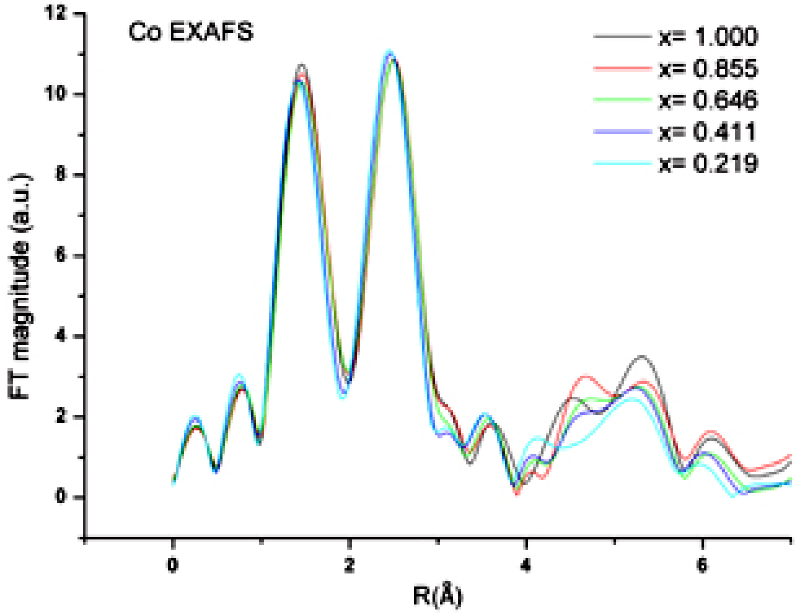

(c)

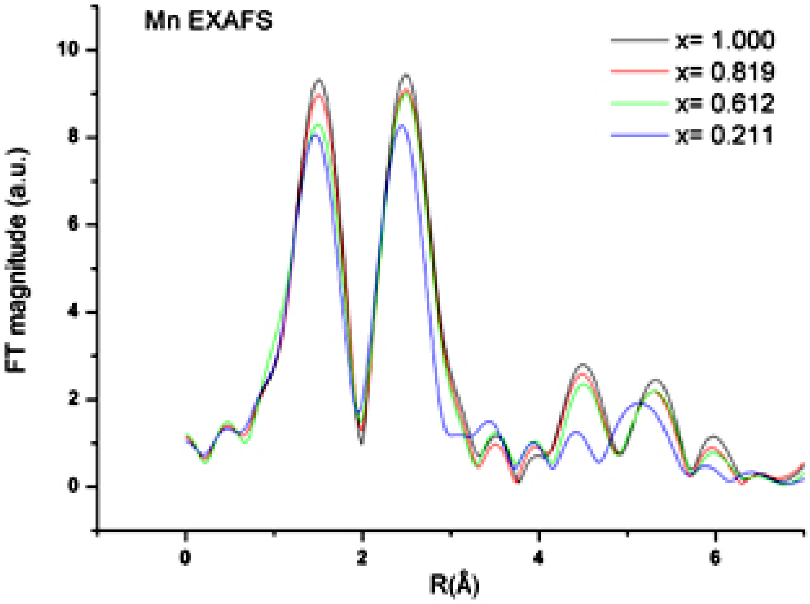

(d)

Figure 4-18 EXAFS spectra of a) Ni edge b) Fe edge c) Co edge and d) Mn edge of $LiNi_{1/3}Fe_{1/6}Co_{1/6}Mn_{1/3}O_2$

4.5 First Principles Analysis of Fe Stability in Layered Oxides

To better understand the in-situ EXAFS data, an evaluation of the Fe stability in the layered structure was carried out with first principles computation. We adopted the mechanism proposed by Reed and Ceder [10], and calculated the energy barrier for the migration of Fe ions from octahedral site to tetrahedral site when the material is partially delithiated. The lowest energy path starts with a hop from a transition metal layer octahedron to an adjacent lithium plane tetrahedron through the triangular face shared by the two sites. To get a qualitative understanding, we calculated three states 1) layered structure (free of defect) 2) Fe defect in the shared face between transition metal layer octahedron and Li layer tetrahedron (transition state) and 3) Fe defect in Li layer tetrahedron

Two virtual compositions $Li_{1/2}Zr_{1/2}Fe_{1/2}O_2$ and Li_0FeO_2 were used for investigating the migration barrier of Fe^{3+} and Fe^{4+} respectively. As it can be seen clearly in Figure 4-19, in $Li_{1/2}Zr_{1/2}Fe_{1/2}O_2$ when a Li layer tetrahedron is surrounded by Li vacancies, the activation barrier for a neighboring Fe to move into that tetrahedron through the triangular oxygen face is 0.5eV. The energy of the structure with one Fe^{III} tetrahedron defect lies beneath that of un-defect structure, which indicates the Fe^{3+} prefers the tetrahedron coordination. In Li_0FeO_2, the energy of the structure with one Fe^{IV} tetrahedron defect is 0.37eV higher than that of un-defect structure. Furthermore, the activation barrier for a Fe^{IV} to move into the tetrahedron through the triangular oxygen face is calculated to be as high as 4.9eV. This indicates that in the fully delithiated structure, Fe^{4+} refers the octahedron coordination. In summary, octahedral Fe^{3+} is susceptible to migration to tetrahedral site when Li is partially removed from the layered structure, according to the first principles computation.

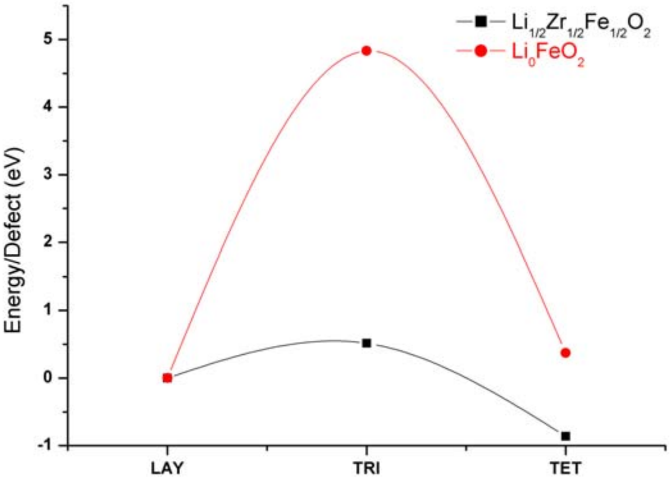

Figure 4-19 Energies of LAY: layered undefected structure; TRI: Fe defect in shared face between transition metal layer octahedron and Li layer tetrahedron; TET: Fe defect in Li layer tetrahedron

The speculation of Fe migration to tetrahedron in the Li layer from the in-situ EXAFS data requires further in-depth investigation.

4.6 Conclusions

Motivated by a series of first principles calculations on $LiNi_{1/3}TM1_{1/3}TM2_{1/3}O_2$, $LiNi_{1/3}Fe_zCo_{1/3-z}Mn_{1/3}O_2$ ($0 \leq z \leq 1/3$) cathode materials were synthesized by the sol-gel method. Excessive Fe substitution ($z > 2/9$) leads to evolution of non-layered impurity phase, which can be clearly seen by powder XRD and SEM experiments. Preliminary X-ray Photoelectron Spectroscopy XPS (Al source) results for $LiNi_{1/3}Fe_zCo_{1/3-z}Mn_{1/3}O_2$ cathode materials revealed that the oxidation state of Ni, Mn, Fe are 2+, 4+ and 3+, respectively, which is consistent with the first-principle computation results. We predicted and confirmed that Fe substitution would lead to a lower potential at the end of charge. The $LiNi_{1/3}Fe_{1/6}Co_{1/6}Mn_{1/3}O_2$ compound synthesized at 750°C shows reversible capacity of 150mAh/g with reasonably good capacity retention. This material may be considered as potential cathode material in lithium ion battery. First principles electronic structure computations indicate that Ni and Fe are simultaneously oxidized in this material. Computations further indicate that Co will only be oxidized at the very end of charge. Both XPS and XAS study on delithiated $Li_xNi_{1/3}Fe_{1/6}Co_{1/6}Mn_{1/3}O_2$ reveals that in the potential window of 3.0 to 4.5V, Ni and Fe redox couples are activated, while Co and Mn remain unchanged in their oxidation states and chemical environment.

In this work, we have demonstrated that an integrated approach of computation and experiment has produced a new electrode material with very few iteration steps in the material design cycle. We believe that such direct integration of ab-initio methods with experimental research holds promise for significantly shortening the development cycle of materials.

References:

1. C. Delmas, et al., *An overview of the Li(Ni,M)O_2 systems : syntheses, structures and properties.* Electrochimica Acta, 1999. **45**: p. 243-253.
2. C. Delmas, et al., *Effect of iron on the electrochemical behaviour of lithium nickelate : from $LiNiO_2$ to 2D-$LiFeO_2$.* Solid State Ionics, 2000. **135**: p. 71.
3. E.J. Wu, P.D. Tepesch, and G. Ceder, *Size and charge effects on the structural stability of $LiMO_2$ (M = transition metal) compounds.* Philosophical Magazine B, 1998. **77**(4): p. 1039-1047.
4. B.J. Hwang, et al., *A combined computational/experimental study on $LiNi_{1/3}Co_{1/3}Mn_{1/3}O_2$.* Chemistry of Materials, 2003. **15**(19): p. 3676-3682.
5. www.srdata.nist.gov/xps/.
6. J. Hesse and A. Rubartsch, J. Phys. E. Sci. Instrum., 1974. **7**: p. 526.
7. M.K. Aydinol, et al., *Ab initio study of lithium intercalation in metal oxides and metal dichalcogenides.* Physical Review B, 1997. **56**(3): p. 1354-1365.
8. Z.H. Chen and J.R. Dahn, *Methods to obtain excellent capacity retention in $LiCoO_2$ cycled to 4.5 V.* Electrochimica Acta, 2004. **49**(7): p. 1079-1090.
9. A. Van der Ven and G. Ceder, *Ordering in $Li_x(Ni_{0.5}Mn_{0.5})O_2$ and its relation to charge capacity and electrochemical behavior in rechargeable lithium batteries.* Electrochemistry Communications, 2004. **6**: p. 1045-1050.
10. J. Reed, G. Ceder, and A. Van Der Ven, *Layered-to-spinel phase transition in Li_xMnO_2.* Electrochemical and Solid-State Letters, 2001. **4**(6): p. A78.

CHAPTER 5

UNDERSTANDING THE EFFECT OF CATIONIC SUBSTITUTION ON REDOX POTENTIAL IN LAYERED COMPOUNDS

As mentioned in the previous chapter, $Ni^{2+}/Ni^{3+}/Ni^{4+}$ redox potentials can be tuned with different cationic substitution in $LiNi_{1/3}TM1_{1/3}TM2_{1/3}O_2$ or $LiNi_{1/2}TM2_{1/2}O_2$ systems, where TM1 is a 3+ transition metal (Co^{3+}, Al^{3+}, Fe^{3+} etc.) and TM2 is a 4+ transition metal (Ti^{4+}, Zr^{4+}, Mn^{4+} etc.). In this chapter, the changes and trends in the nickel redox potentials are systematically compared and summarized. The electronic structure of those materials is studied in details in the attempt to understand these changes and trends. With a brief review of the literature on voltage tuning associated with lithium intercalation compounds; we adopt the concept of the inductive effect to describe in-depth understanding of ab initio calculated voltages in layered materials.

5.1 Ni Redox Potential in Different Compounds

Voltages of $LiNi_{1/3}TM1_{1/3}TM2_{1/3}O_2$ or $LiNi_{1/2}TM2_{1/2}O_2$ systems are calculated according to equation 5-1[1].

$$V(x) = -\frac{(\mu_{Li}^{cathode} - \mu_{Li}^{anode})}{ze} \qquad \text{Eq. 5-1}$$

where μ_{Li}^{anode} constant if metallic lithium is used as anode;

$$\mu_{Li}^{cathode} = \left(\frac{\partial G_f}{\partial x}\right)_{T,P,N_{host}}$$

In the thesis, G_f is approximated by E (total energy) because electronic and vibrational excitations are not considered. In these layered compounds it is possible to identify which redox couple is active in the particular voltage ranges, by examining the projected density of states on different cations, as tabulated in Table 5-I.

Table 5-I GGA calculated voltages of $LiNi_{1/3}TM1_{1/3}TM2_{1/3}O_2$ or $LiNi_{1/2}TM2_{1/2}O_2$ systems

Composition	**Ni^{2+}/Ni^{3+}**	**Ni^{2+}/Ni^{3+}**	***Ave. Voltage***	**Other Redox Pair**
$LiNi_{1/2}Mn_{1/2}O_2$	2.94V	3.51V	*3.22V*	
$LiNi_{1/2}Ti_{1/2}O_2$	3.13V	3.87V	*3.50V*	
$LiNi_{1/2}Zr_{1/2}O_2$	2.96V	3.85V	*3.41V*	
$LiNi_{1/2}Mo_{1/2}O_2$	Inactive		*N.A.*	Mo^{4+}/Mo^{6+}(2.91)
$LiNi_{1/3}Co_{1/3}Mn_{1/3}O_2$	2.82V	3.17V	*3.00V*	Co^{3+}/Co^{4+}(4.20)
$LiNi_{1/3}Fe_{1/3}Mn_{1/3}O_2$	2.95V	3.20~3.80V	*3.08V**	Fe^{3+}/Fe^{4+}(3.20~3.80)
$LiNi_{1/3}Al_{1/3}Mn_{1/3}O_2$	3.29V	3.33V	*3.31V*	Al^{3+}/Al^{4+}(5.05)
$LiNi_{1/3}Co_{1/3}Ti_{1/3}O_2$	2.98V	3.32V	*3.15V*	Co^{3+}/Co^{4+}(4.33)
$LiNi_{1/3}Co_{1/3}Zr_{1/3}O_2$	2.88V	3.45V	*3.16V*	Co^{3+}/Co^{4+}(4.28)

*Due to simultaneous redox reactions of Ni^{3+}/Ni^{4+} and Fe^{3+}/Fe^{4+}, the average voltage is calculated using a mid-point volatage 3.20V for Ni^{3+}/Ni^{4+} couple.

If the voltages at which the $Ni^{2+}/Ni^{3+}/Ni^{4+}$ couples are active in $LiNi_{1/2}Mn_{1/2}O_2$ are taken as the reference point, in $LiNi_{1/2}TM2_{1/2}O_2$ and $LiNi_{1/3}TM1_{1/3}TM2_{1/3}O_2$, Fe and Co doping lowers the voltages, while all other cation substitutions increase the delithiation voltages.

5.2 Computational Details

In order to find out how and why nickel redox potential are changed when substituted with different cations, we first look at the atomic arrangements of the supercells in the ab initio computations as shown in Figure 5-1. As mentioned before, the close packed oxygen planes have an ABCABC stacked oxygen frame. The stacking sequence of ordered transition metal planes is *a1b* in all calculations of this work. For consistency, the $LiNi_{1/2}TM2_{1/2}O_2$ system has the zig-zag ordering, and the $LiNi_{1/3}TM1_{1/3}TM2_{1/3}O_2$ has such ordering so that each Ni2+ ion has three 3+ and three 4+ ions as the nearest neighbor. Supercells of four formula units and three formula units are used in the two systems respectively.

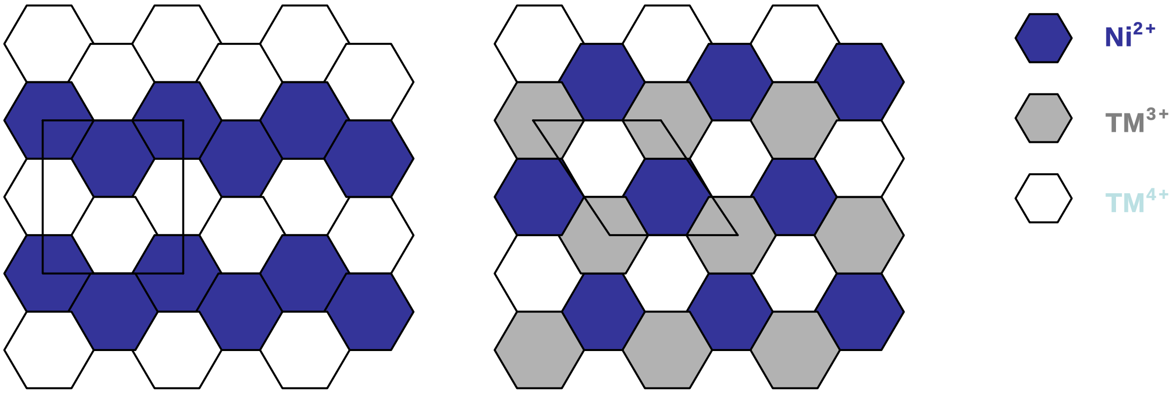

Figure 5-1 Ni, $TM1^{3+}$, $TM2^{4+}$ ordering in the supercells of $Li(Ni_{1/3}TM1_{1/3}TM2_{1/3})O_2$ and $Li(Ni_{1/2}TM2_{1/2})O_2$

5.3 Electronic Structure of Transition Metal Ion

To understand the reasons why the nickel redox potential can be tuned with cationic substitution, we have to exam the electronic structure of the nickel in the layered lithium transition metal oxides. In the layered crystal structure, the transition metal is octahedrally coordinated with oxygen. Electron p orbitals of oxygen overlap with s, p and d orbitals from the transition metal, forming bonding and anti-bonding levels. The oxygen p bands are filled and the transition metal d bands are empty or partially occupied. Crystal field theory [2-4] demonstrates that the interaction of the d orbitals with the electrostatic potential due to the negatively charged oxygen ions of the octahedron produces an increase in the energy of the e_g orbitals with respect to the energy of the t_{2g} orbitals. This happens because the e_g orbitals have lobes pointing toward the oxygen ions while the lobes of the t_{2g} orbitals point between oxygen ions. More accurately, the covalent mixing that exists between the transition metal ion and the oxygen ions affects their interaction. The e_g orbitals directly overlap with the p orbitals of oxygen forming bonding and antibonding levels, referred as e_g^b and e_g^*, as indicated in Figure 5-2. The separation between the bonding and anti-bonding levels becomes more pronounced as the difference in the energy of the metal d levels and the oxygen p levels widens.

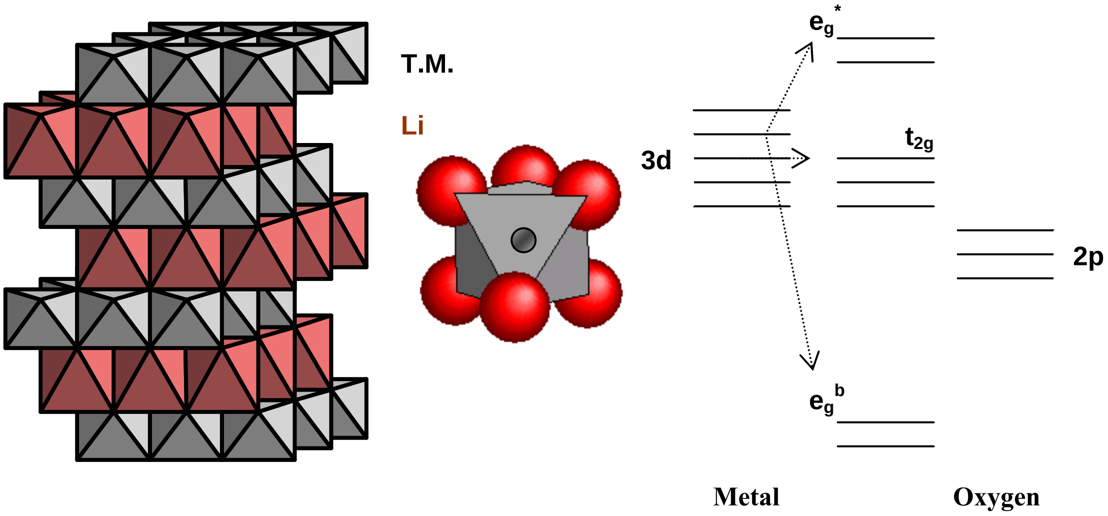

Figure 5-2 Schematic illustration of the bonding and anti-bonding levels that arise for a transition metal ion octahedrally coordinated by oxygen ions. The splitting is due to the hybridization between the valence electronic states of the transition metal ion with those of the oxygen ions.

The stronger is the cation-anion covalent bonding, the higher is the anti-bonding level. If the redox process consists of exchanging an electron with these levels (as in the case of Ni^{2+}/Ni^{4+}) then a higher energy will give a lower extraction voltage. This covalent bonding may be modulated by the strength of the covalent bonding of the anion with another neighboring cation without changing the primary structure. Modulation of the strength of the cation-anion covalence at a given cation by nearest-neighbor cations that compete for the same anion valence electrons is know as the **inductive effect** [5].

5.4 Tuning the Voltage by the Inductive Effect

Variation in voltages at which a given cation redox couple is active depends on two factors: (a) the magnitude of the crystalline electric field at the cation; and (b) the covalent contribution to the bonding, that may be modulated by the strength of the covalent bonding at the nearest-neighbor cations. The former may be estimated for a purely ionic model by a Madelung summation of the Coulomb fields from the other ions present; changes of structure alter primarily the Madelung energy. The stronger is the negative Madelung potential at a cation, the higher energy is a given redox couple; and the stronger is the covalent bonding of the electrons at a transition metal cation, the higher is the redox energy of that cation ion. [5] It should be noted that raising the energy of a given redox couple in a cathode lowers the voltage. In this study, we do not consider the Madelung energy since the structure of the compounds studied is always O3 type layered structure.

In NASICON materials, it has been illustrated that the Fe^{3+}/Fe^{2+} redox potential can be tuned by anionic substitution [6, 7]. In $Fe_2(SO_4)_3$, $LiFe_2(SO_4)_2(PO_4)$ and $Li_3Fe_2(PO_4)_3$, the redox voltages of Fe^{3+}/Fe^{2+} are 3.6V, 3.4V and 2.8V respectively because the Fe – PO_4 bonding is more covalent than the Fe – SO_4 bonding.

Similarly, we will also expect that changing of the counter cation in the Li(Ni,TM1,TM2)O_2 systems alters primarily the inductive effect, thus changes the Ni redox potential. Table 5-II shows the calculated redox potential of various metal cation in the O3 layered $LiTMO_2$ structure.

Tabel 5-II Redox potential of transition metal cation in the O3 layered structure $LiTMO_2$

M in $LiMO_2$	**Ti**	**V**	**Cr**	**Mn**	**Fe**	**Co**	**Ni**	**Cu**	**Mo**
Av. Voltage (V) for $MO_2/LiMO_2$	**2.33**	**2.93**	**3.22**	**2.95**	**3.52**[a]	**3.73**	**3.32**[b]	**3.70**	**2.93**[c]

All values obtained from reference [8], except

a. Notice the ground state for $LiFeO_2$ is not a layered structure
b. Calculated as 3.17V in Ref [8], the difference is due to different pseudo potential used in calculation
c. Calculated in this work

If charge transfer occurs mainly on the transition metal valence electron when Li is de-intercalated, the more amount of orbital mixing (covalent the bonding character) is, the higher is the redox couple M^{3+}/M^{4+} energy, thus the lower is the voltage.

For example, in $LiNi_{1/2}Mn_{1/2}O_2$, the redox potential of Ni^{2+}/Ni^{3+} and Ni^{3+}/Ni^{4+} are calculated as 2.94V and 3.51V, respectively [9]. While in $LiNi_{1/2}Ti_{1/2}O_2$, these values increase to 3.13V and 3.87V. Ti and Mn has very similar electronegativity (see Table 5-3), but Ti^{4+} is bigger in size and has no d electrons available, therefore there will be substantial amount of orbital mixing of Ti-O bonding than the Mn-O bonding in the structure. Substitution of Mn by Ti induces a reduction in the hybridization between the Ni d-levels and the oxygen p-levels, therefore decreases the covalency of Ni-O bonding, and lowers the Ni redox energy by a significant amount. Therefore, Ti doping raises the voltage at which Ni redox couple is active.

A similar situation occurs when Mn is substituted by Zr and Mo. In $LiNi_{1/2}Mo_{1/2}O_2$, the average voltage at which Mo^{4+}/Mo^{6+} redox couple is active, is calculated as 2.91V. Notice that in $LiMoO_2$ layered material, Mo^{3+}/Mo^{4+} redox potential is already as high as 2.93V. Presence of Ni in the transition metal layer obviously induces an increase in the covalent contribution to Mo – O bonding since there is less orbital mixing in Ni – O bonding (that is Ni – O bonding is more ionic than Mo – O bonding) .

Table 5-III Ionic radii, electronic configuration and electronegativity of various transition metal cations

	Ionic Radii	**Electronic Config.**	**δ***		**Ionic Radii**	**Electronic Config.**	**δ***
Ni^{2+}	0.69	3d8	1.91	**Mn^{4+}**	0.53	3d3	1.55
Co^{3+}	0.545	3d6	1.88	**Ti^{4+}**	0.605	3p6	1.54
Fe^{3+}	0.645	3d5	1.83	**Zr^{4+}**	0.72	4p6	1.33
Al^{3+}	0.535	2p6	1.61	**Mo^{4+}**	0.65	4d2	2.16

* electronegativity (Pauling scale) of the atom, data obtained from http://www.webelements.com/

5.5 Calculated Projected Density of States

Ni^{2+} has 8 electrons in the 3d levels, t_{2g} orbitals are fully occupied and two e_g orbitals are half-filled (high spin configuration, Figure 5-3. Counter cation substitution will affect the amount of orbital mixing (covalent contribution) in the Ni-O bonding, which can be further depicted by plots of projected density of states. In order to find a good reference point for energy comparison, oxygen s levels are plotted against Ni d levels, since one can assume that oxygen s-level energy is relatively insensitive to the type of cation ions in the layered compounds

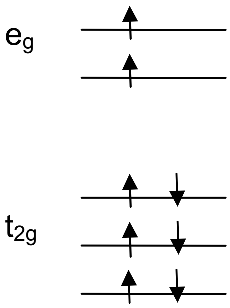

Figure 5-3 Electronic configuration of octahedrally coordinated Ni^{2+}

The following plots on the projected density of states on Ni d and O s levels demonstrate the shift in Ni redox potential towards more negative energy when Mn (Figure5-4a) & Figure 5-5a) is replaced by Ti (Figure 5-4b))in $LiNi_{1/2}Mn_{1/2}O_2$; towards more positive energy when Co is doped in the transition metal layer of $LiNi_{1/3}Co_{1/3}Mn_{1/3}O_2$ (Figure 5-5b)). Although the absolute shift in energy may not be directly correlated to the change in voltages, the comparison leads to the same conclusions as the ones in the previous section.

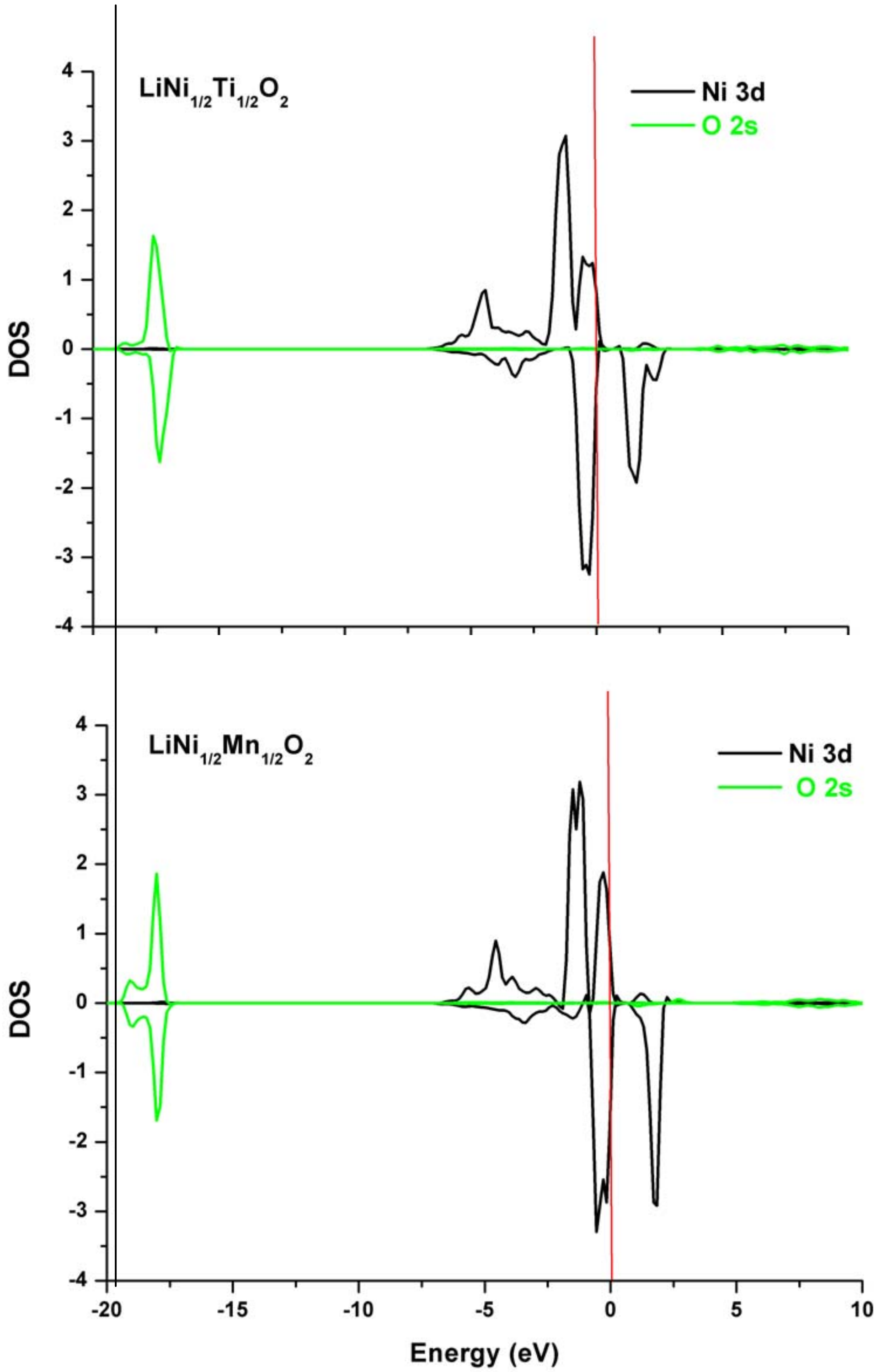

Figure 5-4 Projected density of states on Ni and O ions, notice that the energy is extended to low value in order to show the oxygen s-level, which is believed unchanged regardless of cation substitution. Fermi level is outlined by red line, by which it clearly shows that Ni redox potential is shifted to more negative value when Mn is substituted with Ti

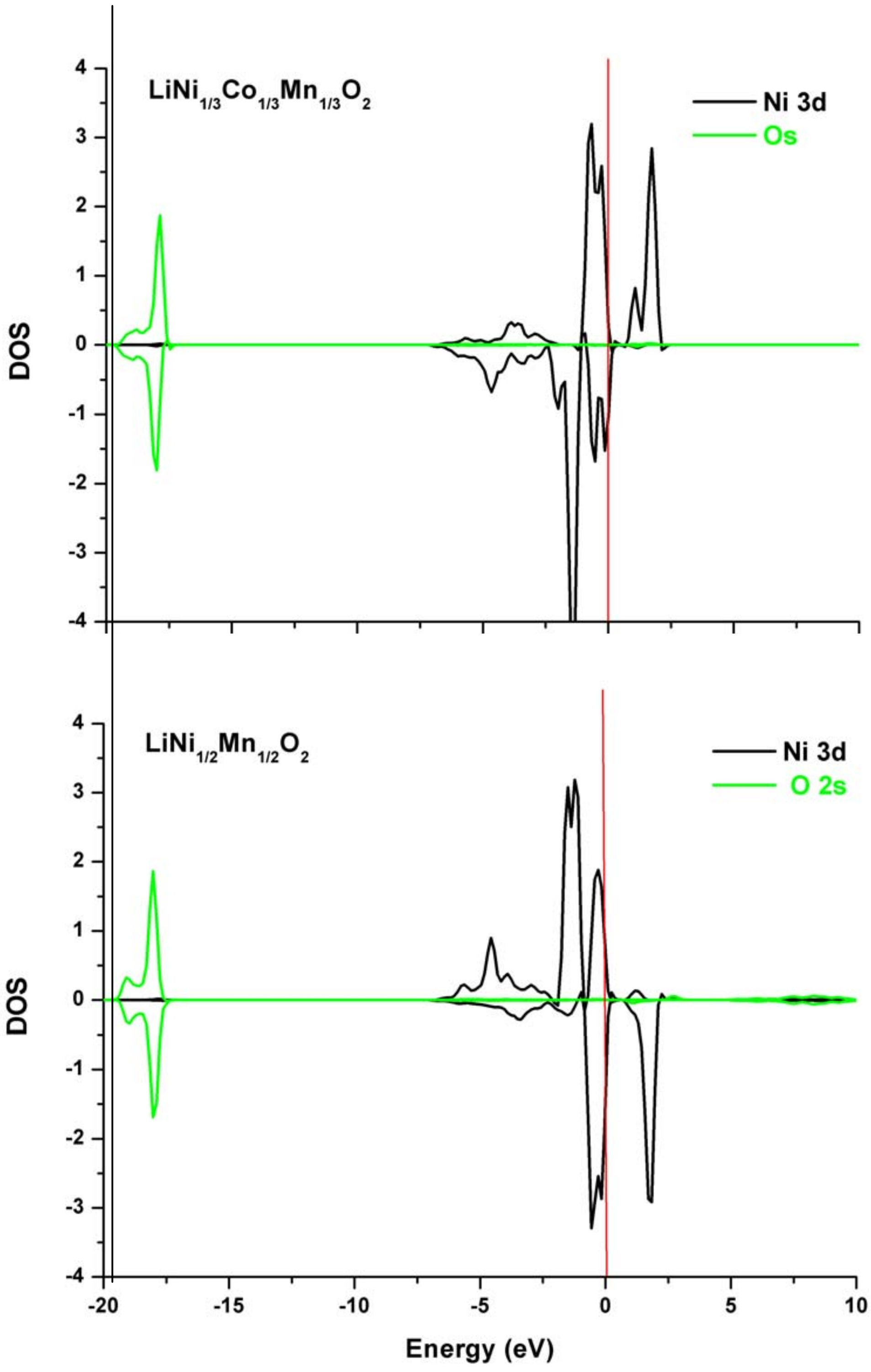

Figure 5-5 Projected density of states on Ni and O ions, notice that the energy is extended to low value in order to show the oxygen s-level, which is believed unchanged regardless of cation substitution. Fermi level is outlined by red line, by which it clearly shows that Ni redox potential is shifted to more positive value when Mn is substituted with Co

5.6 Experimental Evidence

Experimental data from Ohzuku & Makimura on $LiNi_{1/2}Mn_{1/2}O_2$ [10] and from Kang et al. on $Li_{0.9}Ni_{0.45}Ti_{0.55}O_2$ [11] are shown below for comparison. Although that the amount of cation disorder in the as-prepared materials and the polarization in the two battery systems are quite different, it can still been seen from the first charging curve that at cutoff voltage 4.8V, almost 8/9 Ni is active in $LiNi_{1/2}Mn_{1/2}O_2$, contributing to 235mAh/g in capacity. However, in Ti-doped material, only 1/2 of the theoretical capacity is achieved. It is speculated that high Ni^{3+}/Ni^{4+} redox potential beyond the cut-off voltage is the main reason for such low capacity.

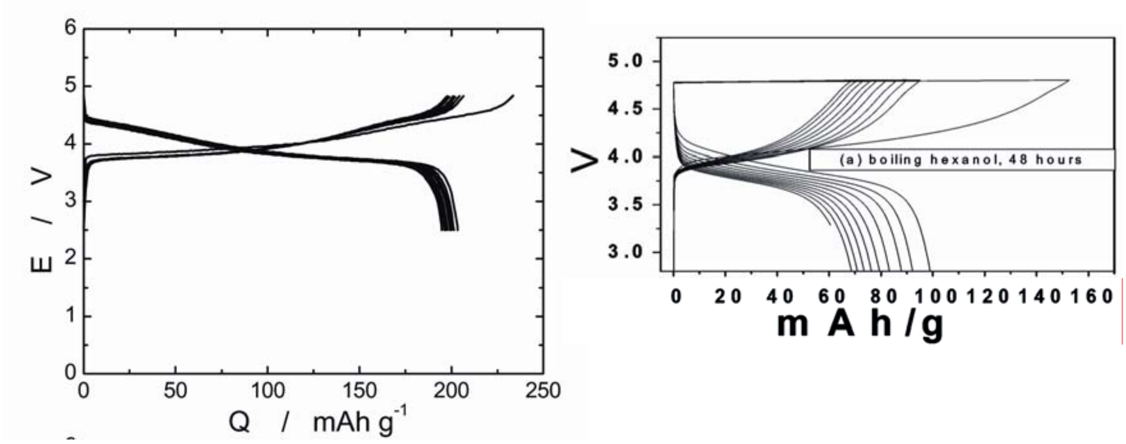

Figure 5-6 Experimental charge-discharge curves of (a) $LiNi_{1/2}Mn_{1/2}O_2$ [10] and (b) $Li_{0.9}Ni_{0.45}Ti_{0.55}O_2$ [11]cut-off voltage: 4.8V

Co – O boning is more ionic than Ni – O bonding, therefore the presence of Co in the transition metal layer increases the covalency in Ni – O bonding and raises the redox energy of the Ni redox couple. At a lower cut-off voltage such as 4.6V, about 225mAh/g capacity can be obtained experimentally in $LiNi_{1/3}Co_{1/3}Mn_{1/3}O_2$ compound, shown by Ohzuku&Makimura [12]. B.J. Hwang et al obtained the similar result – 218 mAh/g when charged upto 4.5V [13].

To see the shift in voltage more clearly, experimental data of $LiNi_{1/2}Mn_{1/2}O_2$ [14] and $LiNi_{1/3}Co_{1/3}Mn_{1/3}O_2$ are plotted together in Figure 5-8. The Co doing lowers the voltage slightly.

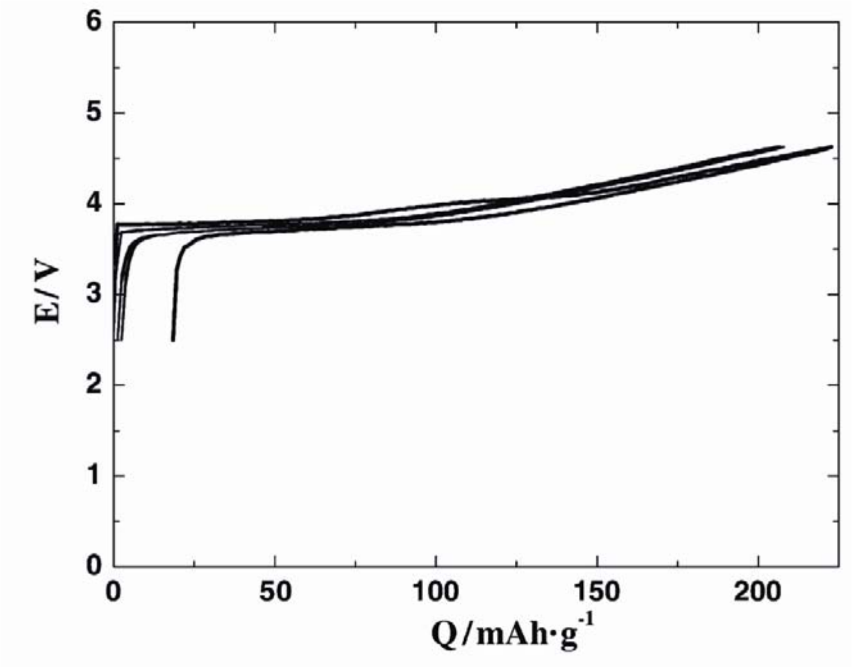

Figure 5-7 Experimental voltage curve of $LiNi_{1/3}Co_{1/3}Mn_{1/3}O_2$ with cut-off voltage 4.6V by Ohzuku & Makimura [12]

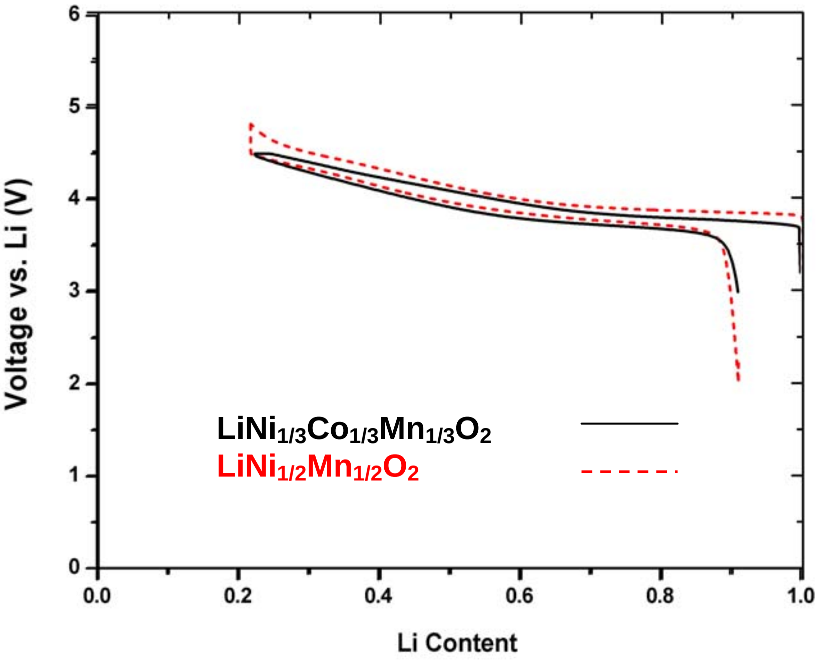

Figure 5-8 First-cycle charge and discharge curves of $Li[Ni_{1/2}Mn_{1/2}]O_2$ and $Li[Ni_{1/3}Co_{1/3}Mn_{1/3}]O_2$

In Figure 5-9, the charge-discharge curve of $LiNi_{1/3}Fe_{1/6}Co_{1/6}Mn_{1/3}O_2$ is plotted against that of $LiNi_{1/3}Co_{1/3}Mn_{1/3}O_2$, showing that Fe substitution further lowers the voltage [15].

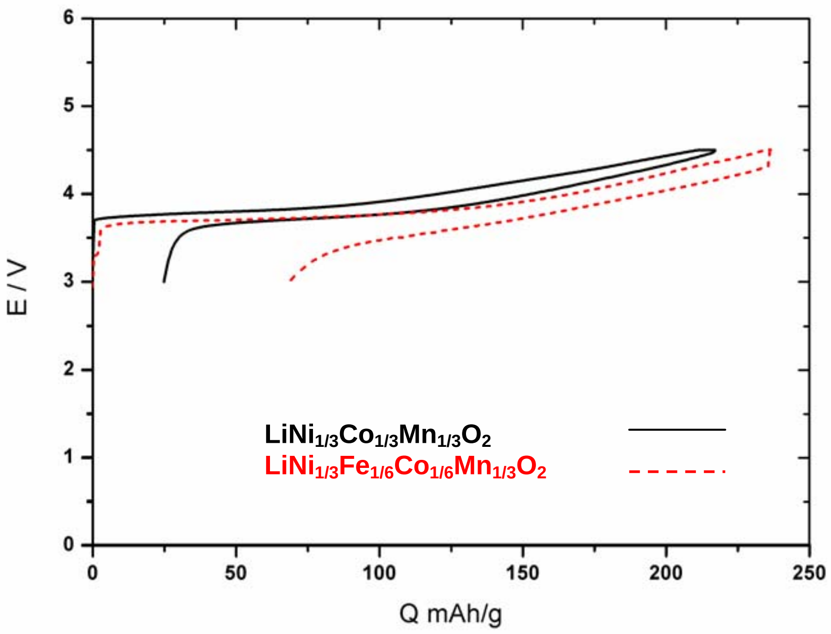

Figure 5-9 First-cycle charge and discharge curves of $Li[Ni_{1/3}Co_{1/3}Mn_{1/3}]O_2$ and $Li[Ni_{1/3}Fe_{1/6}Co_{1/6}Mn_{1/3}]O_2$

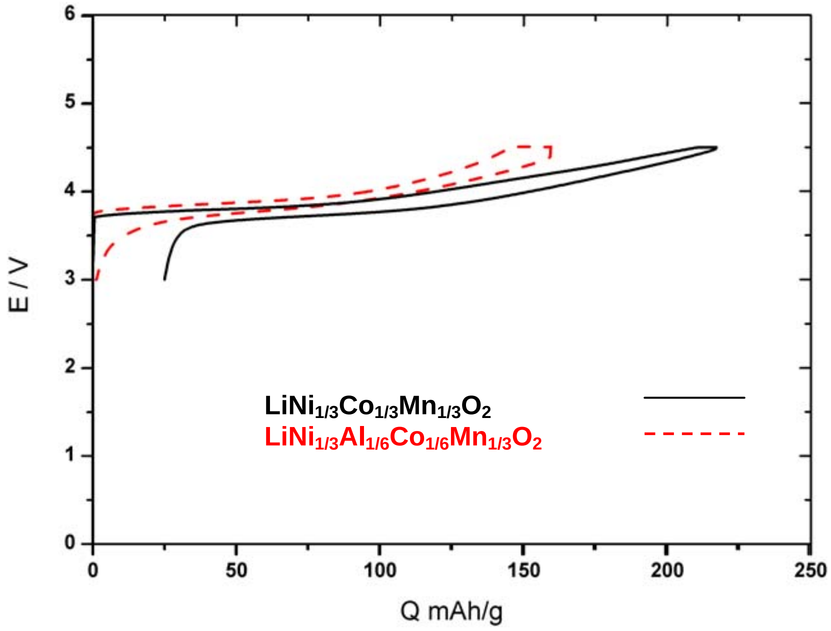

Figure 5-10 First-cycle charge and discharge curves of $Li[Ni_{1/3}Co_{1/3}Mn_{1/3}]O_2$ and $Li[Ni_{1/3}Al_{1/6}Co_{1/6}Mn_{1/3}]O_2$

Very recently, $LiNi_{1/3}Co_{1/6}Al_{1/6}Mn_{1/3}O_2$ has been successfully synthesized. [16, 17] At cut-off voltage of 4.5V, only about half of the theoretical capacity is obtained (Figure 5-10); indicating that certain amount of Ni is not activated at this cut-off voltage.

Myung et al. [18] also showed that Al and Ti doping raise the average voltages in the nickel manganese based layered compounds, as shown in Figure 5-11.

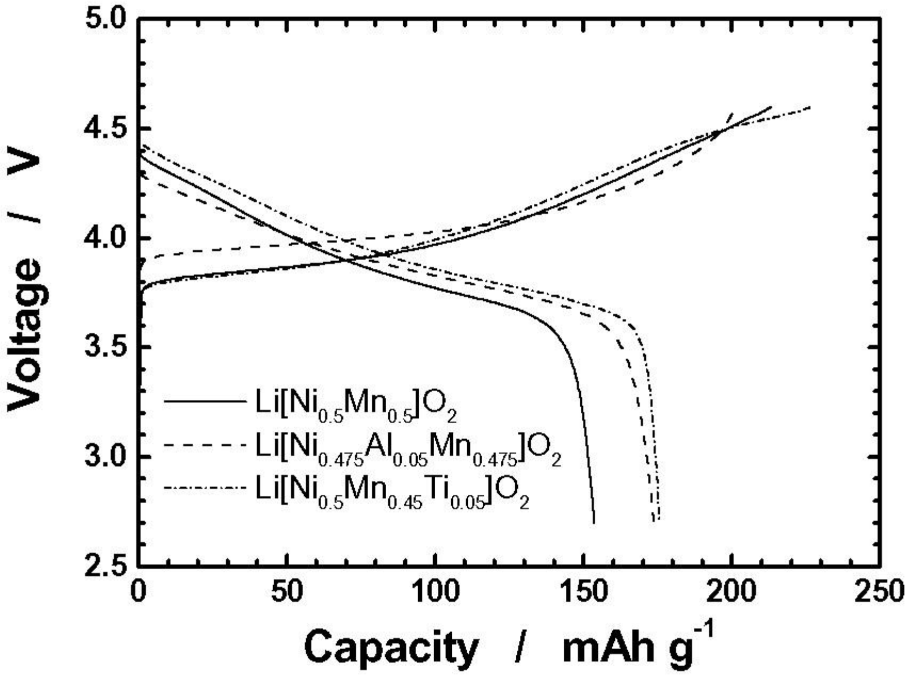

Figure 5-11 First-cycle charge and discharge curves of $Li[Ni_{1/2}Mn_{1/2}]O_2$, $Li[Ni_{0.475}Al_{0..05}Mn_{0.475}]O_2$, and $Li[Ni_{0.5}Mn_{0.45}Ti_{0.05}]O_2$

5.7 Conclusions

The inductive effect is introduced by cationic substitution in Li(Ni, TM1, TM2)O_2 layered compounds. For the counter cation that competes for the same anion (oxygen) valence, the amount of orbital mixing (covalent contribution) of the Ni-O bonding can be modulated. If the counter cation – oxygen bonding is more covalent, than the redox energy of Ni will be lowered, resulting in the increase in delithiation voltage. By tuning the voltage by cationic substitution, it is possible to gain from

- Increase in capacity with certain cut-off potential
- Higher structural stability
- Better electronic conductivity
- Lower cost

References:

1. W.R. McKinnon and R. Haering, eds. *Modern Aspects of Electrochemistry*. ed. J.O.M. Bockris and B.E. Conway. 1983, Plenum Press: New York.
2. C.J. Ballhausen, *Introduction to Ligand Field Theory*. 1962, New York: McGraw-Hill.
3. I.B. Bersuker, *Electronic Structure and Properties of Transition Metal Compounds: Introduction to the Theory*. 1996, New York: Wiley. p. 44-89
4. B.N. Figgis and M.A. Hitchman, *Ligand Field Theory and Its Applications*. 2000, New York: Wiley-VCH. p. 1-40
5. J.B. Goodenough, *General Concepts*, in *Lithium Ion Batteries: Fundamentals and Performance*, M. Wakihara and O. Yamamoto, Editors. 1998, Wiley-VCH: Weinheim.
6. C. Masquelier, et al., *New cathode materials for rechargeable lithium batteries : the 3-D framework structures* $Li_3Fe_2(XO_4)_3$ *(X = P, As)*. Journal of Solid State Chemistry, 1998. **135**: p. 228.
7. A.K. Padhi, V. Manivannan, and J.B. Goodenough, *Tuning the position of the redox couples in materials with Nasicon structure by anionic substitution*. Journal of the Electrochemical Society, 1998. **145**(5): p. 1518.
8. G. Ceder, A. Van Der Ven, and M.K. Aydinol, *Lithium-intercalation oxides for rechargeable batteries*. Journal of Metals, Minerals and Materials, 1998. **50**(9): p. 35-40.
9. J. Reed and G. Ceder, *Charge, potential, and phase stability of layered* $Li(Ni_{0.5}Mn_{0.5})O_2$. Electrochemical and Solid State Letters, 2002. **5**(7): p. A145-A148.
10. T. Ohzuku and Y. Makimura, *Layered lithium insertion material of* $LiNi_{1/2}Mn_{1/2}O_2$*: A possible alternative to* $LiCoO_2$ *for advanced lithium-ion batteries*. Chemistry Letters, 2001(8): p. 744-745.
11. K. Kang, et al., *Synthesis and electrochemical properties of layered* $Li_{0.9}Ni_{0.45}Ti_{0.55}O_2$. Chemistry of Materials, 2003. **15**(23): p. 4503-4507.
12. T. Ohzuku and Y. Makimura, *Layered lithium insertion material of* $LiCo_{1/3}Ni_{1/3}Mn_{1/3}O_2$ *for lithium-ion batteries*. Chemistry Letters, 2001(7): p. 642-643.
13. B.J. Hwang, et al., *A combined computational/experimental study on* $LiNi_{1/3}Co_{1/3}Mn_{1/3}O_2$. Chemistry of Materials, 2003. **15**(19): p. 3676-3682.
14. Y. Shao-Horn, *Personal Communication*. 2004.
15. Y.S. Meng, et al., *Combining ab initio computation with experiments for designing new electrode materials for advanced lithium batteries:* $LiNi_{1/3}Fe_{1/6}Co_{1/6}Mn_{1/3}O_2$. Journal of the Electrochemical Society, 2004. **151**(8): p. A1134-A1140.
16. B.J. Hwang, *Personal Communication on Al doping in lithium nickle manganese oxides*. 2004.
17. Y.K. Lin, et al. *New Layered Structure* $LiNi_{1/3}Co_{1/3}Al_{1/3}O_2$ *Prepared via Water-in-Oil Microemulsion Method*. in *International Meeting on Lithium Batteries IMLB12*. 2004. Nara Japan.
18. S.-T. Myung, et al. *Enhanced Electrochemical Properties of* $Li[Ni_{0.5}Mn_{0.5}]O_2$ *by Al and Ti Doping*. in *International Meeting on Lithium Batteries IMLB12*. 2004. Nara Japan.

CHAPTER 6

REVIEW ON THE LI[$NI_XLI_{1/3-2X/3}MN_{2/3-X/3}$]$O_2$ SYSTEM

6.1 Synthesis, Structure and Electrochemical Performance

Among the novel lithium intercalation compounds, layered O3 lithium nickel manganese oxides Li[$Ni_xLi_{1/3-2x/3}Mn_{2/3-x/3}$]$O_2$ are considered as one of the most promising candidates for future lithium ion batteries. [1, 2] In this series, only the structure of the end member Li_2MnO_3 (x = 0) is known in detail. It consists of a pure Li layer alternating with a $Li_{1/3}Mn_{2/3}$ layer in which Li and Mn are ordered to form a $\sqrt{3}a_{hex.} \times \sqrt{3}a_{hex.}$ superlattice. In the single crystal the stacking sequence of these ordered planes is a1c1, forming a structure with space group C2/m as illustrated in Figure 6-1. Generally, Li_2MnO_3 is considered as electrochemically inactive since charge compensation is unlikely to happen on Mn^{4+}. However, Robertson & Bruce recently demonstrate that at 4.6V, some electrochemical activity is found in Li_2MnO_3. The proposed mechanisms for lithium extraction are possible proton exchange or oxygen loss, but not redox reaction of Mn^{4+}/Mn^{5+}. $LiNi_{1/2}Mn_{1/2}O_2$ represents the other end member of the solid solution Li[$Ni_xLi_{1/3-2x/3}Mn_{2/3-x/3}$]$O_2$ (x = 1/2), its structure is still subject to debate. In $LiNi_{1/2}Mn_{1/2}O_2$ Ni can be oxidized from 2+ to 4+; half of the transition metal is electrochemically inactive Mn^{4+}. This material is most attractive since it has the highest theoretical capacity in the composition range 280mAh/g. However experimentally, this material exhibits different capacity and cycling performance with different preparation methods. Li_2MnO_3 is usually obtained through solid-state reaction of Li_2CO_3 and $MnCO_3$;

other members in the system, such as $LiNi_{1/2}Mn_{1/2}O_2$ are often synthesized by co-precipitation or sol-gel methods, followed by high-temperature firing 900-1000°C.

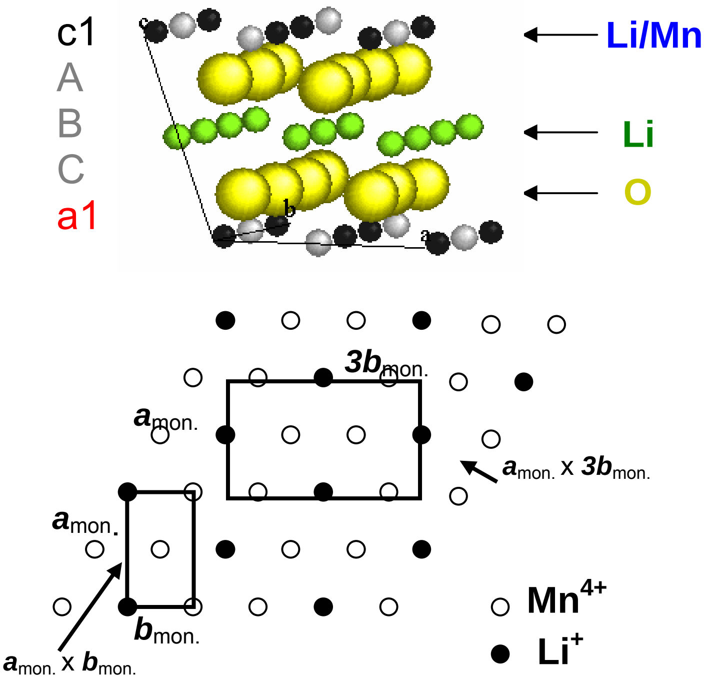

Fiugre 6-1 a) Crystal structure of Li_2MnO_3 b) $(001)_{hex.}$ projection of $Li_{1/3}Mn_{2/3}$ layer.

Ohzuku and Makimura obtained a reversible capacity of 200 Ah/Kg between the potential window 2.5-4.5V and a good cycling efficiency up to 30 cycles [1]. J.Dahn's group reported a stable capacity of 140 Ah/Kg in 3 to 4.4V and 200Ah/Kg in 2.5 to 4.8V [3]. The structure of $LiNi_{1/2}Mn_{1/2}O_2$ is usually indexed as a rhombohedral layered structure with space group R-3m. The separation of Li and transition metals in different layers is not perfect in $LiNi_{1/2}Mn_{1/2}O_2$, as Rietveld refinement of the structure based on the XRD and neutron diffraction data gives 8 to 10 percent Ni ions in the Li layer [1, 3]. Such mixing is naturally accompanied by the presence of Li ions in the transition metal (Ni, Mn) layers, which has been revealed by ^{6}Li MAS NMR studies[4, 5]. It is confirmed both by XANES experiment and first-principles calculations that in $LiNi_{1/2}Mn_{1/2}O_2$, the delithiation process occurs by oxidizing Ni^{2+} first to Ni^{3+}, and then when all the Ni^{2+} are oxidized, Ni^{3+} ions will be oxidized to Ni^{4+}.[6, 7]

From powder XRD studies, superstructure lattice peak were observed for compounds with $0 \leq x \leq 1/3$ in Li[$Ni_xLi_{1/3-2x/3}Mn_{2/3-x/3}$]$O_2$ [9]. Lu & Dahn proposed that for such compositions, Ni, Mn and Li ions are ordered in the transition metal layer on a $\sqrt{3}a_{hex.} \times \sqrt{3}a_{hex.}$ superlattice. They reported that ordering is not expected for the composition $x = 1/2$ as X-ray and neutron powder diffraction analyses reveal little evidence of superlattice peaks [8]. However, recent first-principles computation and Li-NMR analyses [5] reveal strong ordering interactions between Ni^{2+} & Mn^{4+} and Li^+ & Mn^{4+}, even for the composition $LiNi_{1/2}Mn_{1/2}O_2$. Monte Carlo simulations on perfectly stoichiometric material with no Li/Ni interlayer displacement show that short range ordering of Ni^{2+} and Mn^{4+} is retained near synthesis temperature range, though these simulations do not account for the presence of Li in the transition-metal layer [5]. NMR data reveals the preference for Li in the transition metal layers to be surrounded by 5-6 Mn. [5] Moreover, recent electron diffraction data of a $LiNi_{1/2}Mn_{1/2}O_2$ sample by Ohzuku *et al.* clearly shows a $\sqrt{3}a_{hex.} \times \sqrt{3}a_{hex.}$ superstructure relative to the parent hexagonal cell, but a detailed structural model was not discussed [9]. More recently, Van der Ven and Ceder proposed a structural arrangement in which cation layers with stoichiometry $Li_{11/12}Ni_{1/12}$ alternate with $Li_{1/12}Ni_{5/12}Mn_{6/12}$ in the octahedral sites of the O3 layered structure [10]. In the layer with composition $Li_{1/12}Ni_{5/12}Mn_{6/12}$ the cations arrange in flower-like patterns, which will be described in details later.

6.2 Anomalous Capacity when $0 \leq x < 1/2$

It is well known that lithium can be extracted from lithium manganese oxides by oxidizing Mn up to 4+. However, Li[$Ni_xLi_{1/3-2x/3}Mn_{2/3-x/3}$]$O_2$ ($0 \leq x < 1/2$) in which Mn already has 4+ oxidation state, demonstrated "overcharge" beyond Mn^{4+} when the materials were charged beyond 4.5V [11, 12]. The amount of lithium extracted beyond the theoretical amount is referred to as "anomalous" capacity, since the possible causes for such behavior have not been clearly identified.

For $x < 1/2$ compounds, some irreversible change occurred in the electrodes charged to 4.8V. A charge-discharge curve of Li_2MnO_3 by Robertson and Bruce (Figure 6-2) depicts the overcharging behavior clearly. A plateau near 4.6V is present. Near the plateau, the lattice parameter *a* remains almost constant, while *c* reduces rapidly [3, 12] Lu et al. claimed that the transition metal oxidation states are not changing during the plateau because *a* axis remains approximately constant; and the rapid decrease in *c* axis suggests that most of the Li is being removed from Li layer. Therefore, the charge compensation must come from the oxygen atom, which is effectively Li_2O is lost. Further oxygen extraction (during subsequent cycles) must be accompanied by Mn reduction. ($Mn^{4+} > Mn^{3+}$ below 3.5V). Such a large amount of oxygen loss may also cause substantial motion of the transition metal to the lithium layer, leading to poor lithium diffusion and large irreversible capacity. When the cells are charged between 2.0-4.4V, no anomalous behavior is observed. Their in-situ XRD experiment shows that all changes are completely reversible, as expected in the intercalation process.

Another end member of the solid solution Li_2MnO_3 (x = 0) was investigated by Robertson & Bruce [11, 13]. They suggested that many electrolytes contain H^+ due to the presence of PF_6^- anion, thus proton exchange with Li^+ may occur. They also claimed that oxygen loss appears to dominate during the overcharge of Li[$Ni_xLi_{1/3-2x/3}Mn_{2/3-x/3}$]$O_2$ (0 < x < 1/2) though H^+/Li^+ exchange is also evident. From the ex-situ XRD data of overcharged Li_2MnO_3, it was found that when H^+/Li^+ exchange occurred, the O3 structure (ABC stacking of oxygen layers) transformed to a P3 structure based on close-packed oxide layers stacked in AABBCC sequences [11]. The driving force for the adoption of this structure is the hydrogen bonding between adjacent oxide ion layers.

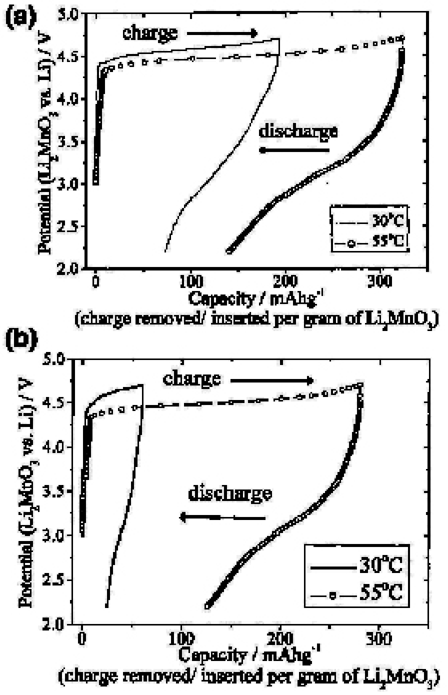

Figure 6-2 [11] First charge discharge curve of cells at different temperatures for Li_2MnO_3 prepared at a) 500 °C and b) 800 °C

6.3 Other Observations for $LiNi_{1/2}Mn_{1/2}O_2$

Shaju et al. [14] attempted a detailed study of $LiNi_{1/2}Mn_{1/2}O_2$ by GITT (Galvanic Intermittent Titration Technique) and EIS (Electrochemical Impedance

Spectroscopy). The GITT Diffusivity of Li was measured to be about $3*10^{-10}$ cm^2/s in the voltage range of 3.8V to 4.3V (minimum at 3.8V, which indicates some structural change at this voltage). EIS Impedance study shows a decrease in impedance at the start of charging, a minimum value is reached at 3.8V and then charge transfer resistance increases as the state of charge (SOC) increases. Bulk and surface resistance remain almost constant throughout the charging. According to the authors, the capacity fading when charged above 4.3V is due to the increased polarization at the end of the charging.

Many possible reasons for polarization have been proposed [14]:

1. Poor electronic charge-transfer due to unavailability of redox pair
2. Cation mixing
3. Phase change
4. Surface film, etc.

Various experimental and computational groups have investigated the above speculations; nevertheless ambiguity still exists in the characterization of charged $LiNi_{1/2}Mn_{1/2}O_2$.

The following experimental facts were observed as well:

- The parent structure R-3m changes to C2/m at half-delithiation $Li_{0.5}Ni_{1/2}Mn_{1/2}O_2$ [6]
- Most of Li go to tetrahedral sites at half-delithiation [15]
- Charge rates are important for the reversible capacity; 152mAh/g between 2.8V-4.3V with excellent cycleability is achieved if 10mA/g charge density

is applied. [16], only 87mAh/g can be obtained if the current density applied is 100mA/g [17].

- After 50 cycles, the R-3m frame is preserved, though the ordering has disappeared. [16]
- Short-range ordering disappears after a few cycles by NMR study (C.P.Grey, personal communication)
- Co, Al, Ti doping improve the reversible capacity and cycling ability [18]

6.4 First Principles and Monte Carlo Study in the System

Modeling of $LiNi_{1/2}Mn_{1/2}O_2$ was performed by first principles computations assuming that no Li is present in the transition metal layer [5]. The arrangement of Ni and Mn in the transition metal layer that has the lowest energy is the zig-zag ordering shown in Figure 6-3, in clear disagreement with experiments [19, 20]. However, this preliminary computation study does give some useful insight into the long and short-range order in $LiNi_{1/2}Mn_{1/2}O_2$. There is strong tendency for Ni^{2+} and Mn^{4+} to have long-range ordering on a triangular lattice. The kinetic Monte Carlo study shows that even when the material is synthesized above the long-range ordering temperature, short-range order exists and can grow as the material is cooled.

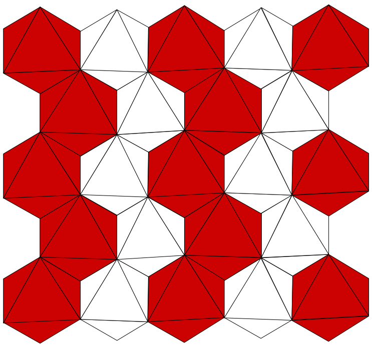

Figure 6-3 [5] Zig-zag in-plane ordering of Ni and Mn in $LiNi_{1/2}Mn_{1/2}O_2$

In a more recent study by Van der Ven and Ceder, Li is included in the transition metal layer for the computational study [10]. Using the results from ab initio computations with various Li, Ni and Mn arrangements, they predicted a flower-type ordering of Ni, Mn and Li in a $2\sqrt{3}a_{hex.} \times 2\sqrt{3}a_{hex.}$ unit cell with $Li_{1/12}Ni_{5/12}Mn_{1/2}$ stoichiometry layer of $LiNi_{1/2}Mn_{1/2}O_2$ (assuming there is 9% of Li in the transition metal layer), as shown in Figure 6-4. Each Li is surrounded by a hexagon of six Mn, which in turn is surrounded by a larger hexagon of twelve Ni. The similarity and difference between such flower ordering and the $\sqrt{3}a_{hex.} \times \sqrt{3}a_{hex.}$ ordering will be discussed in detail in Chapter 8 in combination with experimental and simulation results.

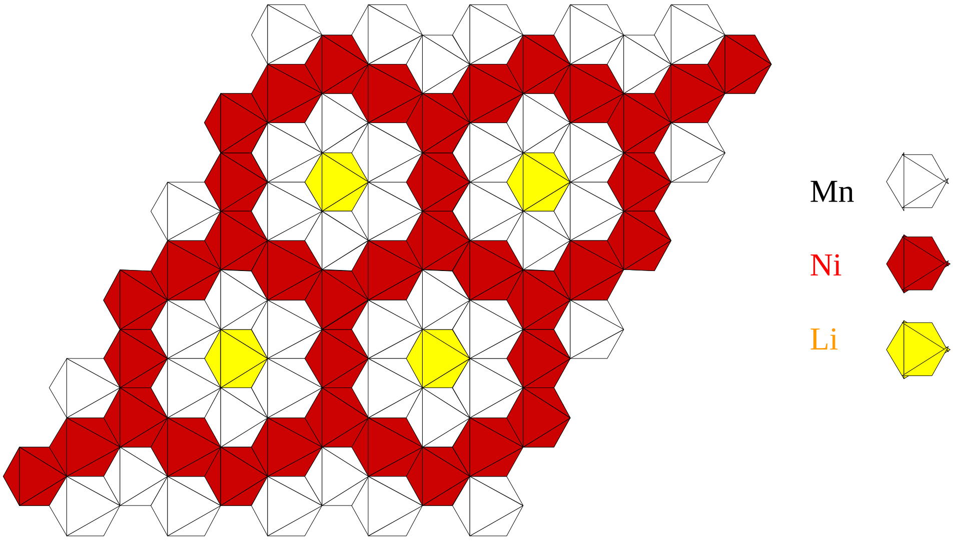

Figure 6-4 Flower in-plane ordering [5] of Ni and Mn in $Li_{11/12}Ni_{1/12}[Li_{1/12}Ni_{5/12}Mn_{1/2}]O_2$ (i.e. $LiNi_{1/2}Mn_{1/2}O_2$).

In addition, a combined study by first principles calculations and Li NMR spectroscopy on Li[$Ni_xLi_{1/3-2x/3}Mn_{2/3-x/3}$]$O_2$ system [21] shows that the lithium ions in the transition metal layer participate in the electrochemical process. They return to the sites upon lithium re-intercalation, though become increasingly unstable when the concentration of vacancies in the lithium layers increases. The octahedral lithium nearby three vacancies in the lithium layers is susceptible to migrate to the adjacent tetrahedral site in the lithium layer since no activation barrier exists for such process. [21] This proposed mechanism provides insight in understanding the capacity retention in the system.

6.5 Motivation and Objectives

A detailed understanding of the atomic arrangement in the solid solution will be essential in obtaining the structure – synthesis – properties relations. Optimization of the electrode materials and design of new electrode materials depend strongly on such knowledge. For this work, the main objective is to identify the three-dimensional crystal structures of Li[$Ni_xLi_{1/3-2x/3}Mn_{2/3-x/3}$]$O_2$, especially the two end members $LiNi_{1/2}Mn_{1/2}O_2$ ($x = 1/2$) and Li_2MnO_3 ($x = 0$), as well as to study the effect of compositions and synthesis conditions on long-range cationic ordering in the system.

References:

1. T. Ohzuku and Y. Makimura, *Layered lithium insertion material of* $LiNi_{1/2}Mn_{1/2}O_2$*: A possible alternative to* $LiCoO_2$ *for advanced lithium-ion batteries.* Chemistry Letters, 2001(8): p. 744-745.
2. Z.H. Lu, D.D. MacNeil, and J.R. Dahn, *Layered cathode materials* $LiNi_xLi_{(1/3-2x/3)}Mn_{(2/3-x/3)}O_2$ *for lithium-ion batteries.* Electrochemical and Solid State Letters, 2001. **4**(11): p. A191-A194.
3. Z.H. Lu, et al., *Synthesis, structure, and electrochemical behavior of Li* $Ni_xLi_{1/3-2x/3}Mn_{2/3-x/3}O_2$. Journal of the Electrochemical Society, 2002. **149**(6): p. A778-A791.
4. W.S. Yoon, et al., *Li-6 MAS NMR and in situ X-ray studies of lithium nickel manganese oxides.* Journal of Power Sources, 2003. **119**: p. 649-653.
5. W.S. Yoon, et al., *Local structure and cation ordering in O3 lithium nickel manganese oxides with stoichiometry* $LiNi_xMn_{(2-x)/3}Li_{(1-2x)/3}O_2$ *- NMR studies and first principles calculations.* Electrochemical and Solid State Letters, 2004. **7**(7): p. A167-A171.
6. Y. Arachi, et al., *Structural change of* $Li_{1-x}Ni_{0.5}Mn_{0.5}O_2$ *cathode materials for lithium-ion batteries by synchrotron radiation.* Chemistry Letters, 2003. **32**(1): p. 60-61.
7. J. Reed and G. Ceder, *Charge, potential, and phase stability of layered* $Li(Ni_{0.5}Mn_{0.5})O_2$. Electrochemical and Solid-State Letters, 2002. **5**(7): p. A145.
8. Z.H. Lu, Z.H. Chen, and J.R. Dahn, *Lack of cation clustering in* $LiNi_xLi_{1/3-2x/3}Mn_{2/3-x/3}O_2$ $(0 < x \leq 1/2)$ *and* $LiCr_xLi_{(1-x)/3}Mn_{(2-2x)/3}O_2$ $(0 < x < 1)$. Chemistry of Materials, 2003. **15**(16): p. 3214-3220.
9. T. Ohzuku and Y. Makimura. *Structural Chemistry and Electrochemistry of* $LiNi_{1/2}Mn_{1/2}O_2$ *for Advanced Lithium Batteries*. in *Abstract No. 1079 of the Electrochemical Society Spring Meeting*. 2003. Paris, France.
10. A. Van der Ven and G. Ceder, *Ordering in* $Li_x(Ni_{0.5}Mn_{0.5})O_2$ *and its relation to charge capacity and electrochemical behavior in rechargeable lithium batteries.* Electrochemistry Communications, 2004. **6**: p. 1045-1050.
11. A.D. Robertson and P.G. Bruce, *Mechanism of electrochemical activity in* Li_2MnO_3. Chemistry of Materials, 2003. **15**(10): p. 1984-1992.
12. Z.H. Lu and J.R. Dahn, *Understanding the anomalous capacity of* $Li/LiNi_xLi_{(1/3-2x/3)}Mn_{(2/3-x/3)}O_2$ *cells using in situ X-ray diffraction and electrochemical studies.* Journal of the Electrochemical Society, 2002. **149**(7): p. A815-A822.
13. A.D. Robertson and P.G. Bruce, *The origin of electrochemical activity in* Li_2MnO_3. Chemical Communications, 2002(23): p. 2790-2791.
14. K.M. Shaju, G.V.S. Rao, and B.V.R. Chowdari, *Li-ion kinetics and polarization effect on the electrochemical performance of* $Li(Ni_{1/2}Mn_{1/2})O_2$. Electrochimica Acta, 2004. **49**(9-10): p. 1565-1576.
15. H. Kobayashi, et al., *Structural determination of* $Li_{1-y}Ni_{0.5}Mn_{0.5}O_2$ $(y=0.5)$ *using a combination of Rietveld analysis and the maximum entropy method.* Journal of Materials Chemistry, 2004. **14**(1): p. 40-42.
16. Y.K. Sun, C.S. Yoon, and Y.S. Lee, *Electrochemical properties and structural characterization of layered Li* $Ni_{0.5}Mn_{0.5}O_2$ *cathode materials.* Electrochimica Acta, 2003. **48**(18): p. 2589-2592.

17. B.L. Cushing and J.B. Goodenough, *Influence of carbon coating on the performance of a* $LiMn_{0.5}Ni_{0.5}O_2$ *cathode.* Solid State Sciences, 2002. **4**(11-12): p. 1487-1493.
18. S.H. Kang, et al., *Layered* $Li(Ni_{0.5-x}Mn_{0.5-x}M'_{(2x)})O_2$ *(M ' = Co, Al, Ti; x = 0, 0.025) cathode materials for Li-ion rechargeable batteries.* Journal of Power Sources, 2002. **112**(1): p. 41-48.
19. Y. Makimura, N. Nakayama, and T. Ohzuku. *Structural Chemistry and Electrochemistry of* $LiNi_{1/2}Mn_{1/2}O_2$ *for Advanced Lithium Batteries*. in *The Electrochemical Society Meeting*. 2003. Paris France.
20. Y.S. Meng, G. Ceder, C.P. Grey, W.-S. Yoon, and Y. Shao-Horn, *Understanding the Crystal Structure of Layered* $LiNi_{0.5}Mn_{0.5}O_2$ *by Electron Diffraction and Powder Diffraction Simulation.* Electrochemical and Solid State Letters, 2004. **7**(6): p. A155.
21. C.P. Grey, et al., *Electrochemical Activity of Li in the Transition-Metal Sites of O3* $Li[Li_{(1-2x)/3}Mn_{(2-x)/3}Ni_x]O_2$. Electrochemical and Solid State Letters, 2004. **7**(9): p. A290-A293.

CHAPTER 7

KINEMATICS OF DIFFRACTION – TEM, XRD AND ND

Knowledge on how atoms are arranged into crystal structures is the foundation by which we gain our understanding of the synthesis, microstructures and properties of materials. Diffraction techniques have been applied for crystal structure analysis in materials science over a few decades and can be broadly categorized into powder diffraction and single crystal diffraction. Most common radiation sources of diffraction experiment are X-ray (soft and hard), neutron and electron. It is tempting to give a unified treatment to the X-ray, neutron and electron diffraction. However such complete theoretical explanation of diffraction physics is beyond the scope of this thesis. The simple theoretical and practical issues for those techniques are discussed in this chapter; the unique advantages of each diffraction technique as well as its limitations will be explained in detail. And the message that *none of the diffraction technique should be used in isolation to solve a materials problem* will hopefully be clear. In this work we will demonstrate how the combination of all help to characterize the atomic arrangement of lithium nickels manganese oxides, which is essential in understanding and optimizing the materials' electrochemical properties.

7.1 Different Sources of Radiation and Their Interaction with Matter

Simply speaking, diffraction is a three-dimensional extension of simple Fraunhofer (far-field) diffraction theory applied to the idealized case of infinite periodic object with sharply defined diffracted beam and a set of lattice points in reciprocal space [1]. The basic mathematical tool used is Fourier series. However, greater sophistications exist for different radiation sources since they interact with matter differently.

X-rays

X-rays are generated when energetic electrons lose energy. There are two major sources for X-rays: synchrotron radiation and cathode ray tube. The former offers higher intensity and better resolution, however in laboratory scale, the latter is widely used. Facilities for synchrotron radiation experiments are available only at several national/international laboratories. Conventional X-ray tubes are vacuum tube diodes, where their filaments are biased typically at a few tens of kV. Electrons are emitted thermoionically from the filament, and accelerate into the anode, where X-rays are generated. The characteristic wavelengths of X-rays vary from 2.28 Å for chromium to 0.71 Å for molybdenum, the most commonly used being the copper radiation of wavelength 1.54 Å.

X-rays are scattered by the electrons in a material through the interaction between the negatively charged electrons and the electromagnetic field of the incident X-rays [2]. The electrons in the material respond to the applied field of the X-ray flux, oscillating with the frequency of the X-ray beam. These accelerated charged particles emit their own electromagnetic field, thus the resultant field is called the scattered wave [2, 3]. For light elements, for example oxygen, whose electron density is weak, it is extremely difficult, if not impossible to directly determine the position of light atoms by X-rays.

Electrons

For many years, the electron source was a sharply-bent tungsten wire being electrically heated. At high enough temperatures, thermoioinc emission occurs and electrons are emitted. The rate of the thermoioinc emission is proportional to exp(-Φ/kT), where Φ is the work function of tungsten. (Φ for tungsten is 4.5eV). The lower work function of LaB6 (2.7eV) has made it a preferred material for thermoioinc electron guns, though the cost of LaB6 is much higher than that of tungsten. On the other hand, cold field emission gun (FEG) is an excellent point source of radiation, it is highly monochromatic and is absent of thermal spread. A positive electrode is placed near a sharp metal tip (usually tungsten), a strong electric field at the tip causes some electrons to overcome the work function and leave the metal. Nevertheless, cold FEG guns require ultrahigh vacuum system (10^{-8}-10^{-9} Pa) in order to suppress the damage by ions of gas atoms that accelerated into the tip in the high electric field imposed.

Electrons are scattered by both the electrons and the nuclei in a material; it is not a field-to-field exchange as in the case of X-rays. Therefore, electrons are scattered much more strongly than X-rays. [3, 4] However, the requirement of specimen and dynamic effects make ED a less conventional technique in structural analysis as XRD.

Neutrons

The neutrons for diffraction experiments are usually the thermal neutrons which are in thermal equilibrium with the atoms in a nuclear reactor. They have an average energy of about 0.025eV; however, the spread of energies or wavelengths in the beam of neutrons obtained from a reactor is quite broad. For diffraction experiment, a narrow range of wavelength is selected by use of a monochromator crystal or by a time-of-flight chopper device which selects a range of neutron velocities.

The main interaction of a matter with neutron is with the nucleus. Neutrons are not appreciably scattered by the electrons of a matter. [1] Neutron diffraction is not only suitable for structural analysis, especially for locating light elements; but also excellent for studying time-dependent processes, such as phonons and magnons. The kinematics is derived mainly in the context of nuclear physics. A different set of jargon is used, for instance, scattering cross section rather than atomic scattering amplitude is used in neutron diffraction analysis.

Despite the different physical mechanisms in the three diffraction processes, together they provide complementary information about the atomic arrangements in materials. There are a lot of similarities in these three diffraction techniques; the most well known one is Bragg's law [2], which will be discussed next.

7.2 Simple Diffraction Physics

7.2.1 The Bragg's Law and Laue Condition

In the geometric optics approximation for diffraction, Bragg's law is stated as

$$n\lambda = 2\, d_{hkl} \sin\theta \qquad \text{Eq. 7-1}$$

where n is the order of reflection. λ is the wavelength of the incident wave, d is the spacing of particular set of crystallographic planes and θ is the angle between the incident beam and the crystallographic planes, as shown in Figure 7-1. The right hand side sets the difference in path length for the ray scattered from plane A and the ray scattered from the plane B. The left hand side gives the condition for constructive interference (and therefore strong diffraction).

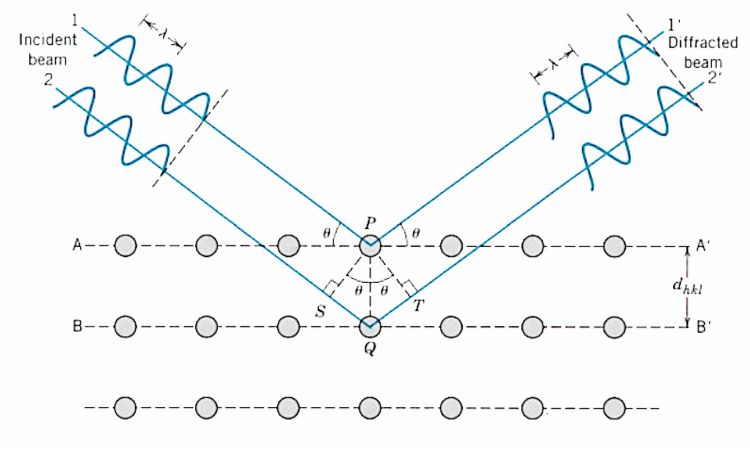

Figure 7-1 Schematics of X-ray diffraction by planes of atoms

Diffraction is a wave interference phenomenon and it is more appropriate to express the diffraction condition in terms of wave vectors. Suppose that the incident wave vector $\vec{k}_0$ and the scattered wave vector have the same length (that is elastic scattering), the angle between $\vec{k}$ and $\vec{k}_0$ is equivalent to the 2θ in the Bragg's law.

$$\Delta k = \left|\vec{k} - \vec{k}_0\right| = 2\left|\vec{k}\right| \sin\theta = \frac{4\pi}{\lambda} \sin\theta \qquad \text{Eq. 7-2}$$

Notice that $\Delta \vec{k}$ is the normal of the diffraction planes, as shown in Figure 7-2. This is called the Laue condition [3] and is more effective to use in diffraction physics.

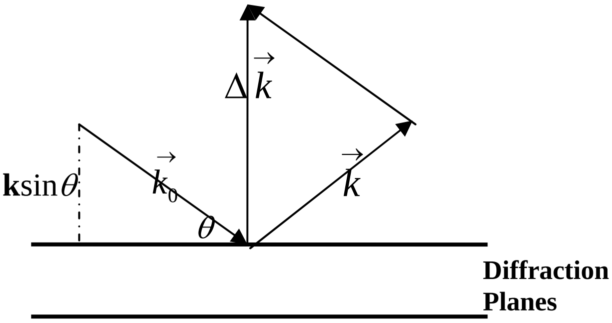

Figure 7-2 Relationship between $\Delta \vec{k}$ and θ for elastic scattering

7.2.2 Real and Reciprocal Space

The kinematical scattering amplitudes can be expressed in terms of the Fourier transform of a distribution of electron density in real space.[1] The Fourier transform space is often referred to as the reciprocal space. It is much more convenient to understand the diffraction effects in terms of reciprocal lattice.

In real space, a position vector $\vec{r}$ has coordinates (x,y,z), in reciprocal lattice, a position vector $\vec{u}$ has coordinates (u,v,w). A distribution of electron density in real space can be expressed as

$$F(\vec{u}) = \int \rho(\vec{r}) \exp\left\{2\pi i \vec{u} \bullet \vec{r}\right\} d\vec{r} \qquad \text{Eq. 7-3}$$

If the electron density distribution is assumed to be the sum of the electron density attributed by individual atoms, then

$$F(\vec{u}) = \sum_i f_i(\vec{u}) \exp\left\{2\pi i \vec{u} \bullet \vec{r}_i\right\} \qquad \text{Eq. 7-4}$$

The values for atomic scattering factor can be found in the International Tables for Crystallography Vol. C [5].

For a periodic lattice in real space with lattice parameters a, b, c, the corresponding reciprocal lattice is associated with a*, b*, c*. The relations are:

$$a^* = \frac{b \times c}{V},\ b^* = \frac{c \times a}{V},\ c^* = \frac{a \times b}{V}$$

where V is the unit cell volume. In the case of orthogonal lattice, a* = 1/a, b*= 1/b and c*= 1/c. Diffraction occurs when $\Delta \vec{k}$ is a vector of the reciprocal lattice.

7.2.3 Ewald Sphere Construction

The Laue condition for diffraction can be demonstrated by a geometrical construction, named the Ewald Sphere Construction [2]. Assume that the reciprocal lattice is simple cubic, as shown in Figure 7-3, the incident wave vector $\vec{k}_0$ and possible diffracted wave vector $\vec{k}$ are shown in the picture. $\vec{k}_0$ is always placed at a point of the reciprocal lattice, thus the condition $\Delta \vec{k} = 0$ always satisfies the Laue condition. This is the reason why a forward-scattered beam in the electron diffraction pattern is always observed. In elastic scattering, the length of $\vec{k}$ equals the length of $\vec{k}_0$, which is the radius of the Ewald sphere. If the end of the $\vec{k}$ touches a reciprocal lattice point, the Laue diffraction condition occurs.

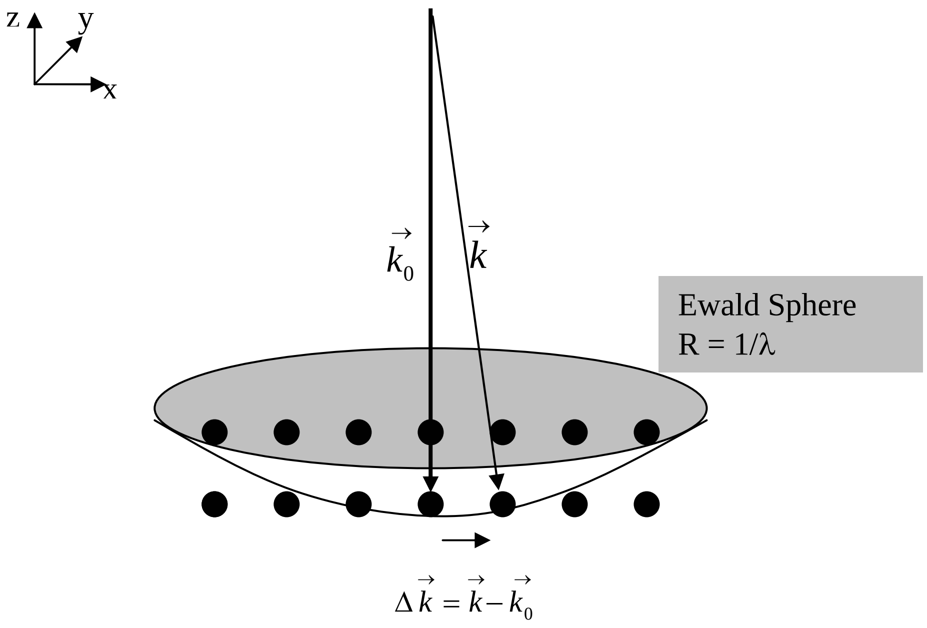

Figure 7-3 Ewald sphere construction

In X-ray diffraction, the length of $\vec{k}_0$, which is in the order of 1/λ (about 1Å^{-1}) is comparable to the reciprocal lattice spacing. The Ewald sphere is strongly curved. For electron diffraction, however, the length of the wave vector is much longer than the reciprocal lattice (the wave length of 200keV electrons is about 0.02507Å), the Ewald sphere is relatively flat. Therefore, $\Delta\vec{k}$ is nearly perpendicular to $\vec{k}_0$. In practice, the diffraction intensity is distributed around a reciprocal lattice point with finite volume, so $\Delta\vec{k}$ does not have to exactly equal a reciprocal lattice for diffraction to occur.

7.2.4 Perfect and Defective Crystal

The translational symmetry of unit cells on a lattice is the essential feature of the crystal that enables constructive interferences of wavelets emitted by many atoms.

Although real crystals contain many types of defects, including point defects, dislocations, stacking faults etc., which may or may not destroy the translational symmetry of the crystal, it is reasonable to think the main diffraction effects as coming from an ideally periodic crystal.

7.2.5 Kinematical Approximation and Dynamic Diffraction

Kinematical approximation is also known as *single scattering* approximation. Coherent multiple scattering is called dynamical diffraction. [1] The condition for kinematical diffraction implies that the amplitude of the single scattered radiation is very small compared with the incident wave amplitude and the amplitude of the doubly- and multiply-scattered radiation is negligible compared with the singly scattered. The limit of the applicability of kinematical approximation depends very much on the radiation source. [1, 3] In the case of x-rays and neutrons, the interaction with atoms is so weak that the energy associated with diffracted waves can be concentrated into one or two sharply defined directions by three-dimensional diffraction before the incident beam loses much energy. Doubly or multiple diffraction occurs only if another crystal region (perfectly ordered, in absent of defects) is set at the right angle for Bragg condition, which is seldom satisfied since the radius of the Ewald sphere is comparable to the reciprocal lattice.

While for electron diffraction, the interaction with atoms is much stronger so that multiple scattering may not be ignored. Well defined diffracted beams are not generated before the incident beam loses its energy. Multiply scattering becomes important with a distance in the order of one or two hundred Armstrong for light atoms and less for heavy atoms. Fortunately, coherent multiple scattering has been satisfactorily taken care of for experiments by the use of special theoretical treatments.[6-8]

7.3 Powder Diffraction vs. Single Crystal Diffraction

Both powder and single crystal diffraction are used in structural analysis. However, structure determination from powder diffraction data is much more difficult than from single crystal diffraction data. This is associated almost entirely with the collapse of the three dimensions of crystallographic information onto the single dimension of a powder diffraction pattern. [9] If representative single crystals are available, the single crystal diffraction is the preferred method. The reason that powder diffraction is always used for structure analysis is that there are many materials for which no single crystals are easily available. However, when only powder sample is available, there may be small crystallites that are suitable for single crystal diffraction, if a suitable technique such as selected area electron diffraction (SEAD) is applied. These small crystals do, however, suffer from the risk that they may not be representative of the bulk powder. Therefore, it is essential to collect a powder diffraction pattern as well as that the structure information obtained from the microcrystallites corresponding to that of the bulk material.

7.4 The Structure Determination Process

The structure determination process can be viewed as an optimization process. Sample quality, type of radiation source to use, suitable experimental conditions, determination of the space group, fitting all the structural parameters and so on, have to be optimized with respect to the type of sample itself. To be relevant to this work, the structure determination process for lithium nickel manganese oxides is illustrated in the flow chart below in Figure 7-4.

The Rietveld method [10], which is an achievement that has greatly enhanced the power of the powder diffraction experiments, has been widely used in the structural analysis. However, the Rietveld method is a refinement process, thus it requires that an approximation to the correct structure be known in advance. If a structural model is not available, it must first be determined. The same is true for fitting single-crystal electron diffraction patterns. Thus, chemical information and structural information obtained from other techniques, including first principles computation, are necessary for the structure determination processes.

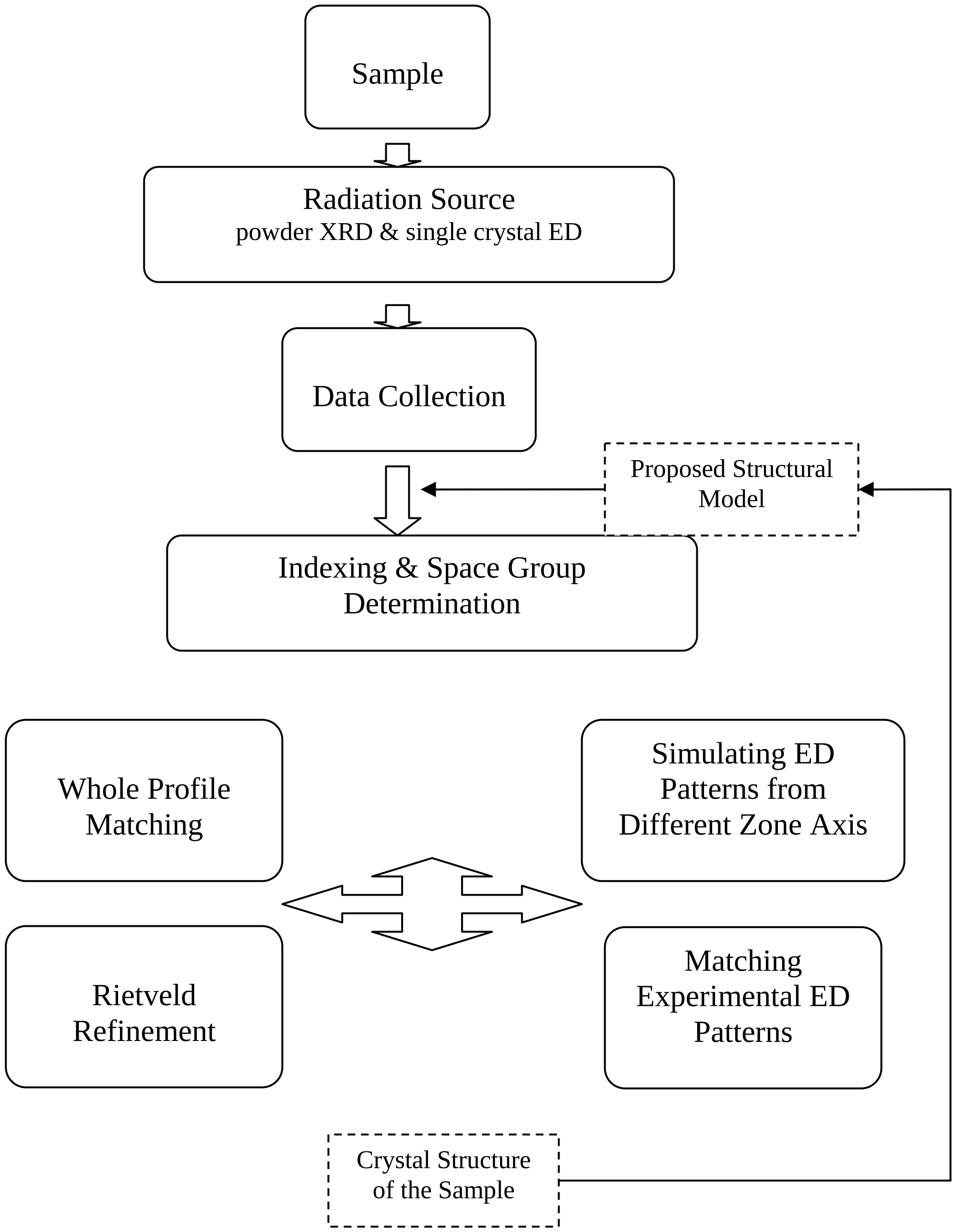

Figure 7-4 The structure determination process

7.5 Selected Area Electron Diffraction

The major experimental tool used in this part of the work is Selected Area Electron Diffraction (SAED). A detailed description on the SEAD technique is given, including its advantages and limitations. It is important to realize that a combination of experimental techniques that probe different relevant length scales is necessary to truly understand the structure of complex solids such as $Li[Ni_xLi_{1/3-2x/3}Mn_{2/3-x/3}]O_2$ system. The role of computer simulation of electron diffraction is also explained in this chapter.

A modern TEM provides two modes for obtaining diffraction patterns from individual crystallites – Selected area electron diffraction (SAED) and convergent-beam electron diffraction (CBED). The former is useful for obtaining diffraction patterns from regions as small as 0.5μm in diameter; the latter is also called nanodiffraction, where a focused electron probe beam is used to obtain diffraction patterns from regions as small as 10Å. We are emphasizing SAED here, since we use it in this work.

The ray diagram for TEM when it is operating in SAED mode is shown in Figure 7-5. The intermediate lens is focused on the back focal plane of the objective lens and the transmitted beam and all the diffracted beams are imaged. A second aperture (selected area aperture) is positioned in the image plane of the objective lens, as a means of confining the diffraction pattern to a selected area of the specimen. The specimen is first examined in *image mode* until a region of interest (or individual crystallite) is found. The selected area aperture is then inserted and positioned around this feature. The microscope is then switched to *diffraction mode* to obtain an electron diffraction pattern.

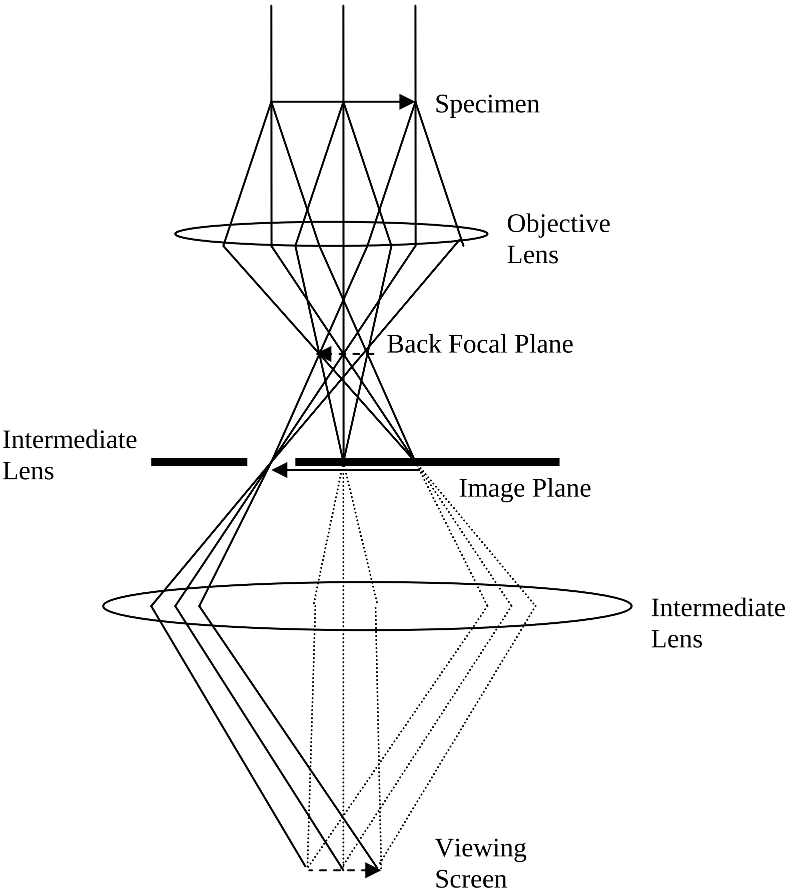

Figure 7-5 Selected Area Electron Diffraction (SAED) mode – tracing the rays to confirm that the intermediate aperture provides a sampling of the transmitted and all diffracted rays [3]

Dynamic Effect

Dynamic diffraction is very important in electron diffraction, since the electron beam interacts so strongly with the atoms in the crystal. As shown in Figure 7-6, the beam that has been strongly Bragg-diffracted once is necessarily in the perfect Bragg orientation to be diffracted back into the direct beam by the same set of planes. This re-diffracted beam is perfectly oriented to be diffracted again. The likelihood of this process increases with the thickness of the specimen. Forbidden diffractions in low symmetry crystal may be observed when the specimens are of modest thickness and dynamic diffraction occurs [4]. Sometimes it is possible to perform a tilting experiment to test if double diffraction is occurring.

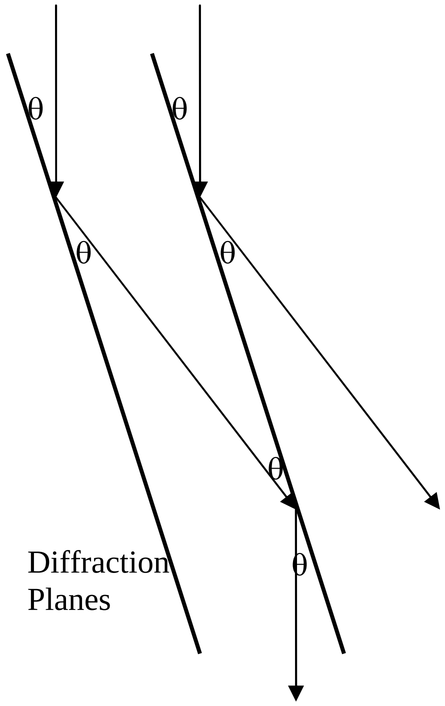

Figure 7-6 The electron beam can be diffracted more than once – a phenomenon called dynamical scattering

7.5.1 Indexing of Electron Diffraction Pattern

SAED patterns are sharply focused spot patterns. We will be talking about positions of diffraction spots and not their intensities for most of this thesis. The type of analysis differs from the X-ray studies, though much of the discussion of electron diffraction follows directly from the analysis of XRD. The reason that intensities of the spots are not measured is that the electron beams are diffracted more than one time in a typical TEM specimen [3, 4, 11]. We have discussed the major differences between the two radiation sources: electrons and X-rays in the previous chapter:

- Electrons have a much shorter wavelength than the X-rays (for laboratory research).

- Electrons are scattered more strongly because they interact with both the nucleus and the electrons of the scattering atoms through Coulomb forces.
- Electron beams can be easily directed because electrons are charged particles.

The indexing of single crystal diffraction patterns begins with the identification of the forward transmitted beam, followed by indexing two independent diffraction spots nearest the (000) spot. Once the indices of all diffraction spots are obtained, we can specify the zone axis – the normal to the plane of the spot pattern. The indexing of a diffraction pattern is not unique. A high symmetry leads to a multiplicity of different, but equally correct ways to index a pattern. The procedures are straightforward for low-index zone axes of simple crystal structures, but becoming increasingly difficult for crystal structures with low symmetry and for high-index zone axes, where many different combinations of interplanary spacings and angles provide diffractions patterns that look similar.

As we have mentioned in the previous chapter, indexing single crystal electron diffraction pattern requires that an approximation to the correct structure be known in advance.

7.5.2 Simulation of Electron Diffraction Pattern

In many cases, it is helpful to use a computer program to calculate the diffraction patterns, especially in the simple case where only kinematics are considered. Interpretation of diffraction data can be routine and relatively straightforward or extremely complex depending on the type of structures. In order to figure out the crystal structures of complex solids, such as $Li[Ni_xLi_{1/3-2x/3}Mn_{2/3-x/3}]O_2$ system, simulations of different structural models are compared with the experimentally obtained diffraction data. With Cerius^2 [12], fast and interactive simulation radically increases the efficiency of diffraction data interpretation. Simulated patterns can be recalculated instantaneously as a structural model is modified or manipulated, allowing real-time coupling of structure modeling to experiment. In addition, changing diffractometer properties, the nature of the radiation, and simulation parameters is straightforward with Cerius^2.

References:

1. J.M. Cowley, *Diffraction Physics*. 1995, Amsterdam; New York: Elsevier Science B.V.
2. B.D. Cullity, *Elements of X-ray Diffraction*. 2nd ed. 1978, Reading, Massachusetts: Addison-Wesley Pub. Co.
3. B. Fultz and J.M. Howe, *Transmission Electron Microscopy and Diffractometry of Materials*. 2nd ed. 2002, New York: Springer.
4. D.B. Williams and C.B. Carter, *Transmission Electron Microscopy: A Textbook for Materials Science*. Vol. V1-V4. 1996, New York: Plenum Press.
5. *International Tables for Crystallography*. Vol. C. 1983, D. Reidel Publishing Company.
6. H.A. Bethe, Ann. Phys. Lpz, 1928. **87**: p. 55-129.
7. J.M. Cowley and A.F. Moddie, Acta Crystallographica, 1957. **10**: p. 609-619.
8. A.F. Moddie, J.M. Cowley, and P. Goodman, in *International Tables for Crystallography*. 1990, D. Reidel Publishing Company. p. Section 5.2.
9. W.I.F. David, et al., *Structure Determination from Powder Diffraction Data*. 2002, Oxford University Press: New York.
10. H. Rietveld, Journal of Applied Crystallography, 1969. **2**: p. 65-71.
11. J.M. Cowley, ed. *Electron Diffraction Techniques*. Vol. 1. 1992, Oxford University Press: New York.
12. http://www.accelrys.com/cerius2/.

CHAPTER 8

UNDERSTANDING THE STRUCTURE OF $LINI_XLI_{1/3-2X/3}MN_{2/3-X/3}O_2$ BY ELECTRON DIFFRACTION EXPERIMENT AND POWDER DIFFRACTION SIMULATION

The three-dimensional crystal structure of the $LiNi_xLi_{1/3-2x/3}Mn_{2/3-x/3}O_2$ system is studied by various diffraction techniques. In such a multi- cation system, the degree of complicity in solving the structural details requires an approach combining both experimental and computation tools. Electron diffraction experiments and powder diffraction simulations (X-rays and neutron), together with first principles computation are applied to study the cationic arrangements of Li^+, Ni^{2+} and Mn^{4+} in $LiNi_xLi_{1/3-2x/3}Mn_{2/3-x/3}O_2$ ($0 \leq x \leq 1/2$). The focus is on $LiNi_{1/2}Mn_{1/2}O_2$ ($x = 1/2$) and Li_2MnO_3 ($x = 0$) since they represent the two end members of the solid solution $LiNi_xLi_{1/3-2x/3}Mn_{2/3-x/3}O_2$ ($0 \leq x \leq 1/2$), as illustrated in the ternary phase diagram in Figure 8-1. A compound with nominal composition $LiNi_{1/3}Li_{1/9}Mn_{5/9}O_2$ ($x = 1/3$) is also studied, this composition can be obtained by replacing 2/9 Li^+ and 1/9 Mn^{4+} with 1/3 Ni^{2+} in the transition metal layer of Li_2MnO_3 or replacing 1/6 Ni^{2+} with 1/9 Li^+ and 1/18 Mn^{4+} in the same layer of $LiNi_{1/2}Mn_{1/2}O_2$.

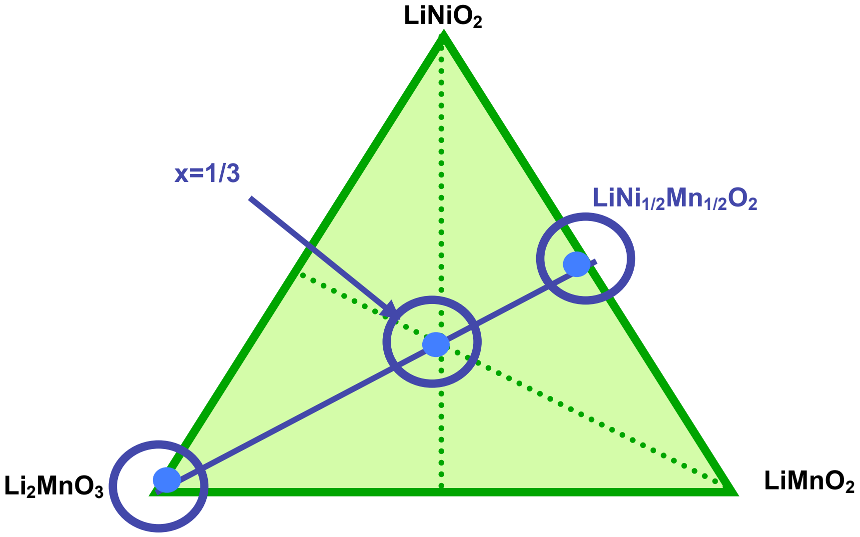

Figure 8-1 Ternary phase diagram of $LiNiO_2$-$LiMnO_2$-Li_2MnO_3. The solid line inside the triangle represents the solid solution $LiNi_xLi_{1/3-2x/3}Mn_{2/3-x/3}O_2$ ($0 \le x \le 1/2$)

8.1 Synthesis and XRD Characterization

$LiNi_{1/2}Mn_{1/2}O_2$ and $LiLi_{1/9}Ni_{1/3}Mn_{5/9}O_2$ samples were synthesized from stoichiometric quantities of co-precipitated manganese and nickel hydroxides with lithium hydroxide at 900°C - 1000°C in O_2. Li_2MnO_3 sample was synthesized by conventional solid-state reaction method with stoichiometric amount of Li_2CO_3 and $MnCO_3$ fired at 850°C in O_2.

The X-ray diffraction spectra of $LiNi_{1/2}Mn_{1/2}O_2$ ($x = 1/2$) and $LiNi_{1/3}Li_{1/9}Mn_{5/9}O_2$ ($x = 1/3$) are shown in Figure 8-2 a) & b). Both spectra can be indexed by the typical rhombohedral layered structure with space group R3-m, while additional superstructure peaks can be seen in the two-theta range of 20-30°.

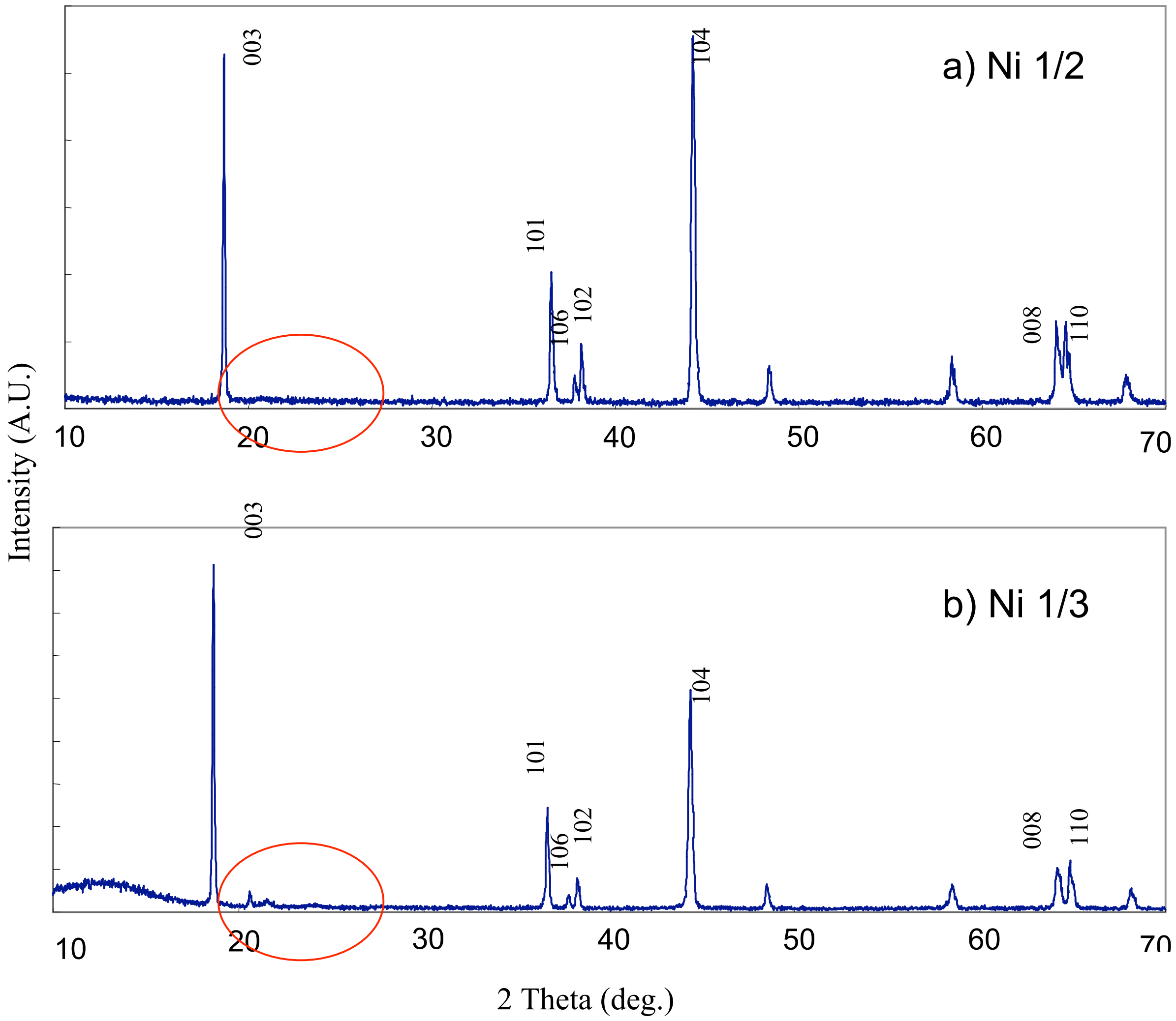

Figure 8-2 X-ray powder diffraction spectra of a) $LiNi_{1/2}Mn_{1/2}O_2$ and b) $LiNi_{1/3}Li_{1/9}Mn_{5/9}O_2$, notice that the superstructure peaks become stronger when Ni content decreases.

The (104)/(003) integrated peak intensity ratios for $LiNi_{1/2}Mn_{1/2}O_2$ was found as 0.98, significantly higher than 0.71 for an ideal layered structure (no mixing of transition metal layer in the Li layers and Li in the transition metal layer). The intensity ratio is an indication of the amount of transition metal and Li swapped between the transition metal layer and the Li layer, though X-ray diffraction is incapable of distinguishing whether Ni or Mn is present in the Li layer. There is about 9% (approximately 1/12) of cation mixing, and it has been confirmed by neutron diffraction study [1] that the transition metal present in the Li layer is Ni;

thus the composition in the transition metal layer for $LiNi_{1/2}Mn_{1/2}O_2$ can be written as $Li_{0.09}Ni_{0.41}Mn_{0.50}$

It is found that by adding more lithium in the transition metal layer, i.e. when the nickel content is less, the cation mixing between the transition metal ion and Li^+ is reduced. Only a negligible amount of cation mixing is found between Ni^{2+} in the Li layer and Li^+ in the transition metal layer, which is seen by the reduced (104)/(003) peak intensity ratio in the XRD spectrum of $LiNi_{1/3}Li_{1/9}Mn_{5/9}O_2$ in Figure 8-2 b).

Experimental and simulated X-ray powder diffraction patterns of Li_2MnO_3 are compared, as shown in Figure 8-3a) and b) respectively. Notice that the experimentally observed superstructure peak shapes and intensities (two-theta 20-30° range) cannot be exactly matched by the simulated XRD spectrum of Li_2MnO_3. The simulated XRD powder diffraction is obtained from the structure with space group C2/m, based upon the structure in the literature [2]. The superstructure peaks in the experimental spectra appear at the same two-theta position, but with different peak shape and intensity. For example, the peak intensities of $(200)_{C2/m}$ is higher than that of $(110)_{C2/m}$ in the experimental spectra; while the reverse is true in the simulated XRD spectra. One may argue that this is due to the disorder of Li^+ and Mn^{4+} on α and β sites respectively, since the synthesis was carried out at 850°C. Nevertheless, it has been confirmed by the NMR study that there is little evidence of Li/Mn mixing in the $Li_{1/3}Mn_{2/3}$ layer [3]. The discrepancy between the experimental and simulated XRD spectra can be successfully explained by the stacking disorder that is present along the $c_{hex.}$ axis in the powder Li_2MnO_3 sample, which will be explained in detail in the next chapter.

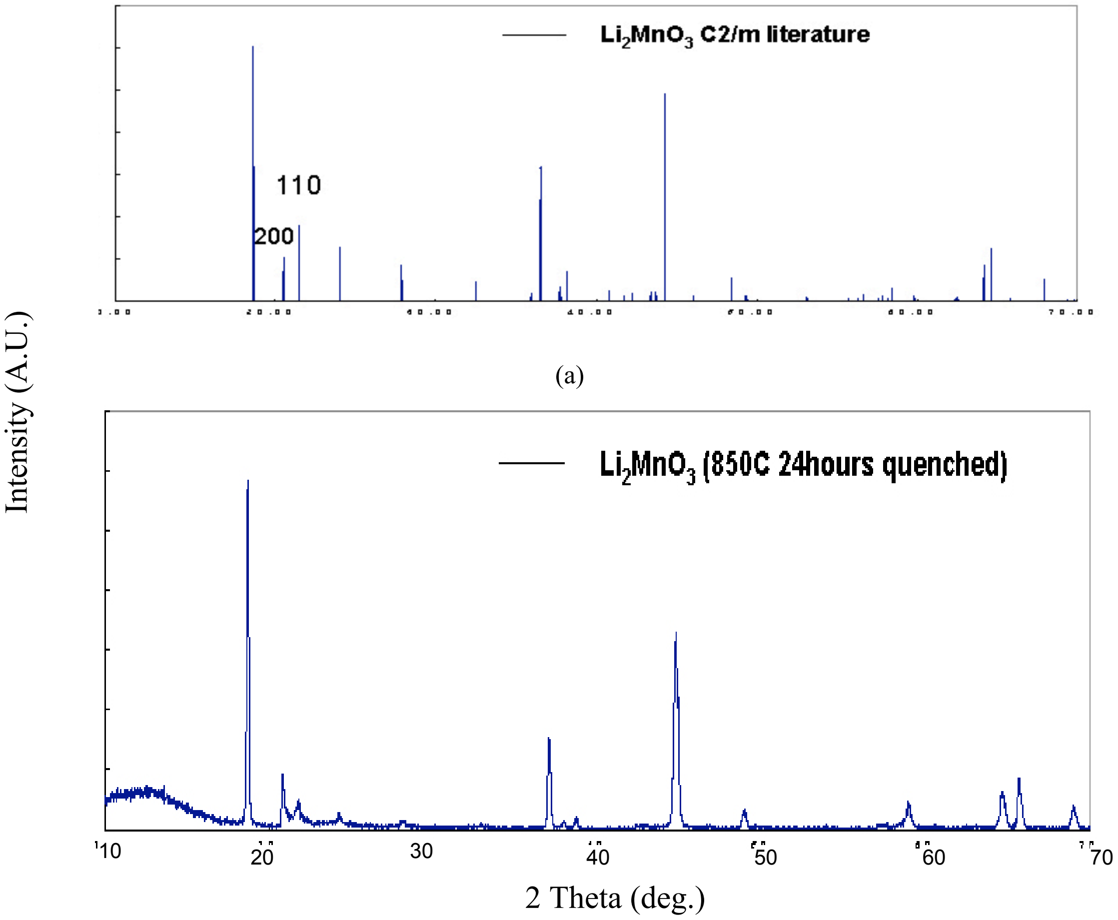

(b)

Figure 8-3 a) Simulated and b) Experimental X-ray powder diffraction spectra of Li_2MnO_3.

The fact that there are similar superstructure peaks in the two-theta range of 20-30º in the XRD spectra of $LiNi_{1/2}Mn_{1/2}O_2$ (x = 1/2), $LiNi_{1/3}Li_{1/9}Mn_{5/9}O_2$ (x = 1/3) and Li_2MnO_3 (x = 0) has led to the speculation that a distinct Li_2MnO_3 phase is present in $LiNi_xLi_{1/3-2x/3}Mn_{2/3-x/3}O_2$ (when $x \neq 0$) [4-6]. However, previous powder XRD diffraction and electrochemistry study have demonstrated that solid solution exists throughout the composition range and that there are no local regions of Li_2MnO_3 in either $LiNi_{1/2}Mn_{1/2}O_2$ [7, 8] or $LiNi_{1/3}Li_{1/9}Mn_{5/9}O_2$ [7].

8.2 Long-Range Cation Ordering in $LiNi_xLi_{1/3-2x/3}Mn_{2/3-x/3}O_2$ ($0 \leq x \leq 1/2$)

8.2.1 Electron Diffraction Analysis on $LiNi_{1/2}Mn_{1/2}O_2$

Electron diffraction patterns and transmission electron microscope (TEM) images were collected from the $LiNi_{0.5}Mn_{0.5}O_2$ powder sample, which was suspended on a copper grid with lacey carbon under an accelerating voltage of 200 keV on a JEOL 200CX, JEOL 2000FX or JEOL 2010 microscope. Chemical analyses of Ni and Mn contents of individual $LiNi_{0.5}Mn_{0.5}O_2$ crystals were performed by X-ray energy dispersive spectroscopy (EDS) at a sample tilt angle of +15° (tilted towards the X-ray detector) on the JEOL 2010 microscope. Examination of ten randomly selected single crystals revealed an average composition of $LiMn_{0.51}Ni_{0.49}O_2$, which agrees with the nominal composition within experimental uncertainty. Lithium and oxygen contents were not quantified by EDS and were assumed stoichiometric.

A total of 34 electron diffraction patterns were collected randomly from the $LiNi_{1/2}Mn_{1/2}O_2$ sample. Among those patterns, 17 revealed superstructure reflections in addition to the fundamental reflections of the hexagonal parent structure with trigonal symmetry R3-m. Figure 8-4 (a), (b) & (c) are electron diffraction patterns obtained from $LiNi_{1/2}Mn_{1/2}O_2$ ($x = 1/2$) with fundamental reflections indexed to the parent hexagonal cell with the hexagonal cell dimensions $a = 2.893$Å and $c = 14.305$Å, which is obtained from lattice refinement of the XRD data. Figure 8-4 (a), (b) & (c) respectively shows the $[-411]_{hex}$ $[-2\ 5\ -1]_{hex}$ and $[-111]_{hex}$ zone axis patterns. The most predominant feature of the electron diffraction patterns is that only the $(11\boldsymbol{l})_{hex.}$ planar spacings ($\boldsymbol{l} = 3n$, $n = 0, \pm1, \pm2\ldots$) in the parent hexagonal structure are tripled by the presence of the superstructure reflections. The presence of these unique superstructure reflections suggests that the formation of a $\sqrt{3}a_{hex} \times \sqrt{3}a_{hex} \times c_{hex}$ superstructure, which implies long-range ordering of Li, Ni and Mn in the transition metal layer.

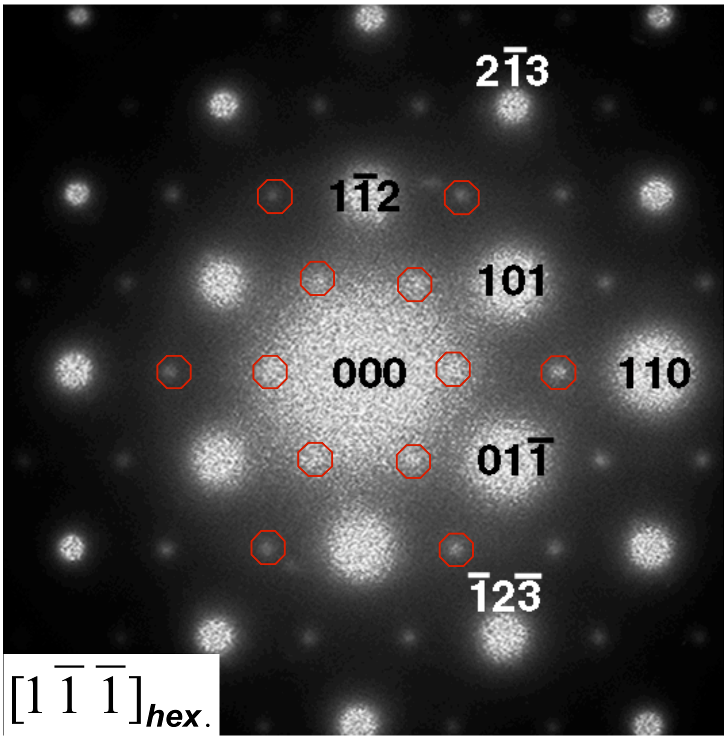

(a)

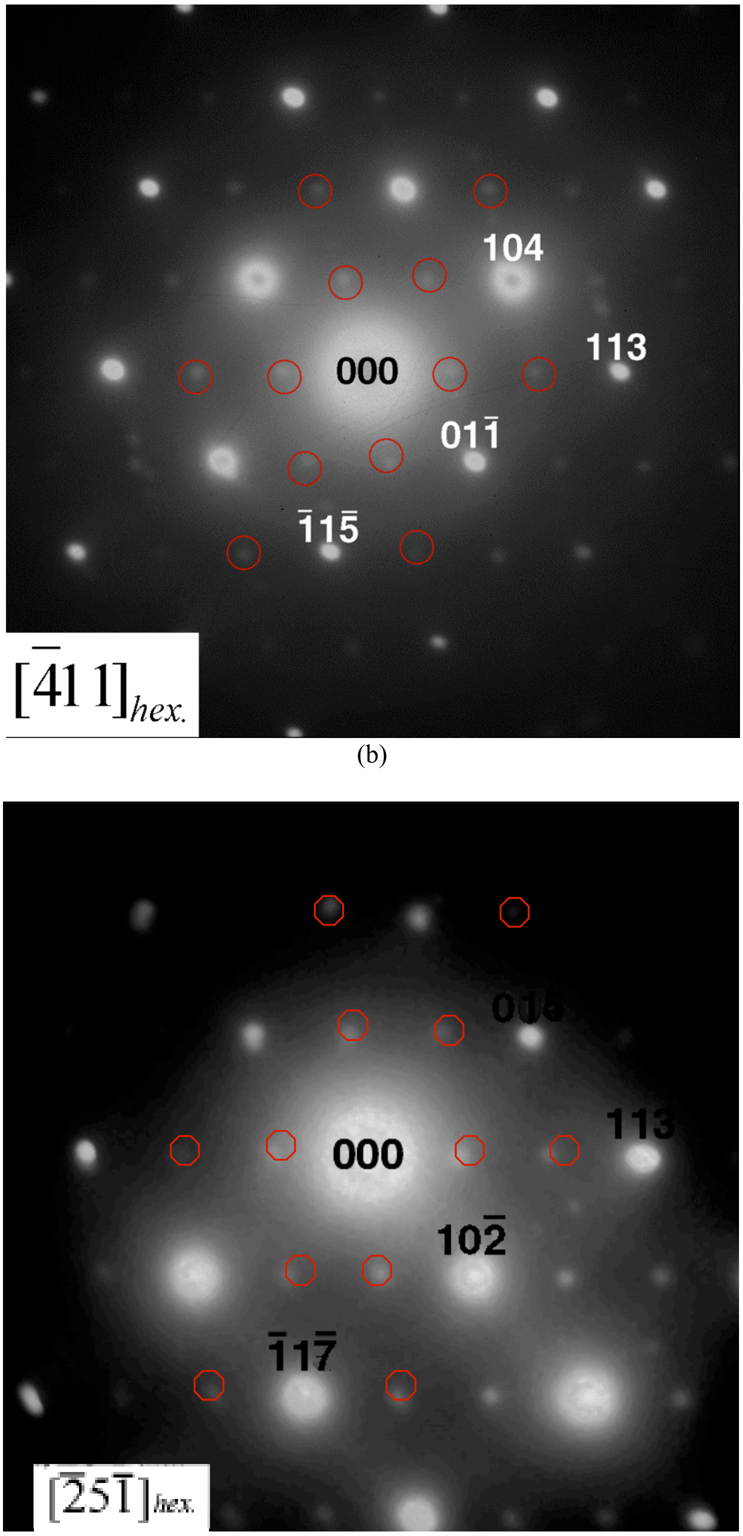

(b)

(c)

Figure 8-4 (a) $[1\text{-}1\text{-}1]_{hex.}$ (b) $[\text{-}411]_{hex.}$ (c) $[\text{-}25\text{-}1]_{hex.}$ electron diffraction patterns of $LiNi_{1/2}Mn_{1/2}O_2$, which shows the superstructure reflections consistent with $\sqrt{3}a_{hex} \times \sqrt{3}a_{hex.} \times c_{hex.}$ superstructure with space group $P3_112$.

8.2.2 Proposed Structure Model

In-Plane Ordering and Stacking of Ordered Planes

Ordering in a √3 × √3 superstructure cell (Figure 8-5) is common on triangular lattices, and has been observed for Li-vacancy ordering in delithiated $LiCoO_2$ [9, 10] and delithiated $LiNiO_2$ [11] at lithium concentration 1/3. This superstructure creates two distinct sites (α and β) in the transition metal layer with a multiplicity of 1 to 2. The a-b plane of the unit cell can be defined in the hexagonal cell (Figure 8-5a) or in the monoclinic cell (Figure 8-5b) depending on the stacking of the ab planes along the c-axis. As the translational unit in the transition metal layer is enlarged by the superstructure formation, different ways of positioning successive transition metal layers along the c-axis results in different crystal structures.

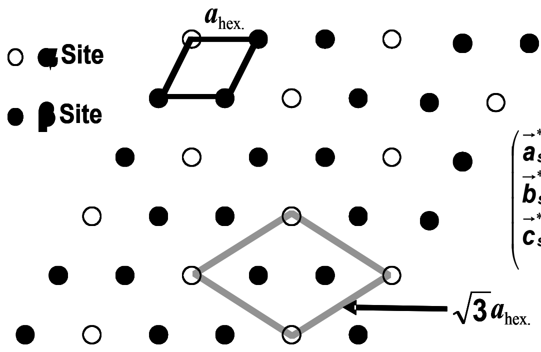

$$\begin{pmatrix}\vec{a}^*_{superhex.}\\ \vec{b}^*_{superhex.}\\ \vec{c}^*_{superhex.}\end{pmatrix} = \begin{pmatrix}1/3 & 1/3 & 0\\ -1/3 & 2/3 & 0\\ 0 & 0 & 1\end{pmatrix}\begin{pmatrix}\vec{a}^*_{hex.}\\ \vec{b}^*_{hex.}\\ \vec{c}^*_{hex.}\end{pmatrix}$$

$$\left(\vec{a}_{superhex.}, \vec{b}_{superhex.}, \vec{c}_{superhex.}\right) = \left(\vec{a}_{hex}, \vec{b}_{hex}, \vec{c}_{hex}\right)\begin{pmatrix}2 & -1 & 0\\ 1 & 1 & 0\\ 0 & 0 & 1\end{pmatrix}$$

(a)

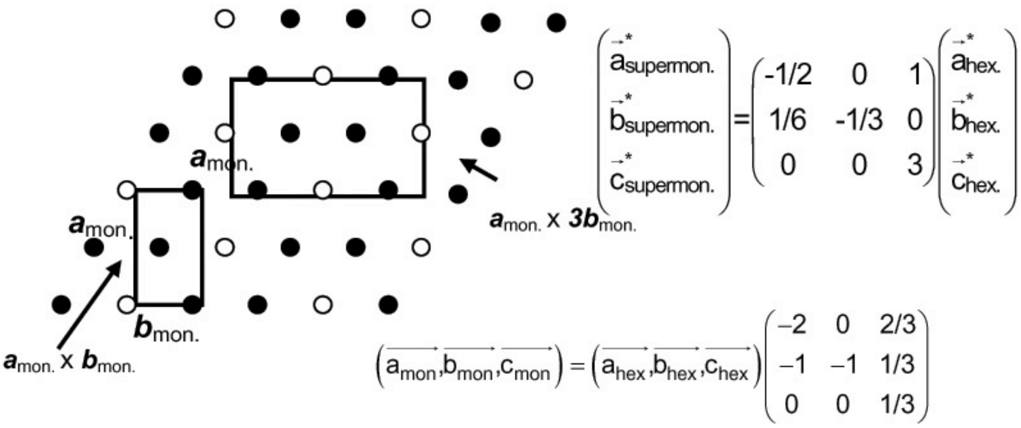

$$\begin{pmatrix} \vec{a}^*_{\text{supermon.}} \\ \vec{b}^*_{\text{supermon.}} \\ \vec{c}^*_{\text{supermon.}} \end{pmatrix} = \begin{pmatrix} -1/2 & 0 & 1 \\ 1/6 & -1/3 & 0 \\ 0 & 0 & 3 \end{pmatrix} \begin{pmatrix} \vec{a}^*_{\text{hex.}} \\ \vec{b}^*_{\text{hex.}} \\ \vec{c}^*_{\text{hex.}} \end{pmatrix}$$

$$\left(\overrightarrow{a_{mon}}, \overrightarrow{b_{mon}}, \overrightarrow{c_{mon}}\right) = \left(\overrightarrow{a_{hex}}, \overrightarrow{b_{hex}}, \overrightarrow{c_{hex}}\right) \begin{pmatrix} -2 & 0 & 2/3 \\ -1 & -1 & 1/3 \\ 0 & 0 & 1/3 \end{pmatrix}$$

(b)

Figure 8-5 a-b plane on a) hexagonal setting and b) monoclinic setting of √3 × √3 superstructure cell on triangular lattices and their relations with parent hexagonal/monoclinic cell.

The *a1b2c1* stacking of the ordered transition metal layers in Figure 8-6a) creates a superstructure with $P3_112$ symmetry, which consists of three transition metal layers per unit cell. Projection of three successive transition metal layers along the c-axis, as shown in Figure 8-6b, illustrates that the structure has a 3-fold screw-axis. On the other hand, the stacking shown in Figure 8-7a) (*a1c1* stacking) leads to C2/m symmetry and is equivalent to the unit cell of Li_2MnO_3. In Li_2MnO_3 layers of pure Li alternate with layers of composition $Li_{1/3}Mn_{2/3}$ in which Li and Mn ions are ordered in the $\sqrt{3}a_{hex.} \times \sqrt{3}a_{hex.}$ superstructure and the unit cell is re-defined as shown in Figure 8-5b) [2]. Projection of two successive transition metal layers of Li_2MnO_3 shows that the structure has no 3-fold screw axis but a 2-fold axis and a in-plane mirror plane (2/m) in Figure 8-7b).

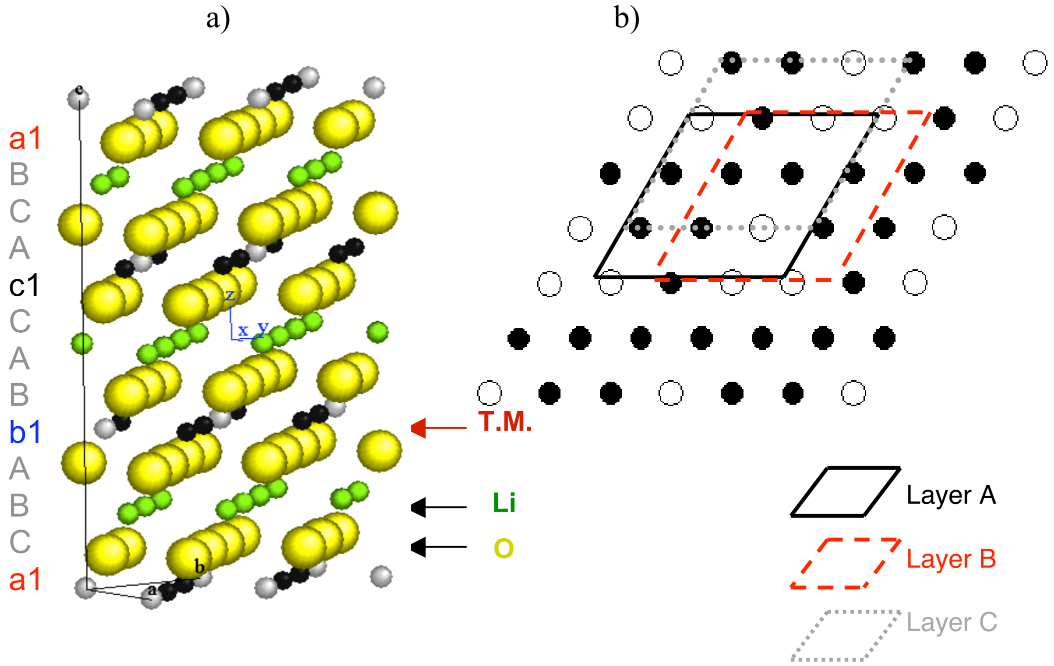

Figure 8-6 a) Proposed structure of $LiNi_{1/2}Mn_{1/2}O_2$ with $P3_112$ space group. b) $[001]_{hex.}$ projection of three successive transition metal layers.

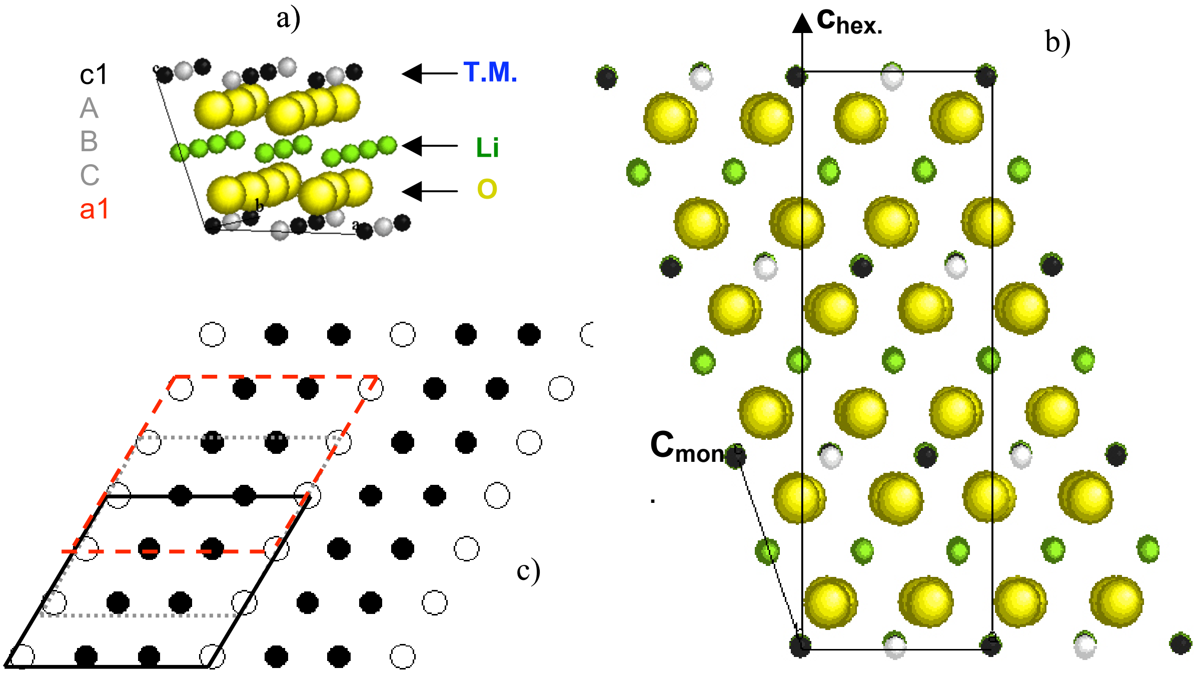

Figure 8-7 a) Crystal structure of Li_2MnO_3 with C2/m space group, b) $[001]_{hex.}$ projection of three successive transition metal layers and c) projection of the cell along $[010]_{hex.}$ showing the relation between $c_{mon.}$ and $c_{hex.}$

Careful comparison of the TEM patterns with electron diffraction simulations of these two possible stackings of the transition metal layers indicates that $LiNi_{1/2}Mn_{1/2}O_2$ has three transition metal layers per unit cell with space group $P3_112$. For example, tripling of the $(113)_{hex.}$ type fundamental reflections in Figure 8-4b) is consistent with the $\sqrt{3}a_{hex.} \times \sqrt{3}a_{hex.} \times c_{hex.}$ superstructure with space group $P3_112$: these superstructure reflections are absent in the simulated electron diffraction pattern of $LiNi_{1/2}Mn_{1/2}O_2$ with space group C2/m along the equivalent zone axis. Hence while $LiNi_{1/2}Mn_{1/2}O_2$ has the same in-plane ordering as Li_2MnO_3, it has a distinctively different ordering along the c-axis. If the transition metal layers were disordered, as speculated previously[8], both stacking sequences (C2/m and $P3_112$) would be identical and degenerate to the R-3m structure as a result of the lack of translational symmetry breaking in the transition metal layer.

It is not possible to directly determine the occupancies of α and β sublattices from the TEM experiments. In order to generate a model with which to simulate the TEM patterns, 9% Ni occupancy in the lithium layer and a composition of $Li_{0.09}Ni_{0.41}Mn_{0.50}$ in the transition metal layer was assumed. Small variations in the Ni occupancy value (8-10%) do not affect the conclusions of this structural model. Given this composition, one cannot create a stoichiometric occupation of α and β sites in the transition metal layer. However, this does not preclude long-range ordering, which is quite common even with partial occupancies [12]. Given the charge difference between Li^+ and Mn^{4+}, one expects a strong ordering tendency between these ions. Experimental XRD evidence for the ordering interaction between Li^+ and Mn^{4+} can be found in the well-ordered nature of Li_2MnO_3, and in the Li NMR observations for this material, which showed a much higher probability for Li^+ ions to be surrounded with 6 Mn^{4+} ions than that would be found for a random solution. The maximum number of the nearest neighbor Li^+ – Mn^{4+} contacts can be achieved by segregating them to separate sublattices (Li to α, and Mn to β). In addition, first principles studies have shown that there is a strong tendency for Ni^{2+} and Mn^{4+} to order [13], the maximum ordering between Ni and Mn occurs when Ni^{2+} preferentially occupies α site. Hence, a likely model for the occupancies in the $\sqrt{3}a_{hex.} \times \sqrt{3}\,a_{hex}$ structure with in-plane composition $Li_{0.09}Ni_{0.41}Mn_{0.50}$ is [α (0.27Li; 0.73Ni), β (0.75Mn; 0.25Ni)].

8.2.3 X-ray and Neutron Powder Diffraction Simulation of $LiNi_{1/2}Mn_{1/2}O_2$

To understand why ordering in $LiNi_{1/2}Mn_{1/2}O_2$ may have been missed with XRD and neutron diffraction methods, we examine the superlattice peak intensities in simulated powder XRD and neutron diffraction patterns using $Cerius^{2}$. The calculated powder XRD pattern of the $\sqrt{3}a_{hex.} \times \sqrt{3}a_{hex.} \times c_{hex.}$ superstructure with site occupancies α (0.27Li; 0.73Ni) and β (0.75Mn; 0.25Ni) is shown in Figure 8-8. Lithium layers in the simulated superstructure consist only of Li, as it can be shown that the random distribution by Ni (8-10%) in the lithium layers has a negligible effect on the superstructure reflection intensity. The superstructure peak intensities are less than 1% of the intensity of the fundamental $(003)_{hex.}$ peak, making them very difficult to resolve experimentally. The low superstructure peak intensities result from similar average scattering factors for X-rays on α (0.27Li; 0.73Ni) and β (0.75Mn; 0.25Ni) sites. It should also be pointed out that simulated powder XRD diffraction patterns of superstructures with the *a1b2c1* and the *a1c1* stacking of the ordered transition metal layers are nearly identical, especially at low two-theta angles, which demonstrates the ambiguous nature of structural determination by powder diffraction techniques.

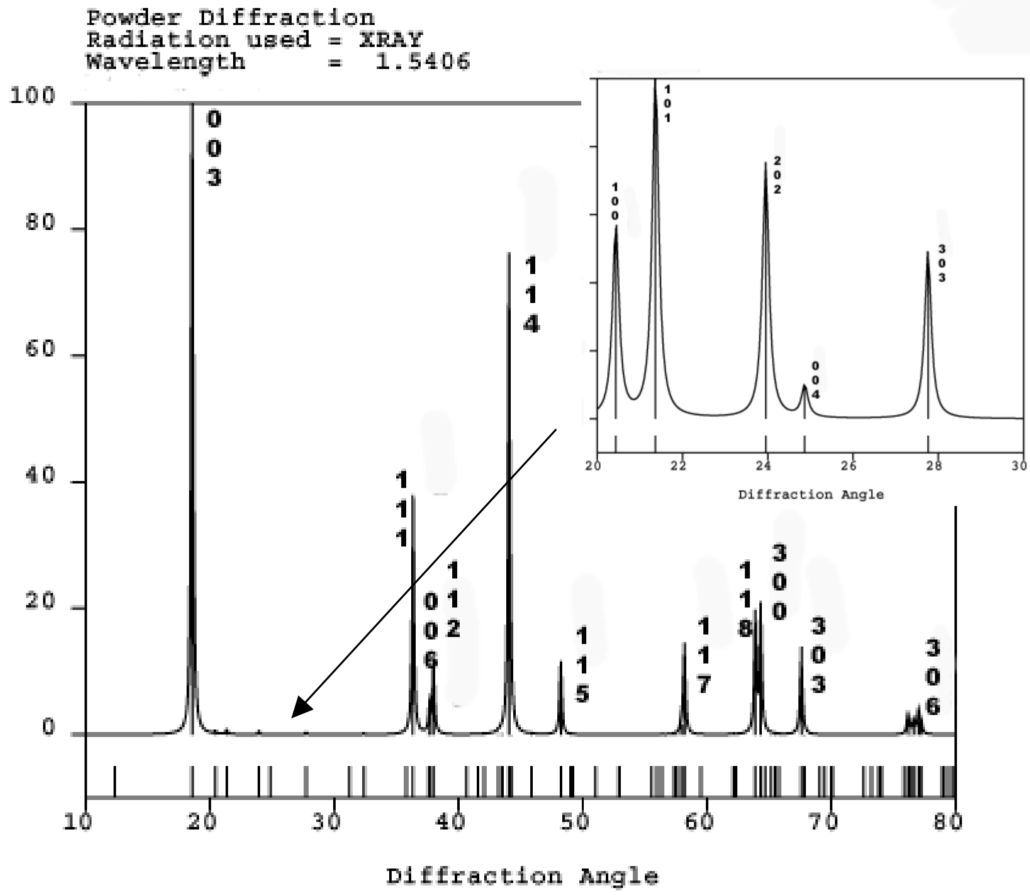

Figure 8-8 Calculated powder XRD spectrum of $LiNi_{1/2}Mn_{1/2}O_2$ with the proposed structure (λ = 1.5406Å). Note that the superstructure peak intensities in the range of 20-30° (see insert) are less than 1% of the maximum fundamental reflection peak intensity $(003)_{hex}$.

For the site occupancies α (0.27Li; 0.73Ni) and β (0.75Mn; 0.25Ni), one might expect to see relatively strong superstructure peaks in the powder neutron diffraction pattern of the $\sqrt{3}a_{hex.} \times \sqrt{3}a_{hex.} \times c_{hex.}$ superstructure as Ni and Mn have significantly different neutron scattering lengths (b_{Ni} = 10.30fm; b_{Mn} = -3.73fm) [14]. However, it is important to note that the neutron scattering length of Li, b_{Li}, is -1.90fm [14] and Li occupancy on the Ni-rich α site significantly lowers the contrast between α and β in powder neutron diffraction patterns. In fact, in the simulated powder neutron diffraction pattern of the superstructure with α (0.27Li; 0.73Ni) and β (0.75Mn; 0.25Ni) in Figure 8-9a) the superstructure reflection peak intensities are only a few percent of the maximum fundamental reflection peak intensities. Small partial occupancies of Mn on α and Ni on β, further lowers the superstructure reflections peak intensities in powder neutron diffraction. For instance, if 4% Mn and Ni interchange sites, making the occupancy on α [0.27Li; 0.61Ni; 0.12Mn] and β [0.69Mn; 0.31Ni], the intensities of superstructure reflections fall to less than 2% of the maximum fundamental peak intensity, as shown in Figure 8-9b). As typical $LiNi_{1/2}Mn_{1/2}O_2$ samples are synthesized at high temperatures, such disorder is likely, making ordering difficult to detect even by neutron diffraction. We therefore believe that the previous conclusion that ordering in $LiNi_{1/2}Mn_{1/2}O_2$ is unlikely [1, 7] based on powder XRD and neutron diffraction data alone shall be revisited. We have shown here that even for the maximum long-range ordering of Ni and Mn possible, neutron superstructure peaks only appear with very small intensities.

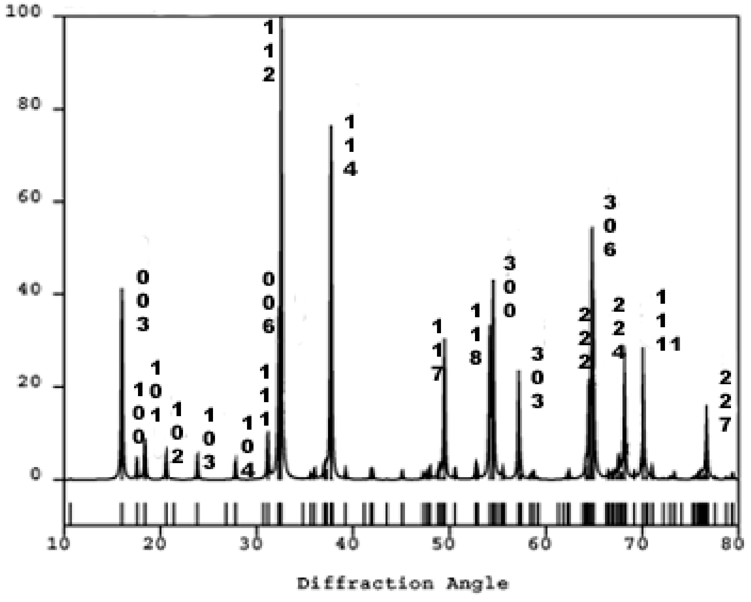

(a)

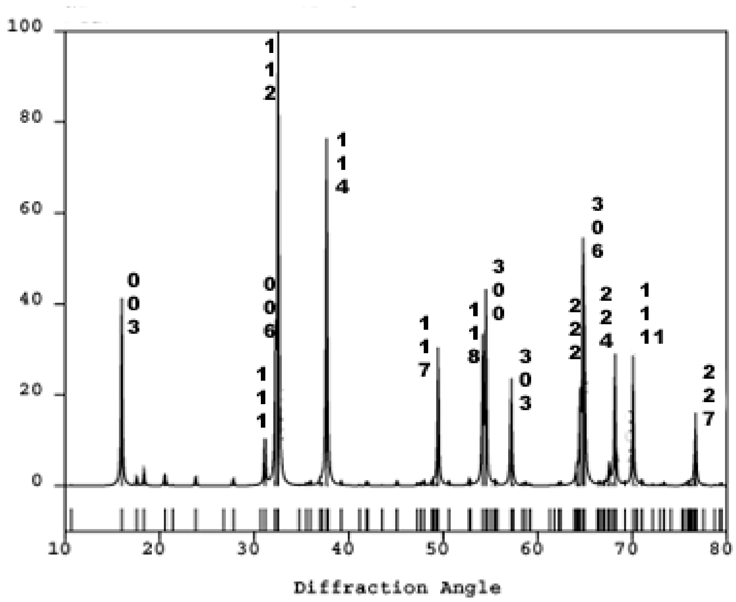

(b)

Figure 8-9 Calculated powder neutron diffraction spectra of proposed superstructures (λ = 1.3230Å) with (a) α [0.27Li; 0.73Ni] and β [0.75Mn; 0.25Ni]; (b)α [0.27Li; 0.61Ni; 0.12Mn] and β [0.69Mn; 0.31Ni]

8.2.4 Electron Diffraction Analysis on $LiNi_{1/3}Li_{1/9}Mn_{5/9}O_2$ and Li_2MnO_3

Electron diffraction study on $LiNi_{1/3}Li_{1/9}Mn_{5/9}O_2$ (x = 1/3) reveals the presence of the same type of long-range ordering in the transition metal plane in all samples, that is $\sqrt{3}a_{hex} \times \sqrt{3}a_{hex}$. Figure 8-10a) & b), are electron diffraction patterns obtained from $LiNi_{1/3}Li_{1/9}Mn_{5/9}O_2$ (x = 1/3), with fundamental reflections indexed to the parent hexagonal cell. The most predominant feature of the electron diffraction patterns obtained from both samples, is that only the $(11\boldsymbol{l})_{hex.}$ planar spacings ($\boldsymbol{l}$ = 3n, n = 0, ±1, ±2…) in the parent hexagonal structure are tripled by the presence of the superstructure reflections.

In $LiNi_{1/3}Li_{1/9}Mn_{5/9}O_2$ (x = 1/3) sample, the long range ordering is more predominant, shown by the presence of such superstructure reflections in every crystal that had been studied by electron diffraction. (A total of 15 crystals) Figure 8-10a) & b) presents diffraction patterns of $[001]_{hex}$ and $[21\text{-}2]_{hex}$ zone axes. Both patterns are obtained from the same crystal by titling the crystal and can be indexed with the superstructure described above. In electron diffraction, what is observed in the diffraction patterns are obtained as near-planar section through k-space. Since the Ewald sphere is nearly flat, the approximation that a diffraction pattern is just a picture of a plane in the reciprocal lattice is valid most of time. Thus to regain the three-dimensional information of the crystal structure, different zone axes patterns obtained by tilting the same crystal help to identify the three-dimensional crystal structure in the structure analysis. The fact that the same type of superstructure reflections are seen in both diffraction patterns in Figure 8-10 eliminates the possibility of additional reflection spots due to double diffraction in electron diffraction. In $LiNi_{1/3}Li_{1/9}Mn_{5/9}O_2$ the composition of the transition metal layer can be written as $Li_{1/9}Ni_{1/3}Mn_{5/9}$, since the cation mixing between the Ni in the transition layer and the Li in the Li layer is negligible. To achieve the maximum separation of Li and Mn on α and β, at the same time the maximum ordering between Ni and Mn, the occupancies of [α (0.33Li; 0.67Ni), β (0.84Mn; 0.16Ni)] is likely in the $\sqrt{3}a_{hex.} \times \sqrt{3}a_{hex}$ lattice. Such occupancies result in higher superstructure peak intensities in powder XRD experiment since the x-ray scattering contrast of α and β is higher compared to those of $LiNi_{1/2}Mn_{1/2}O_2$.

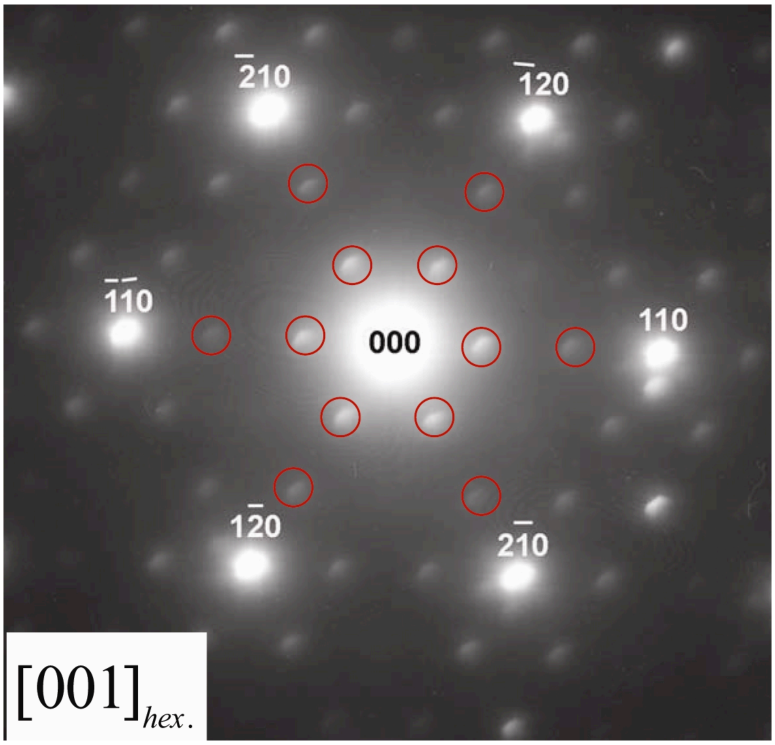

(a)

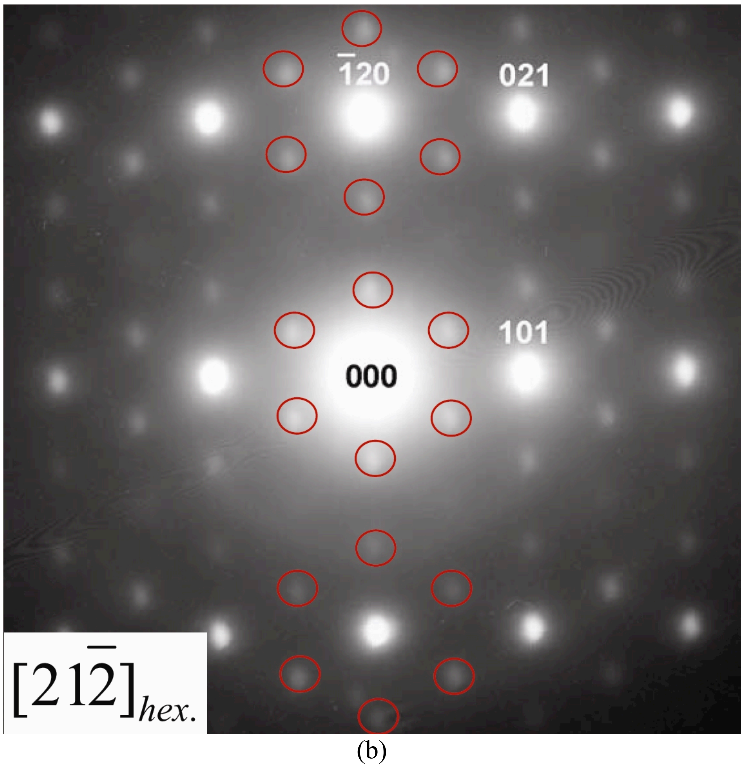

(b)

Figure 8-10 a) $[001]_{hex.}$ b) $[21\text{-}2]_{hex.}$ electron diffraction patterns of $LiNi_{1/3}Li_{1/9}Mn_{5/9}O_2$, which shows the superstructure reflections consistent with $\sqrt{3}a_{hex} \times \sqrt{3}a_{hex.} \times c_{hex.}$ superstructure with space group $P3_112$.

.

Perfect single crystal Li_2MnO_3 has the same type of $\sqrt{3}a_{hex} \times \sqrt{3}a_{hex}$ in-plane ordering in the $Li_{1/3}Mn_{2/3}$ layer due to strong ordering between Li^+ and Mn^{4+}. The ordered planes are stacked along the *c* axis with stacking sequence of *a1c1*, which results in a monoclinic primitive cell with space group C2/m, as illustrated in Figure 8-7a) The relationship between the primitive cell and conventional hexagonal cell is shown in Figure 8-7c). The structure has been confirmed by single crystal structure refinement [2] and powder XRD refinement of Li_2MnO_3 [15].

In our samples, we observed the same type of in-plane cation ordering but different stacking sequences of the ordered planes from what was experimentally observed in single crystal Li_2MnO_3. Among all the electron diffraction patterns obtained from 16 Li_2MnO_3 single crystals, majority of them can be indexed by the same structure model with space group $P3_112$, as shown by the example in Figure 8-11a). However, there are diffracted patterns that can be indexed with neither of the two structures ($P3_112$ or C2/m). Additional superstructure reflections are present other than $P3_112$ and C2/m, such as the diffraction pattern from zone axis $[001]_{hex.}$ in Figure 8-11b). The presence of additional superstructure reflections, as indicated by arrows, implies that more complicated stacking sequence could be present in that particular crystal. Additional superstructure reflections could also be present due to double diffraction, an effect common in electron diffraction experiment [16]. It is suspected that the exact structure of Li_2MnO_3 depends on the synthesis conditions.

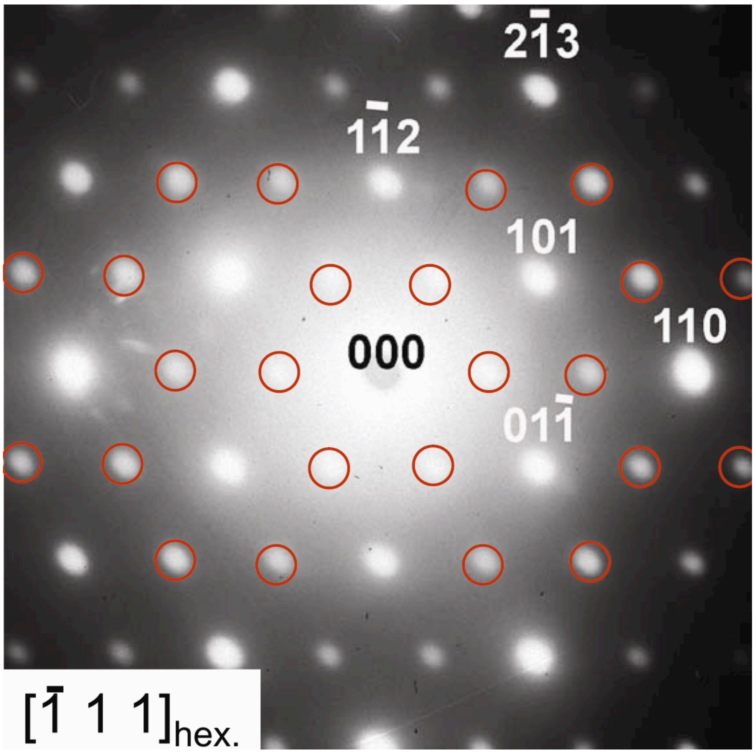

(a)

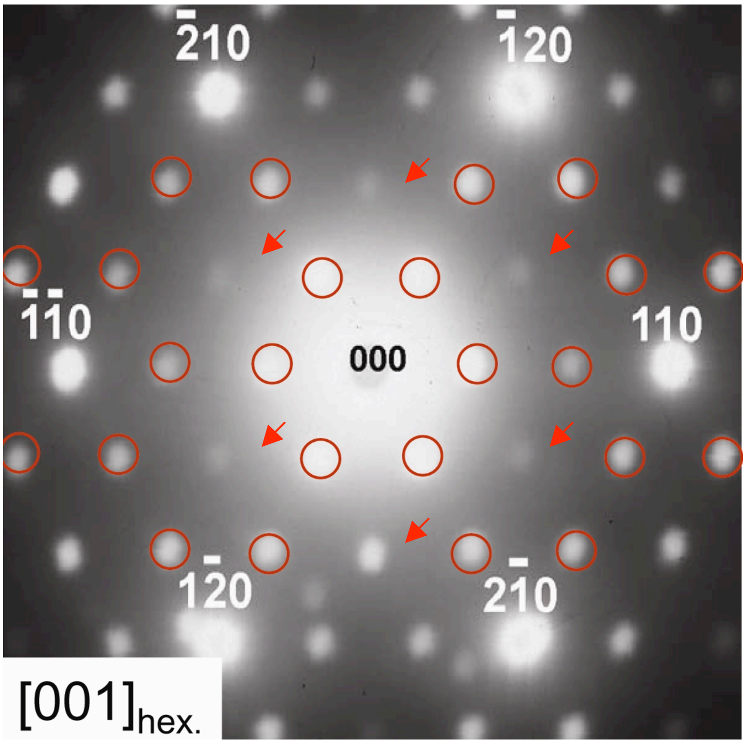

(b)

Figure 8-11 a) $[-111]_{hex.}$ b) $[001]_{hex.}$ electron diffraction patterns of Li_2MnO_3. Notices in b) there are extra reflections (indicated by arrows) that cannot be indexed with superstructure $P3_112$.

The intensities of the superlattice spots also increase when more lithium (less Ni content) is present in the transition metal layer, indicating that the in-plane ordering is more pronounced in lithium-rich compounds, which is consistent with the literature data [1, 17]. The contrast between the two distinct sites in the transition metal layer is provided by more Li occupying α sites and more Mn occupying β sites when x decreases, as shown in Table 8-I.

Table 8-I Site occupancies in $LiNi_xLi_{1/3-2x/3}Mn_{2/3-x/3}O_2$ ($0 \leq x \leq 1/2$)

	$LiNi_{1/2}Mn_{1/2}O_2$	**$LiNi_{1/3}Li_{1/9}Mn_{5/9}O_2$**	**Li_2MnO_3**
Transition Metal Layer	$Li_{0.09}Ni_{0.41}Mn_{0.50}$	$Li_{0.11}Ni_{0.33}Mn_{0.55}$	$Li_{0.33}Mn_{0.66}$
f_{Li}	1/12	1/9	1/3
Occupancies α : β = 1 : 2	α (0.27Li; 0.73Ni) β (0.75Mn; 0.25Ni)	α (0.33Li; 0.67Ni) β (0.84Mn; 0.16Ni)	α (1.00 Li), β (1.00 Mn)

8.3 Disorder in $LiNi_xLi_{1/3-2x/3}Mn_{2/3-x/3}O_2$ ($0 \leq x \leq 1/2$)

In the $LiNi_{1/2}Mn_{1/2}O_2$ sample, only about 50% of the crystals observed showed superstructure reflections, this implies the crystals are not perfectly long range ordered. The in-plane disorder lowers the contrast between α and β sites, and results in broadening (streaking) of superstructure reflections in XRD (ED)[18]. However, even if there is perfect in-plane (a-b plane) ordering, the stacking disorder along the c_{hex} axis could lead to the same phenomenon, in the extreme case - disappearance of the superstructure peaks in diffraction patterns may occur.

8.3.1 In-plane Disorder in $LiNi_{1/2}Mn_{1/2}O_2$

We have shown that the in-plane ordering in $LiNi_{1/2}Mn_{1/2}O_2$ is imperfect, and a small amount of site mixing between the Ni & Mn makes the in-plane ordering difficult to be detected by neutron diffraction. Figure 8-12a) is an electron diffraction pattern obtained from $[1\ \text{-}1\ 0]_{hex.}$ zone axis, the streaking perpendicular to the (110) plane normal reveals that the sizes or ordered domains in the transition metal layers are small. It is believed that multiple ordered domains grown from different LiMn6 nuclei can coexist in individual crystals of the $LiNi_{1/2}Mn_{1/2}O_2$ sample as shown in Figure 8-12b).

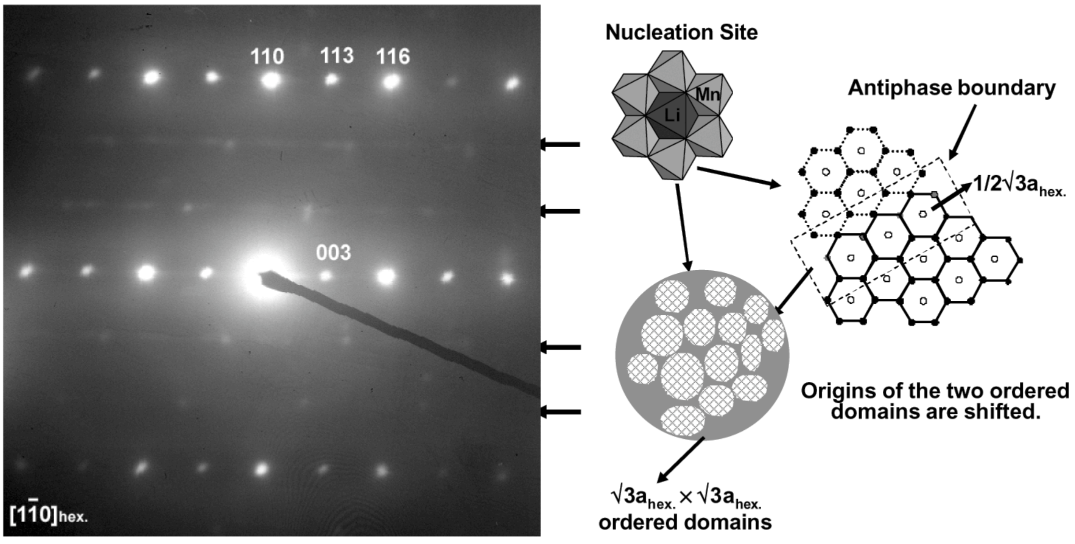

(a) (b)

Figure 8-12 a) An electron diffraction pattern along the $[1\text{-}10]_{hex.}$ zone axis collected from the '$Li[Ni_{1/2}Mn_{1/2}]O_2$' sample. The streaking perpendicular to the (110) plane normal reveals that the sizes of ordered domains in the transition metal layers are small. b) A microstructure that consists of multiple $\sqrt{3}a_{hex.} \times \sqrt{3}a_{hex.}$ ordered domains grown from different $LiMn_6$ nuclei is proposed.

The simplest type superstructure that will give this kind of reflections is so-called $\sqrt{3}a_{hex} \times \sqrt{3}a_{hex}$ type. However as long as the translational symmetry remains indifferent, larger superstructure whose lattice parameters are integral of $\sqrt{3}a_{hex}$ may give the same type of super reflections. Flower ordering is $2\sqrt{3}a_{hex} \times 2\sqrt{3}a_{hex}$ type ordering, as shown in Figure 8-13a). Lithium sits in the vertices of small honeycombs formed by six Mn^{4+} and large honeycombs formed by twelve Ni^{2+}.

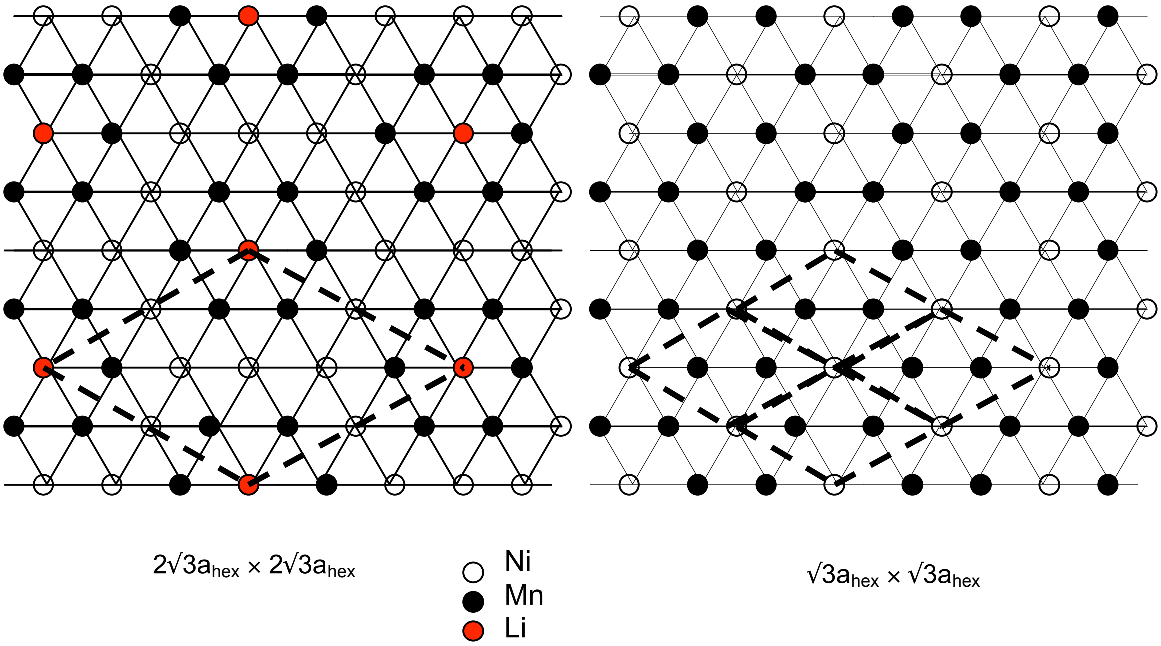

Figure 8-13 a) Flower ordering $2\sqrt{3}a_{hex} \times 2\sqrt{3}a_{hex}$ superstructure, notice that the composition in flower ordering is $Li_{1/9}Ni_{1/3}Mn_{5/9}$. b) Typical $\sqrt{3}a_{hex} \times \sqrt{3}a_{hex}$ superstructure

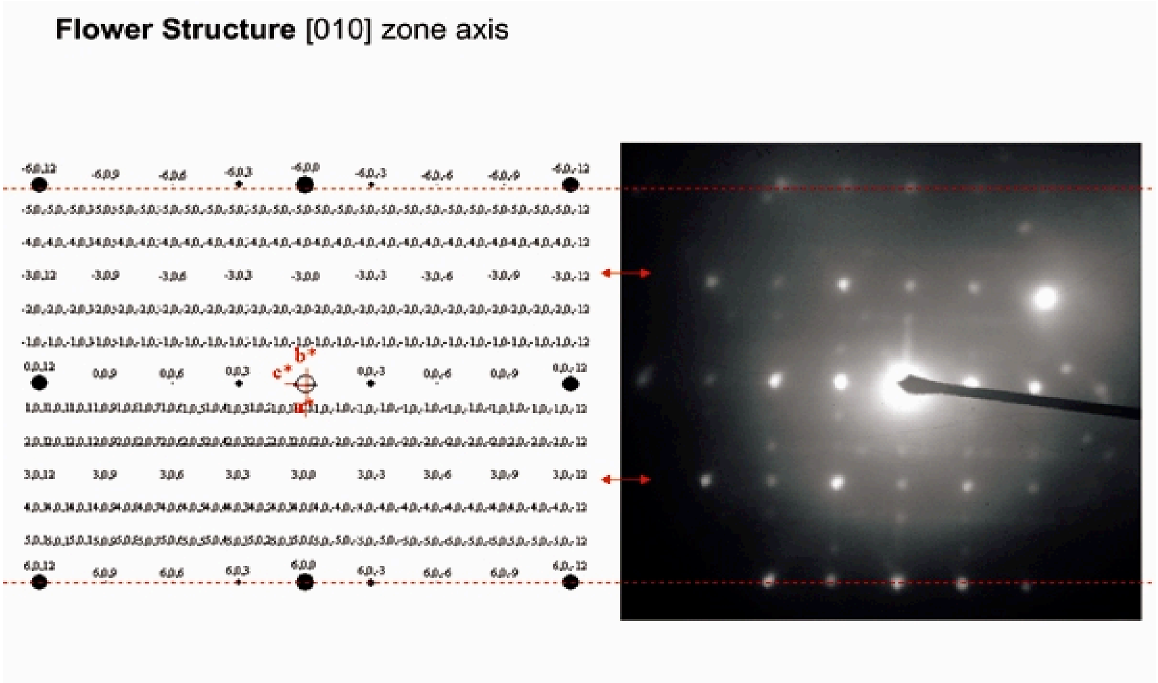

Figure 8-14 Simulated electron diffraction pattern with the flower-type ordering is compared with the $[1\text{-}10]_{hex.}$ electron diffraction pattern of $LiNi_{1/2}Mn_{1/2}O_2$

Electron diffraction experiment reveals the possibility for such complicated superstructure. Notice that the (11***l***) type of reflections in Figure 8-14 are not tripled, but six-fold. This implies that a larger supercell than $\surd 3a_{hex} \times \surd 3a_{hex}$ may exist in the a-b plane. These additional spots can be successfully matched with a simulated ED pattern obtained from flower type of ordering with $2\surd 3a_{hex} \times 2\surd 3a_{hex}$ unit cell [13, 19], as demonstrated in Figure 8-13a).

8.3.2 Stacking Disorder of the Ordered Planes

So far, we have shown that the same type of in-plane ordering is observed in the $LiNi_xLi_{1/3-2x/3}Mn_{2/3-x/3}O_2$ ($0 \le x \le 1/2$) compounds, that is $\surd 3a_{hex} \times \surd 3a_{hex}$ shown in Figure 8-5. However, in principle there may exist an infinite number of possible ways how the ordered planes can be stacked along the $c_{hex.}$ axis.

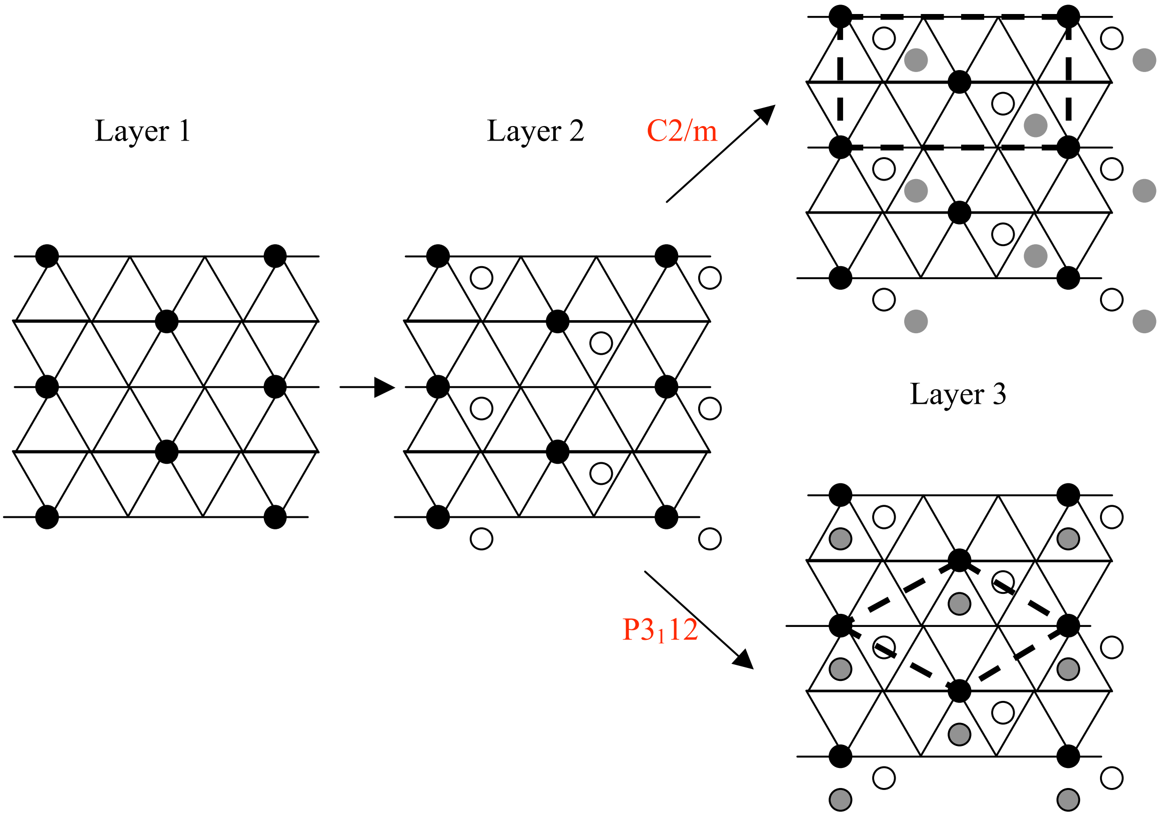

Figure 8-15 Two possible ways of stacking of $\surd 3a_{hex} \times \surd 3a_{hex}$ ordered planes, notice that only α sites are shown, and the superstructures are outlined by dashed lines

The two structures with different space groups $P3_112$ and C2/m are closely related to each other since they have the same in-plane ordering but differ only in the direction along which the ordered planes are stacked. The difference in the two structures is demonstrated by stacking three successive transition metal layers along the $c_{hex.}$ direction. It is important to realize that the same in-plane ordering but different stacking of these ordered planes will lead to different space group and crystal symmetry in the compounds. Consequently, these structures will show different superstructure reflections in the diffraction study. In Figure 8-15, three successive layers of transition metal layers are projected along $(001)_{hex.}$ to demonstrate the distinction between two structures $P3_112$ and C2/m.

Although electron diffraction data of the $Li[Ni_xLi_{1/3-2x/3}Mn_{2/3-x/3}]O_2$ (x = 1/2, 1/3 and 0) crystals could be indexed to the $\sqrt{3}\boldsymbol{a}_{hex.} \times \sqrt{3}\boldsymbol{a}_{hex.} \times \boldsymbol{c}_{hex.}$ superstructure with space group $P3_112$, it is important to point out that electron diffraction results cannot preclude the presence of some transition metal layers with the *C2/m* stacking sequence in the individual crystals analyzed. Therefore, it is believed that the transition metal layers in the layered $Li[Ni_xLi_{1/3-2x/3}Mn_{2/3-x/3}]O_2$ compounds can be arranged in the following ways: 1) mostly in the $P3_112$ stacking with some *C2/m* stacking abnormally and 2) in two or three different *C2/m* stacking sequence variants (*abab…*, *caca…* and *cbcb…*) along the $\boldsymbol{c}_{hex.}$ axis. The presence of nickel in the lithium layer between two adjacent transition metal layers could play an important role in how the transition metal layers of '$Li[Ni_{1/2}Mn_{1/2}]O_2$' and '$Li[Ni_{1/3}Li_{1/9}Mn_{5/9}]O_2$' crystals are stacked along the $\boldsymbol{c}_{hex.}$ axis. The details of such stacking order/disorder will be discussed in the next Chapter.

8.4 Conclusions

A combination of experimental techniques that probe different relevant length scales is necessary to truly understand the structure of complex solids. In $LiNi_xLi_{1/3-2x/3}Mn_{2/3-x/3}O_2$ ($0 \leq x \leq 1/2$) electron diffraction reveals the presence of long-range ordering, previously undetected with X-ray diffraction and neutron diffraction. A superstructure with $\sqrt{3}a_{hex} \times \sqrt{3}a_{hex}$ in-plane ordering and *a1b2c1* stacking order is proposed, though electron diffraction study reveals possibly more complicated superstructure such as flower ordering with $2\sqrt{3}a_{hex} \times 2\sqrt{3}a_{hex}$ plane ordering in the composition $LiNi_{1/2}Mn_{1/2}O_2$. In plane disorder and stacking disorder are also observed experimentally, certain degree of disorder is expected since the material is synthesized at elevated temperature and quench to room temperature upon cooling. The exact long range order parameters depend on synthesis conditions, cooling rates and stoichiometry control.

References:

1. Z.H. Lu and J.R. Dahn, *Understanding the anomalous capacity of* $Li/LiNi_xLi_{(1/3-2x/3)}Mn_{(2/3-x/3)}O_2$ *cells using in situ X-ray diffraction and electrochemical studies*. Journal of the Electrochemical Society, 2002. **149**(7): p. A815-A822.
2. P. Strobel and B. Lambertandron, *Crystallographic and Magnetic-Structure of* Li_2MnO_3. Journal of Solid State Chemistry, 1988. **75**(1): p. 90-98.
3. C.P. Grey, *Personal Communication*. 2004.
4. B. Ammundsen, et al., *Local structure and first cycle redox mechanism of layered* $Li_{1.2}Cr_{0.4}Mn_{0.4}O_2$ *cathode material.* Journal of the Electrochemical Society, 2002. **149**(4): p. A431-A436.
5. W.S. Yoon, et al., *Investigation of the local structure of the* $LiNi_{0.5}Mn_{0.5}O_2$ *cathode material during electrochemical cycling by X-ray absorption and NMR spectroscopy.* Electrochemical and Solid State Letters, 2002. **5**(11): p. A263-A266.
6. S.S. Shin, Y.K. Sun, and K. Amine, *Synthesis and electrochemical properties of* $LiLi_{(1-2x)/3}Ni_xMn_{(2-x)/3}O_2$ *as cathode materials for lithium secondary batteries.* Journal of Power Sources, 2002. **112**(2): p. 634-638.
7. Z.H. Lu, Z.H. Chen, and J.R. Dahn, *Lack of cation clustering in* $LiNi_xLi_{1/3-2x/3}Mn_{2/3-x/3}O_2$ $(0 < x <= 1/2)$ *and* $LiCr_xLi_{(1-x)/3}Mn_{(2-2x)/3}O_2$ $(0 < x < 1)$. Chemistry of Materials, 2003. **15**(16): p. 3214-3220.
8. Y. Makimura and T. Ohzuku, *Lithium insertion material of* $LiNi_{1/2}Mn_{1/2}O_2$ *for advanced lithium-ion batteries.* Journal of Power Sources, 2003. **119**: p. 156-160.
9. Y. Shao-Horn, et al., *Probing lithium and vacancy ordering in O3 layered* Li_xCoO_2 *(x approximate to 0.5) - An electron diffraction study.* Journal of the Electrochemical Society, 2003. **150**(3): p. A366-A373.
10. A. Van der Ven, M.K. Aydinol, and G. Ceder, *First-principles evidence for stage ordering in* Li_xCoO_2. J. Electrochem. Soc., 1998. **145**(6): p. 2149-2155.
11. M. de Dompablo, A. Van der Ven, and G. Ceder, *First-principles calculations of lithium ordering and phase stability on* Li_xNiO_2. Physical Review B, 2002. **66**(6).
12. Cowley, J.M., *Diffraction Physics*. 1981, New York: North-Holland.
13. W.S. Yoon, et al., *Local structure and cation ordering in O3 lithium nickel manganese oxides with stoichiometry* $LiNi_xMn_{(2-x)/3}Li_{(1-2x)/3}O_2$ *- NMR studies and first principles calculations.* Electrochemical and Solid State Letters, 2004. **7**(7): p. A167-A171.
14. http://www.ncnr.nist.gov/resources/n-lengths/.
15. V. Massarotti, et al., *Ab initio structure determination of* Li_2MnO_3 *from X-ray powder diffraction data.* Journal of Applied Crystallography, 1997. **30**: p. 123-127.
16. B. Fultz and J.M. Howe, *Transmission Electron Microscopy and Diffractometry of Materials*. 2nd ed. 2002, New York: Springer.
17. Z.H. Lu, et al., *Synthesis, structure, and electrochemical behavior of* $Li\ Ni_xLi_{1/3-2x/3}Mn_{2/3-x/3}O_2$. Journal of the Electrochemical Society, 2002. **149**(6): p. A778-A791.
18. J.M. Cowley, *Diffraction Physics*. 1995, Amsterdam; New York: Elsevier Science B.V.

19. A. Van der Ven and G. Ceder, *Ordering in* $Li_x(Ni_{0.5}Mn_{0.5})O_2$ *and its relation to charge capacity and electrochemical behavior in rechargeable lithium batteries.* Electrochemistry Communications, 2004. **6**: p. 1045-1050.

CHAPTER 9

STACKING DISORDER AND POLYTYPISM IN $LiNi_xLi_{1/3-2x/3}Mn_{2/3-x/3}O_2$ ($0 \leq x \leq 1/2$)

Stacking faults do not always occur randomly. When the faults are regularly spaced, such periodic faulting in the crystal leads to polytypism. Polytypism is used to denote a special type of polymorphism in which the different structures assumed by a compound differ only in the order in which a two-dimensional layer is stacked. With a brief review on structure of Li_2MO_3 system and more experimental evidence on stacking disorder in $LiNi_xLi_{1/3-2x/3}Mn_{2/3-x/3}O_2$ ($0 \leq x \leq 1/2$), we discuss possible polytypes in this chapter.

9.1 Review on Li_2MO_3 System

Lang G. discussed the possible stacking sequences in Li_2SnO_3 [1]. The oxygen atoms form a distorted cubic close-packed network, and the cations occupy, in an ordered fashion, all octahedral sites present in the network. Pure Li layer alternates with layers of composition $Li_{1/3}Sn_{2/3}$ in which the cations are ordered in such a way that they form hexagonal close-packed planes in which the tin atoms occupy the vertices of the hexagons and the lithium atoms the centers, known as the $\sqrt{3}a_{hex} \times\sqrt{3}a_{hex}$ superlattice. There are at least three ways of stacking these ordered $Li_{1/3}Sn_{2/3}$ planes. In _-form Li_2SnO_3 (high-temperature form), a given layer repeats every six levels, namely, after a double cubic close-pack sequence *a1b2c1a2b1c2*, as demonstrated in Figure 9-1. In _-form the low temperature form of Li_2SnO_3, two polytypic structures are present. If the stacking sequence of the $Li_{1/3}Sn_{2/3}$ layers is *a1b2c1*, the symmetry of the structure is $P3_112$; if the stacking sequence of the $Li_{1/3}Sn_{2/3}$ is *a1c1*, the symmetry of the structure is C2/m, as shown in Figure 9-2.

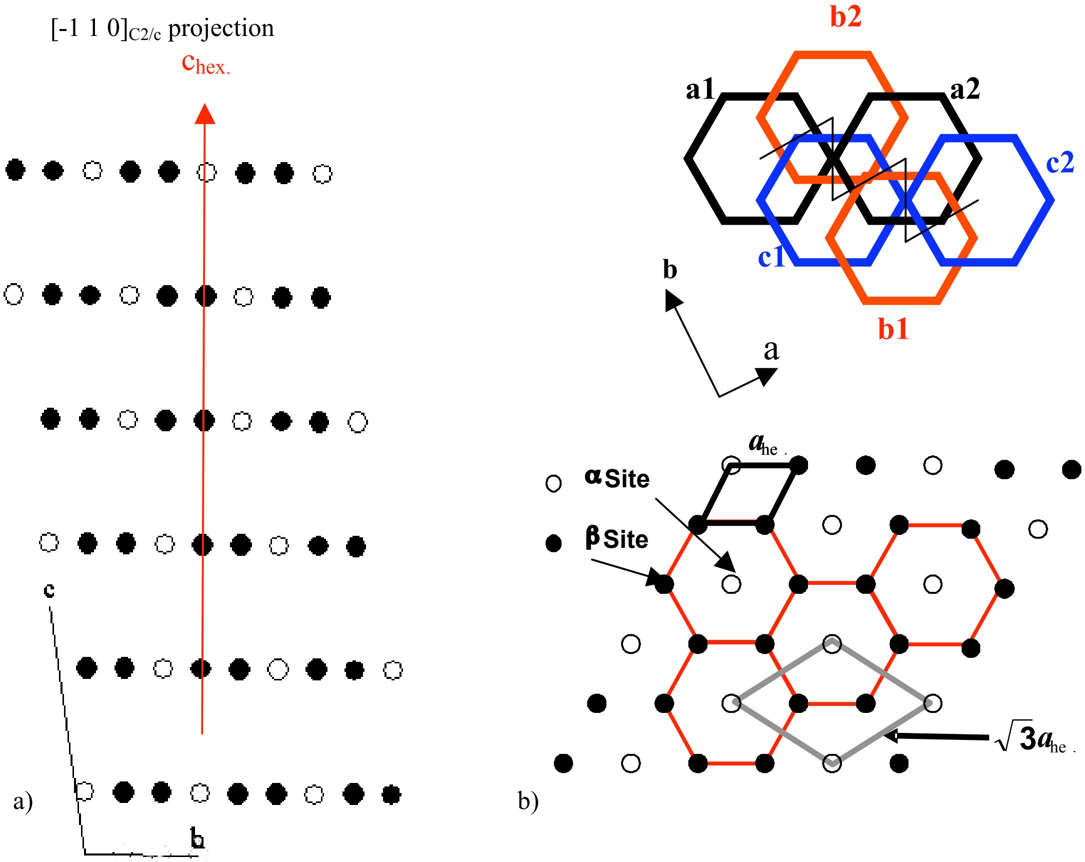

Figure 9-1 Stacking sequence of C2/c structure: a) [-110] projection b)[001] projection of the $Li_{1/3}M_{2/3}$ planes for Li_2MO_3

Structures of other Li_2MO_3 (M = Mn, Ti, Ru, Pt. etc.) [2-13] were studied by various groups and summarized by Kanno et. al, as shown in Figure 9-3 [11]. They tried to correlate the types of structures with the ionic radii of M^{4+}. It should be stressed that the Li_2ZrO_3 belongs to a completely different type of structure, in which there is no separation of pure Li layer and $Li_{1/3}Zr_{2/3}$ layer; instead, layers of $Li_{2/3}Zr_{1/3}$ alternate with oxygen layers [8]. In general, it is true that when the size of M^{4+} is smaller than

Li+ (0.70Å), there will be separation of Li layers of $Li_{1/3}M_{2/3}$ layers, though the exact polytypes (stacking sequences) of these ordered layers is found not directly related to the ionic size. The summary of previous experimental data is summarized in Appendix A.

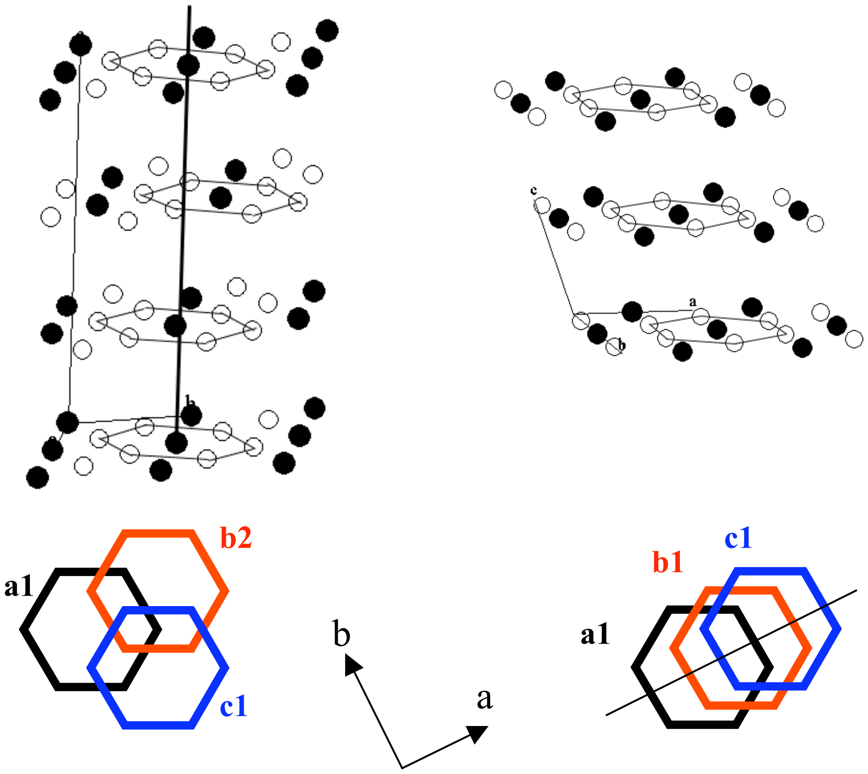

(a) (b)

Figure 9-2 Stacking sequences of a) $P3_112$ structure; b) C2/m structure for Li_2MO_3

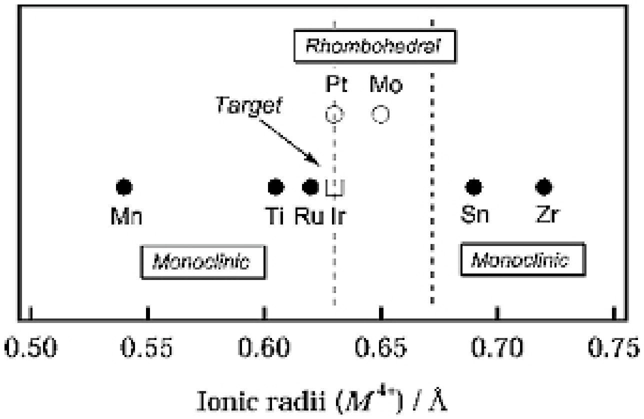

Figure 9-3 Relationship between the ionic radii of transition metals (M^{4+}) and lattice symmetry of Li_2MnO_3. Rhombohedral and monoclinic lattice symmetries are represented by circle and solid ball, respectively.

9.2 First Principles Investigation

To better understand different polytypes, we calculate the total energies of the three different polytypes C2/c, $P3_112$ and C2/m of Li_2MnO_3, Li_2TiO_3 and Li_2SnO_3 using first principles methods [14, 15].

Table 9-I VASP Calculated (GGA) Total Energies of Different Polytypes in Li_2MO_3 (M = Mn, Sn & Ti)

eV/Formula	Li_2MnO_3*	Li_2SnO_3	Li_2TiO_3
C2/m	-40.0218	-34.0410	-42.8055
C2/c	-40.0199	-34.0435	-42.8061
$P3_112$	-40.0206	-34.0421	-42.8052

* antiferromagnetic configuration also considered, no qualitative difference is found.

It was found that regardless of M^{4+} ion size, the energies (eV/formula unit) for three different polytypes are extremely similar, within 1meV difference.

For Li_2MnO_3, though C2/m consistently has the lowest energy for calculations with high k-point density. The C2/c structure is about 2 meV per formula unit higher in energy than the C2/m structure, while $P3_112$ is approximately 1meV higher in energy than C2/m. While these numbers are small we believe they are numerically significant. These small energy differences indicate a small energy penalty associated with a shifting of the transition-metal stacking. Whether such small energy differences will lead to thermal stacking faults depends on the coherence length of the Li-Mn ordering within the transition metal layer, as this determines the size of the domain over which the fault extends, and hence its total energy. Only if this *total* energy of the fault is of the order of the thermal energy, can faults be stabilized by entropic effects.

Polytypism differs from ordinary polymorphism in several respects. The different polymorphs of a compound represent definite thermodynamic states, each characterized by a range of T and P within which it has the minimum free energy G. Polymorphs are related to each other by first-order phase transformations and usually have widely different crystal structures and physical properties. The free energy G differences of different polytypes are vanishingly small as well. If a perfect crystal is considered for Li_2MO_3, that is the ordered $Li_{1/3}M_{2/3}$ layer is infinitely large, the energy E difference of different polytypes is infinitely large. In addition, even the most random stacking will affect the total entropy S insignificantly, since the entropy increase due to stacking disorder is negligible compared with the entropy due to point disorder. However, in practice it is important to realize that the ordered plane may not be perfect due to thermal disorder. For instance, we have shown that certain in-plane disorder is present in $LiNi_{1/2}Mn_{1/2}O_2$ powder samples. If the ordered domain has a finite size, then the energy penalty for an abnormally stacking sequence is small.

9.3 Polytypism and Stacking Faults in $LiNi_xLi_{1/3-2x/3}Mn_{2/3-x/3}O_2$ (0 $\leq x \leq$ 1/2)

9.3.1 Stacking Disorder and Diffax XRD Simulation

Stacking disorder in Li_2MnO_3 has been experimentally observed. As shown in Figure 8-3 in the previous chapter, in the experimentally obtained XRD spectrum the superstructure peaks shapes and intensities differ significantly from the simulated XRD spectrum of Li_2MnO_3 with space group C2/m. NMR study by C.P. Grey [17] has shown that there is little in-plane disorder, i.e. site mixing in $Li_{1/3}Mn_{2/3}$ layer.

Preliminary powder XRD simulation with DIFFAX [16] reveals that such discrepancy is mainly due to the stacking disorder along c_{hex}. axis.

The family of structures, C2/c, $P3_112$ and C2/m, can be considered as a result of a difference in the separation of stacking faults, where one plane of atoms slipping relative to another. When there is completely randomly stacking, R-3m structure is recovered with infinitely long periodicity along $c_{hex.}$ Diffax* is a program that calculates the powder diffraction spectrum of a crystal formed from layers which stack coherently, but not deterministically. Stacking probabilities for different layers are introduced to simulate disorder. Figure 9-4 shows the XRD DIFFAX simulation of C2/m Li_2MnO_3 with stacking faults. The spectrum from a structure in which 3.3% defect is introduced matches well with the experimental XRD spectrum. That implies there is possibly one stacking faults every 30 layers in the powder Li_2MnO_3 we synthesized.

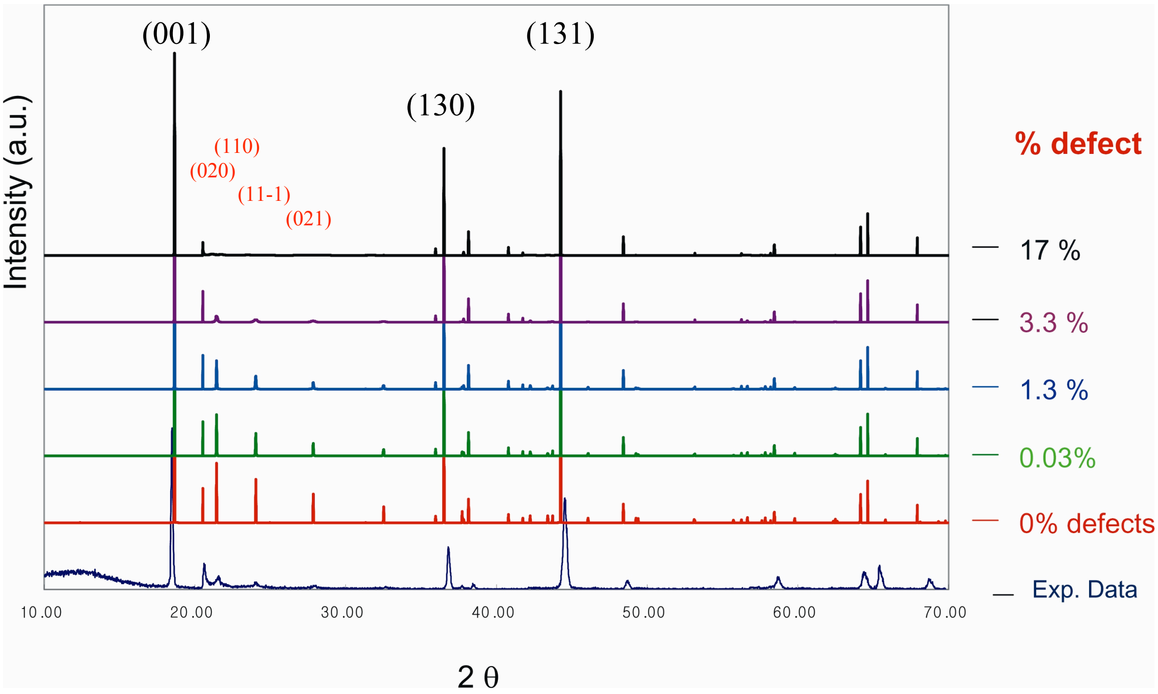

Figure 9-4 Comparison of experimental and Diffrax simulated powder XRD spectra [17] *[16] The algorithm used is described in detail in "A General Recursion Method for Calculating Diffracted

Intensities From Crystals Containing Planar Faults", by M.M.J. Treacy, M.W. Deem and J.M. Newsam, Proceedings of the Royal Society, London, A (1991) 433, pp 499 - 520.

Notice that in the more extreme case (very high percentage of stacking faults), some superstructure peaks might be so low that they are not detectable by conventional powder XRD experiment. Therefore, it is important to realize that the absence of superstructure peaks in the XRD spectrum does not rule out the possibility of long range in-plane ordering in the compound.

9.3.2 Polytypes and Electron Diffraction

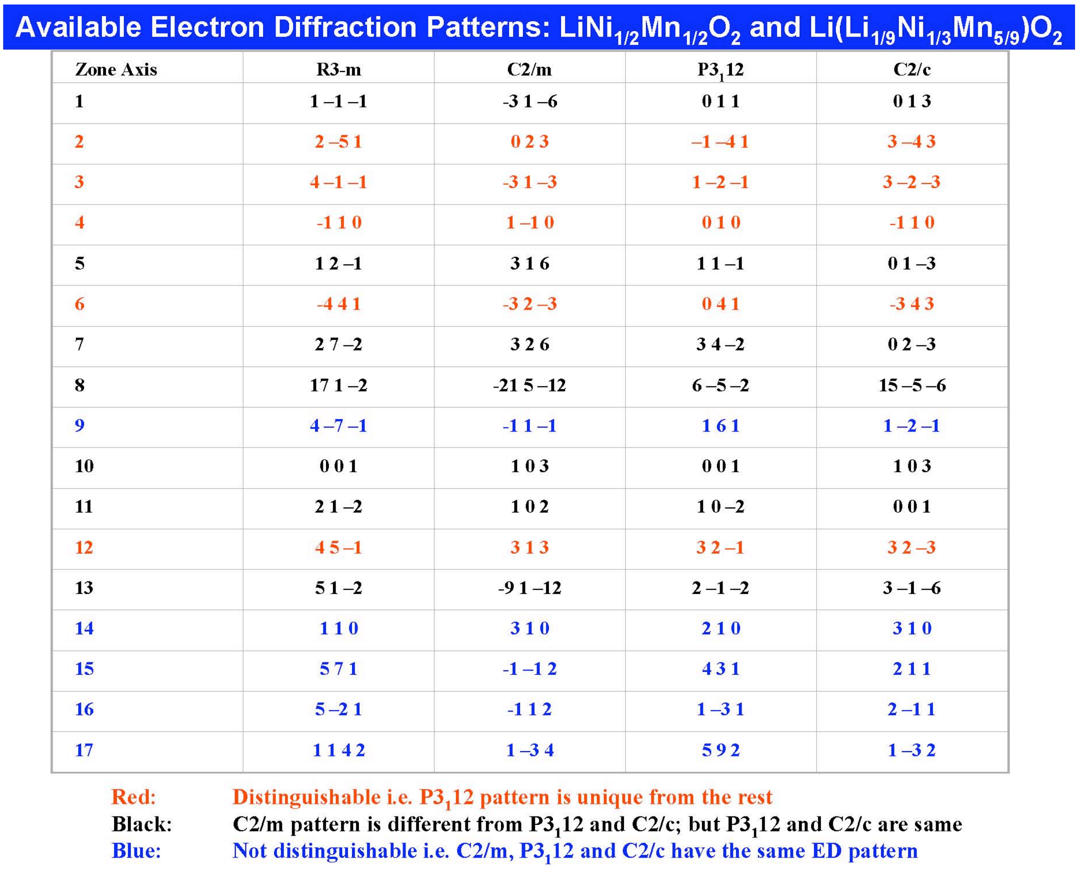

Available Electron Diffraction Patterns: $LiNi_{1/2}Mn_{1/2}O_2$ and $Li(Li_{1/9}Ni_{1/3}Mn_{5/9})O_2$

Zone Axis	R3-m	C2/m	$P3_112$	C2/c
1	1 –1 –1	-3 1 –6	0 1 1	0 1 3
2	2 –5 1	0 2 3	–1 –4 1	3 –4 3
3	4 –1 –1	-3 1 –3	1 –2 –1	3 –2 –3
4	-1 1 0	1 –1 0	0 1 0	-1 1 0
5	1 2 –1	3 1 6	1 1 –1	0 1 –3
6	-4 4 1	-3 2 –3	0 4 1	-3 4 3
7	2 7 –2	3 2 6	3 4 –2	0 2 –3
8	17 1 –2	-21 5 –12	6 –5 –2	15 –5 –6
9	4 –7 –1	-1 1 –1	1 6 1	1 –2 –1
10	0 0 1	1 0 3	0 0 1	1 0 3
11	2 1 –2	1 0 2	1 0 –2	0 0 1
12	4 5 –1	3 1 3	3 2 –1	3 2 –3
13	5 1 –2	-9 1 –12	2 –1 –2	3 –1 –6
14	1 1 0	3 1 0	2 1 0	3 1 0
15	5 7 1	-1 –1 2	4 3 1	2 1 1
16	5 –2 1	-1 1 2	1 –3 1	2 –1 1
17	1 1 4 2	1 –3 4	5 9 2	1 –3 2

Red:	**Distinguishable i.e. $P3_112$ pattern is unique from the rest**
Black:	**C2/m pattern is different from $P3_112$ and C2/c; but $P3_112$ and C2/c are same**
Blue:	**Not distinguishable i.e. C2/m, $P3_112$ and C2/c have the same ED pattern**

Figure 9-5 Summary of experimentally observed electron diffraction zone axes for $LiNi_{1/2}Mn_{1/2}O_2$ and $LiNi_{1/3}Li_{1/9}Mn_{5/9}O_2$.

Due to the same type of in-plane ordering, electron diffraction patterns from the three polytypes might be same. In fact, as summarized in Figure 9-5, for

$LiNi_{1/2}Mn_{1/2}O_2$ and $LiNi_{1/3}Li_{1/9}Mn_{5/9}O_2$ samples only 5 out of the 17 zone axes patterns we obtained are unique for the $P3_112$ structure. The others are the same in the two other polytypes. The equivalent zone axes are calculated according to the conversion matrices presented in Figure 8-5 in the previous chapter. Therefore, it is from these five unique patterns that we conclude *a1b2c1* is the most probable way of stacking in $LiNi_{1/2}Mn_{1/2}O_2$ and $LiNi_{1/3}Li_{1/9}Mn_{5/9}O_2$.

Furthermore, in the experimental electron diffraction pattern obtained from $LiNi_{1/2}Mn_{1/2}O_2$ sample, as shown in Figure 9-6, we observed the diffuse streak which indicates one dimensional disorder in the diffraction pattern obtained from $[1\text{-}10]_{hex.}$ zone axis. The streakings occur parallel to $c^*_{hex.}$. (notice c* is perpendicular to ab plane, same as $c_{hex.}$ axis in real space)

With a rhombohedral lattice (hexagonal axes), the indices of reciprocal lattice point are limited by selection rule $-h+k+l=3n$, as the fundamental reflections are indexed. In the primitive cells of different proposed structure models - C2/m, C2/c and $P3_112$, the larger the spacing d_{001}, the smaller the value of c* and more crowded the reciprocal lattice rows parallel to c. For a structure with a completely disordered arrangement of layers $d_{001} = \infty$ and $c^* = 0$. The reciprocal lattice rows parallel to c* become continuous lines. Notice that the diffuseness of spots in reciprocal space occurs only for rows with $-h+k \neq 3n$, since the fundamental reflections (where $-h+k = 3n$) are unaffected by the different polytypes.

For different proposed structure models (polytypes), the periodicity along the c axis in the ***primitive*** cells increases in the order of C2/m < C2/c < $P3_112$. The simulated diffraction patterns of these three structures are shown in Figure 9-6 (a) (b) and (c) respectively.

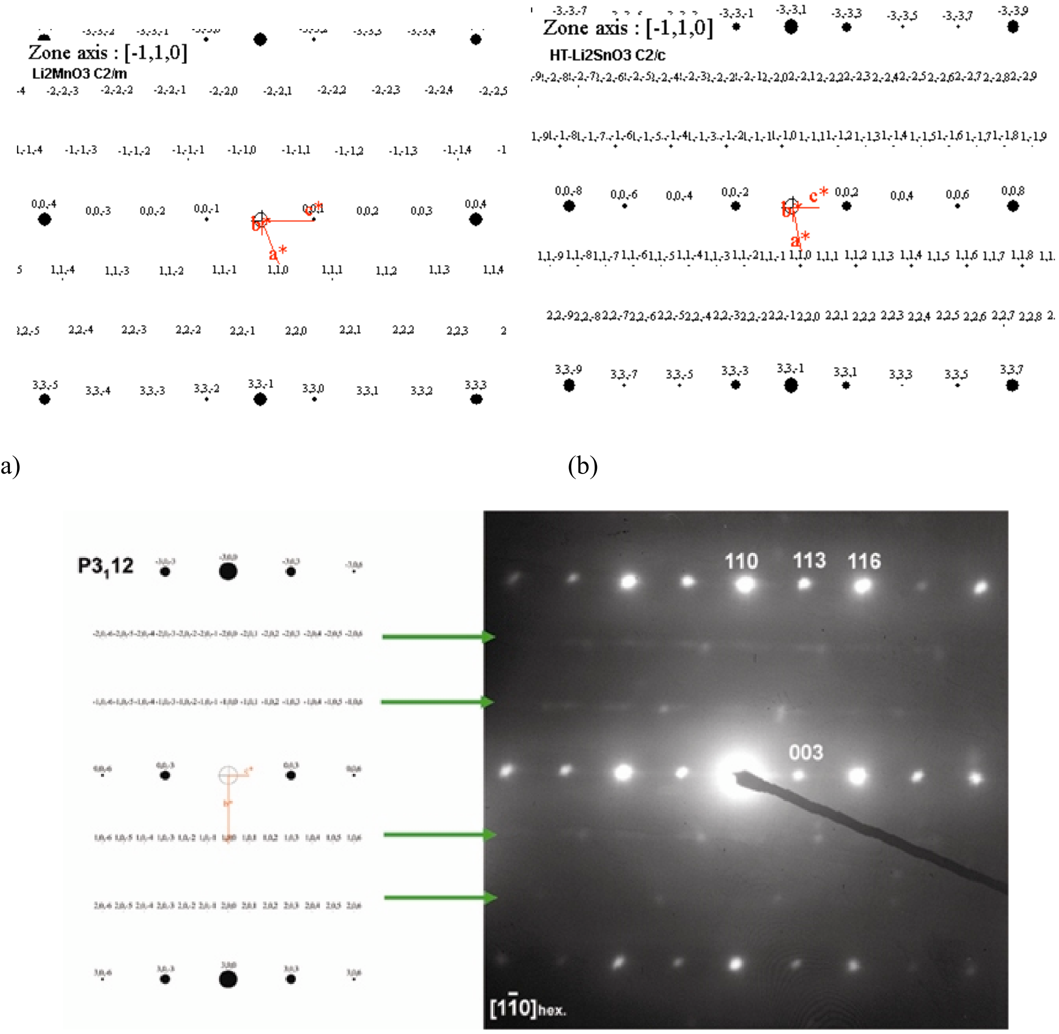

(a) (b)

(c) (d)

Figure 9-6 Simulated electron diffraction pattern from equivalent zone axis of a) C2/m b) C2/c and c) $P3_112$, which well fit the experimentally obtained $[1\text{-}10]_{hex.}$ zone axis electron diffraction pattern of $LiNi_{1/2}Mn_{1/2}O_2$.

Similar type of streaking was also observed by Ohzuku et al. [18] as shown by an electron diffraction pattern from the same zone axis in Figure 9-7.

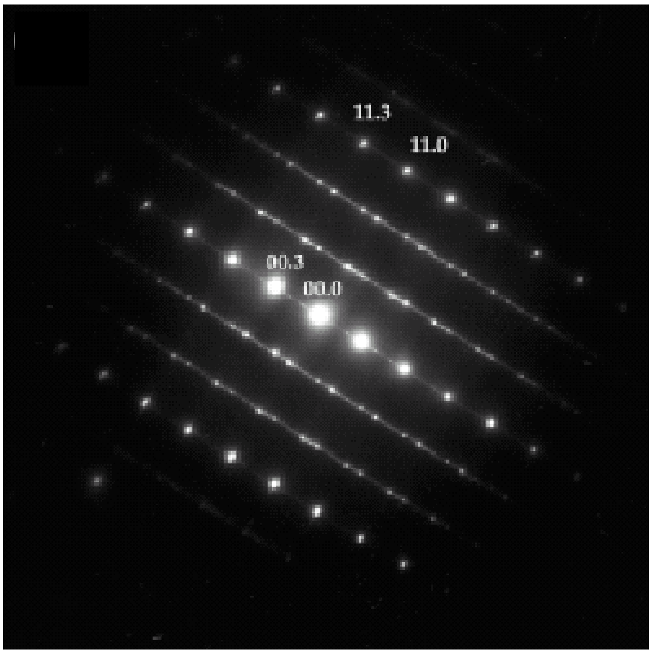

Figure 9-7 $[1\text{-}10]_{hex.}$ zone axis electron diffraction pattern of $LiNi_{1/2}Mn_{1/2}O_2$ [18]

9.4 Significance of Polytypism in Intercalation Compounds

Polytypism has been found in many close-packed systems. Substantial works have been carried out to identify the causes and significance of polytypism in materials. In the metallic system, it is believed that the superlattice period alters the Brillouin zone structure of the metal in such a may as to lower the total energy of the free electrons [19]. It is this lowering of energy that stabilizes the superlattice structure. However, in non-metallic system, these arguments do not apply, the differences in the first-order terms for the energy of polytypic structures are negligible, second-order effects play an important role in determining the structure. *Polytypism does have an impact on the physical properties, for example it is found that longer periodicity leads to a narrower band-gap in SnS_2.[20]* In $LiNi_xLi_{1/3-2x/3}Mn_{2/3-x/3}O_2$ system, the significance of stacking disorder/order on the electrochemical properties have *not* been fully characterized, though the materials synthesized at different conditions (temperature and cooling rate) display different reversible capacities in a recent study by Shao-Horn et al. [21].

9.5 Conclusions

XRD powder diffraction and electron diffraction evidence of stacking disorder in $LiNi_xLi_{1/3-2x/3}Mn_{2/3-x/3}O_2$ system are discussed. The possible ways of stacking ordered planes in the O3 layered structure are demonstrated. Although the significance of stacking order/disorder on the electrochemical properties has not been systematically explored, we believe that the types of order/disorder structures present in the system have a significant impact on the electrochemical properties.

References:

1. G. Lang, *Structure of Ternary Oxides.* Z. anorg. allg. Chem, 1966. **348**: p. 246.
2. H. Kobayashi, et al., *Synthesis and electrochemical properties of lithium molybdenum oxides.* Journal of Power Sources, 1999. **82**: p. 524-529.
3. A. James and J.B. Goodenough, *Structure and Bonding in* Li_2MoO_3 *and* $Li_{2-x}MoO_3$ $(0 \leq X \leq 1.7)$. Journal of Solid State Chemistry, 1988. **76**(1): p. 87-96.
4. A. James and J.B. Goodenough, *Structure and Bonding in Lithium Ruthenate,* Li_2RuO_3. Journal of Solid State Chemistry, 1988. **74**(2): p. 287-294.
5. P. Strobel and B. Lambertandron, *Crystallographic and Magnetic-Structure of* Li_2MnO_3. Journal of Solid State Chemistry, 1988. **75**(1): p. 90-98.
6. V. Massarotti, et al., *Ab initio structure determination of* Li_2MnO_3 *from X-ray powder diffraction data.* Journal of Applied Crystallography, 1997. **30**: p. 123-127.
7. J.F. Dorrian and R.E. Newnham, *Refinement of the Structure of* Li_2TiO_3. Mat. Res. Bull, 1969. **4**: p. 179-184.
8. J.L. Hodeau and M. Marezio, *Neutron Profile Refinement of the Structures of* Li_2SnO_3 *and* Li_2ZrO_3. Journal of Solid State Chemistry, 1982. **45**: p. 170-179.
9. H. Kobayashi, et al., *Structure and charge/discharge characteristics of new-layered oxides:* $Li_{1.8}Ru_{0.6}Fe_{0.6}O_3$ *and* Li_2IrO_3. Journal of Power Sources, 1997. **68**(2): p. 686-691.
10. H. Kobayashi, et al., *Structure and lithium deintercalation of* $Li_{2-x}RuO_3$. Solid State Ionics, 1995. **82**: p. 25-31.
11. H. Kobayashi, et al., *Structure, and magnetic and electrochemical properties of layered oxides,* Li_2IrO_3. Journal of Materials Chemistry, 2003. **13**(4): p. 957-962.
12. K. Asakura, et al., *Cathode properties of layered structure* Li_2PtO_3. Journal of Power Sources, 1999. **82**: p. 388-392.
13. Y. Laligant, P. Lacorre, and J. Rodriquez-Carvajal, *Powder structure determination of* Li_2PdO_3*: a NaCl structure type with turbostratic effect*, in *Epdic 7: European Powder Diffraction, Pts 1 and 2*. 2001. p. 632-637.
14. J., Reed G. Ceder, and A. Van Der Ven, *Layered-to-spinel phase transition in* Li_xMnO_2. Electrochemical and Solid-State Letters, 2001. **4**(6): p. A78.
15. Reed, J., *Ab Initio Study of Cathode Materials for Lithium Batteries*, in *Department of Materials Science and Engineering*. 2003, Massachusetts Institute of Technology: Cambridge, MA. p. 311.
16. M.M.J. Treacy, J.M. Newsam, and M.W. Deem, *A general recursion method for calculating diffracted intensities from crystals containing planar faults.* Proc. R. Soc. London Ser. A, 1991. **43**: p. 499-520.
17. B. Julien and C.P. Grey, *Personal communication: unpublished data*. 2004.
18. Y. Makimura, N. Nakayama, and T. Ohzuku. *Structural Chemistry and Electrochemistry of* $LiNi_{1/2}Mn_{1/2}O_2$ *for Advanced Lithium Batteries*. in *The Electrochemical Society Meeting*. 2003. Paris France.
19. M.T. Sebastian and P. Krishna, in *Random, Non-Random and Periodic Faulting in Crystals*. 1994, Gordon and Breach Science Publishers.

20. A.M.F. Samuel and O.N. Srivastava, in *Crystal Growth and Characterisation of Polytype Structures*, P. Krishna, Editor. 1983, Pergomon: London.
21. Y. Shao-Horn, *Personal Communication*. 2004.

Chapter 10

CONCLUSIONS

In this research, first principles computation and various experiments were used as tools in designing and understanding lithium nickel manganese oxides and their derivatives. In an initial search on $LiNi_{1/3}TM1_{1/3}TM2_{1/3}O_2$ (TM1 = Co^{3+}, Al^{3+}, Fe^{3+} etc. and TM2 = Ti^{4+}, Zr^{4+}, Mn^{4+} etc.) with first principles computation Fe substitution is found to be advantageous as it lowers the lithium intercalation voltage at the end of charge. Among all the compounds investigated $LiNi_{1/3}Fe_{1/3}Mn_{1/3}O_2$ shows the lowest voltage at the last stage of charge, which leads to the highest achievable capacity in practical voltage window 3.0-4.5V. According to calculations of the enthalpy of mixing, excess Fe doping will result in a non-layered impurity phase, which is consistent with the experimental finding. The structural and electronic changes of $LiNi_{1/3}Fe_{1/6}Co_{1/6}Mn_{1/3}O_2$ with various lithium concentrations were investigated by first principles method. Motivated by the computational results, $LiNi_{1/3}Fe_zCo_{1/3-z}Mn_{1/3}O_2$ ($0 \le z \le 1/3$) cathode materials were synthesized by a sol-gel method. Excessive Fe substitution ($z > 2/9$) leads to the evolution of a non-layered impurity phase, which can be clearly observed by powder XRD and SEM experiments. XPS investigation for $LiNi_{1/3}Fe_zCo_{1/3-z}Mn_{1/3}O_2$ revealed that the oxidation state of Ni, Mn, Fe and Co are 2+, 4+, 3+ and 3+, respectively, which is consistent with the first principles prediction. Electronic structure computations indicated that Ni and Fe are simultaneously oxidized in this material and Co will only be oxidized at the very end of charge which is confirmed both by XPS and in-situ XAS. We therefore demonstrate that an integrated approach of computation and experiment has produced a potential new electrode material $LiNi_{1/3}Fe_{1/6}Co_{1/6}Mn_{1/3}O_2$ with very few iteration steps in the material design cycle.

The inductive effect is found to explain the changes in the Ni^{2+}/Ni^{4+} redox voltage shift in Li(Ni, TM1, TM2)O_2 layered compounds. With the counter cation that competes for the same anion orbital, the amount of orbital mixing of Ni-O bonding can be modulated. It is found that Fe and Co doping induces an increase in the hybridization between the Ni d-levels and the oxygen p-levels, therefore raises the Ni^{2+}/Ni^{4+} redox energy, i.e. lowers the voltage. Ti and Zr doping raises the voltage at which Ni is active in Li(Ni, TM1, TM2)O_2. In the case of $LiNi_{1/2}Mo_{1/2}O_2$, it is predicted with first principles method that the Mo^{4+}/Mo^{6+} redox couple is active at a lower voltage than Ni^{2+}/Ni^{4+} redox couple.

A combination of experimental techniques that probe different relevant length scales is necessary to truly understand the structure of complex solids. In $LiNi_xLi_{1/3-2x/3}Mn_{2/3-x/3}O_2$ ($0 \le x \le 1/2$) electron diffraction study reveals the presence of long-range ordering of Li, Ni and Mn in the transition metal layer, previously undetected with X-ray diffraction and neutron diffraction. A superstructure with $\sqrt{3}a_{hex} \times \sqrt{3}a_{hex}$ in-plane ordering and abc stacking order is proposed, though an electron diffraction study reveals possibly more complicated superstructure such as flower pattern with $2\sqrt{3}a_{hex} \times 2\sqrt{3}a_{hex}$ in-plane ordering in the composition $LiNi_{1/2}Mn_{1/2}O_2$. In plane disorder and stacking disorder are also observed experimentally. A certain degree of disorder is expected since the materials are synthesized at elevated temperature and quench to room temperature upon cooling. With powder X-ray and neutron diffraction simulation, we demonstrated that for $LiNi_{1/2}Mn_{1/2}O_2$ ($x = 1/2$) such ordering would be extremely difficult to detect experimentally, if not impossible by powder diffraction. First principles computation plays an important role in optimizing the structural model and better interpreting the electron diffraction patterns. The total energies of different polytypes of Li_2MO_3 are extremely similar, which explains the reason why stacking disorder is expected in the system. The significance of stacking faults in the electrochemical properties of the series have not been systematically studied, and further work is required.

Our approach of directly integrating computation modeling methods with experimental research can screen a larger number of candidate materials and significantly shorten the development cycle of such new electrode materials in lithium ion batteries. Ab Initio computation is a powerful pre-screening tool to identify the potential candidate electrode materials prior to synthesis of the materials. It is also an excellent explanatory tool to understand the experimental observations. Such a combination of virtual material design and knowledge-based synthesis/modification has a significant impact on changing the traditional trial-end-error experimentation way of materials design in the battery research field.

Appendix A

Summary of Literature Review on Li_2MO_3 System

Experimental Data Summary on Li_2MO_3 System

3d3	4d5	3p6	4d6	4d4	5d5	5d6	4d2	4d10	4p6
Li_2MnO_3	Li_2RhO_3	Li_2TiO_3	Li_2PdO_3	Li_2RuO_3	Li_2IrO_3	*Li_2PtO_3	Li_2MoO_3	Li_2SnO_3	Li_2ZrO_3
Lattice									
a: 4.937		5.041	5.1207	4.923	5.1664	5.17	2.884	5.295	5.4089
b: 8.532		8.806	8.8440	8.7746	8.933	5.17	2.884	9.184	9.0309
c: 5.030		9.727	5.1095	9.8776	9.7804	14.42	14.934	10.032	5.414
α: 90		90	90	90	90	90	90	90	90
β: 109.46		100.008	109.559	100.073	100.017	90	90	100.032	112.5
γ: 90		90	90	90	90	120	120	90	90
Structure									
C2/m		C2/c βSn	C2/m	C2/c&2	C2/c&2	$P3_1$	R-3m	C2/m	C2/c&3
No SD		No SD	SD	No SD	8% SD	??	Mo3O13	C2/c βSn	Li_2Zr
No ILM		No ILM	ILM	No ILM	No ILM			V^{2+} 4%	only
								Sn^{2+}	
Synthesis									
1273K		??	873K	1273K	1273K	1073K	923K	1273K	1273K
50h			70h	24h	48h	24h	/1073K	16h	16h
							48h		

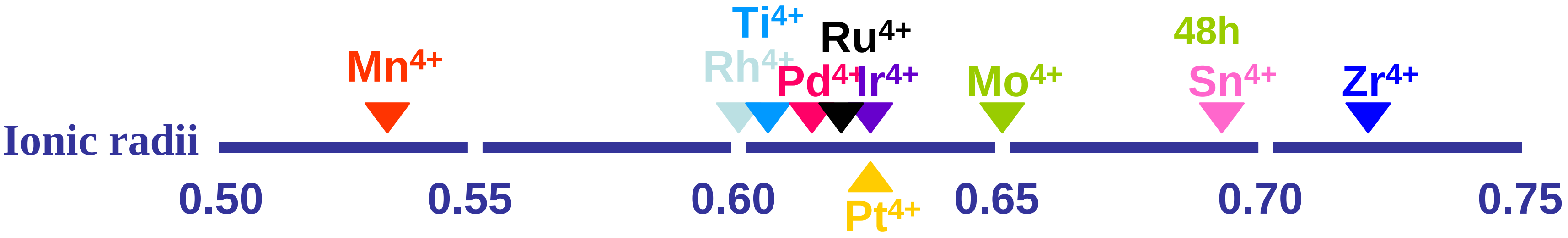

SD: site disorder; ILM: inter-layer mixing

* Refinement not trusted